GRADUATE THESIS APPROVAL FORM AND SIGNATURE PAGE

Instructions: This form must be completed by all doctoral students with a thesis requirement. This form MUST be included as page 1 of your thesis via electronic submission to ProQuest.

Thesis Title: Development and Characterization of 3D Printed Porous Polyetheretherketone for Orthopaedic Applications

Author's Name: Hannah Spece

Submission Date: 09/16/2021

The signatures below certify that this thesis is complete and approved by the Examining Committee.

Role: Member Name: Steven Kurtz
Title: PT Research Prof
Department: School of Biomedical Engineering
Approved: Yes Date: 10/16/2021

Role: Member Name: Sriram Balasubramanian
Title: Associate Professor
Department: School of Biomedical Engineering
Approved: Yes Date: 10/22/2021

Role: Member Name: Michele Marcolongo
Title: Dean of the College of Engineering
Institution: Villanova University
Approved: Yes Date: 10/17/2021

Role: Member Name: Joseph Sarver
Title: Teaching Professor
Department: School of Biomedical Engineering
Approved: Yes Date: 10/18/2021

Role: Chair Name: Kenneth Barbee
Title: Professor
Department: School of Biomedical Engineering
Approved: Yes Date: 10/19/2021

Development and Characterization of 3D Printed Porous Polyetheretherketone for Orthopaedic Applications

A Thesis

Submitted to the Faculty

of

Drexel University

By

Hannah Spece

in partial fulfillment of the

requirements for the degree

of

Doctor of Philosophy

September 2021

Dedication

This dissertation is dedicated to my grandmothers, Sitta and Nan, who always encouraged me to chase my pursuits fearlessly.

Acknowledgements

I would first like to express my immense gratitude to my advisor Dr. Steven Kurtz, for his guidance and encouragement over the years and for making me a better and more confident researcher, writer, and leader. Thank you for introducing me to work that I truly love and for all the amazing opportunities along the way.

Thank you also to my co-advisor Dr. Joseph Sarver, for teaching me how to form and communicate a proper scientific question, a skill that will serve me well for the rest of my career. Your excitement for science is contagious, and our discussions always helped me to realize the worth of my research.

To my committee members, Drs. Michele Marcolongo, Sri Balasubramanian, and Kenneth Barbee, thank you for inspiring me to think about the big picture and for your exceptional feedback and encouragement. You have all helped me to become a better researcher, and I am lucky to have the support of such an impressive group.

I am also grateful to the members of the IRC for providing vital support and making the lab a great place to work. To Genymphas for his advice and for teaching by example how to pursue an enriching grad experience. To Tina and Jackie for our essential research chats and vent sessions, for always offering support, and for being great friends. To Cemile, my grad school sister since Day 1, having you to share all

the new, scary, and exciting experiences along the way was a blessing. To Dan, thanks for sharing your expertise and for all you've taught me.

I would also like to thank the researchers I've worked with and learned from along the way, including Dr. Richard Underwood, Ryan Siskey, and others at Exponent whose experience and knowledge were consistently a great help. I'm grateful also to Dr. Sorin Siegler for his helpful discussions regarding mechanical property analysis. I would also like to thank the Kumovis team, especially Sebastian Pammer and Stefan Leonhardt, for being welcoming and endlessly helpful, and for introducing me to the German way of life. Thank you also to Jonathan Harris at nTopology for his guidance on the homogenization technique, and to Erika Garro for being extraordinarily helpful in the sample testing process.

Lastly, I'd like to express my deep gratitude to my family. To Mom, my first and best teacher, thank you for instilling in me a sense of curiosity and love of learning, and for inspiring me every day. To Dad, thank you for passing on your ingenuity and igniting my interest in building and problem solving. To my siblings, thank you for sharing your excitement for my work (and creative suggestions on what to 3D print next) and for being a constant source of humor and love through grad school. To the Emel family, thank you for your encouragement and for always telling me how proud you are. To Dr. Katie Campbell, one of the greatest researchers I know, thank you for always celebrating my accomplishments and for showing me how a

PhD can be earned with grace and style. Thank you also to the rest of the friends I consider family, for always rooting me on. Finally, to my husband Zach, my gratitude for having you by my side is immeasurable. Thank you for keeping me going with your calming, encouraging, and funny words of wisdom, and for inspiring me with your own amazing work. I'm forever grateful for the support and love you've shared since our days in undergrad.

Table of Contents

List of Tables

List of Figures

Abstract

DEVELOPMENT AND CHARACTERIZATION OF 3D PRINTED POROUS POLYETHERETHERKETONE FOR ORTHOPAEDIC APPLICATIONS

Hannah Spece

Additive manufacturing (AM, 3D printing) is rapidly being adopted by clinicians and researchers aiming to create affordable patient-specific medical devices and other complex structures. In orthopaedics, AM technologies have been especially beneficial for the creation of metallic porous biomaterials, which can help establish bone-implant fixation without the use of bone cement. Metal AM, however, presents considerable challenges for use in a clinical setting, and the potential disadvantages of metal *in vivo* have led to increased interest in nonmetallic implants. Recent advancements in AM have allowed for the printing of high temperature polymers like polyetheretherketone (PEEK) using the fused filament fabrication (FFF) process already adopted by many hospitals. While the bioinert nature of PEEK is often cited as a barrier to its use in osseointegration, the inclusion of porosity by surface modification has shown promising results for bone ingrowth, though often at the expense of mechanical properties. Establishing a strategy to create porous PEEK without detrimental post processing may help advance the possibilities for patient-specific implants created at the point of care.

In this thesis, porous PEEK created by FFF is presented and characterized to determine its potential use as a novel orthopaedic biomaterial. The porous

architectures are designed using the concept of triply periodic minimal surfaces (TPMS), and design tools are provided for future TPMS-inspired materials. In Aim 1, it was demonstrated that porous PEEK designed as either a simple lattice or TPMS structure can be created via FFF. *In vitro* testing indicated increased preosteoblast cell activity for porous PEEK compared to nonporous, and compression testing showed that the TPMS design led to improved mechanical properties over a simple lattice. In Aim 2, the mechanical properties and degree of anisotropy induced on PEEK by the FFF printing process were explored. The elastic constants to be used in later modeling methods were determined, and relatively low anisotropy for the mechanical properties in two orientations was found. In Aim 3, models were created to relate the architecture and function of the porous PEEK. A custom MATLAB script was created to design and characterize TPMS structures, and the designer inputs were mapped to the resulting pore size and porosity. A homogenization scheme was then used to predict the properties of TPMS architectures, and a relationship between the porous characteristics and predicted elastic modulus was established. The model was validated as a part of Aim 4, in which a family of TPMS-inspired porous PEEK structures were additively manufactured and characterized. A variety of FFF porous PEEK with ranging mechanical properties was achieved, and experimental values showed good agreement with the model for the transverse loading direction, showing promise for a predictive architecture-property model for PEEK TPMS structures.

Chapter 1: Introduction and Background

1.1 Orthopaedic Implant Osseointegration

Musculoskeletal disorders including arthritis, back pain, and bone fractures are the leading contributor to disability worldwide, with an estimated 1.71 billion people globally experiencing some form of these conditions [1]. Orthopaedic procedures designed to address these disorders may include device implantation, as is the case for total joint arthroplasty (TJA), spinal fusion, and bone defect repair. The long-term success of these treatments often relies on secure fixation at the implant-bone interface, and failing to sufficiently achieve and maintain this fixation can result in major complications [2, 3]. Unfortunately, implant loosening remains one of the most common failure methods for total joint arthroplasty [3], and strategies to improve fixation with polymethyl methacrylate (PMMA) bone cement or additional instrumentation come with significant disadvantages [4, 5]. For spinal fusions, titanium cages designed for achieving osseointegration have been associated with increased rates of subsidence into the vertebral bodies [6]. Such complications can ultimately lead to treatment failure, which often require complex and costly revision procedures [3]. With significant increases in volume expected for a number of orthopaedic procedures [7, 8], the development of advanced biomaterials designed to ensure long-term fixation with bone is essential.

Implant fixation can be achieved through osseointegration, in which an implant is incorporated into living bone under normal loading conditions with no relative movement between the implant and bone in contact [9, 10]. This process begins with the initial fixation of the device, in which the implant must be stable and interlocked with native bone. With proper mechanical fixation, the interfacial healing pathway and biological attachment can then occur [2]. Interfacial healing, like bone fracture healing, begins with an immune response, vascularization of the area, and recruitment of skeletal progenitor cells [11]. In interfacial healing, all skeletal progenitor cells differentiate directly into osteoblasts, which secrete a collagen-proteoglycan matrix leading to calcification and bone formation [11, 12]. For patient-specific implants (PSI), that is, those designed based on the patient's native bone structure, improved initial fixation and more natural biomechanics may bolster osseointegration [13-15]. Achieving implant fixation through osseointegration is possible through highly textured or porous materials. Metallic implant surfaces have therefore evolved from solid and smooth, requiring additional fixation hardware, to more roughened [10, 16]. Currently, highly porous surfaces are emerging as a leading choice for implant surface coatings, as their structural similarity to natural bone supports osseointegration (**Figure 1**) [4, 10, 17, 18]. The interconnected pores of these surfaces create scaffolding that mimics bone morphology, provides anchorage for cell attachment, and allows for vascularization, thus exhibiting inherent osteoconductivity [17].

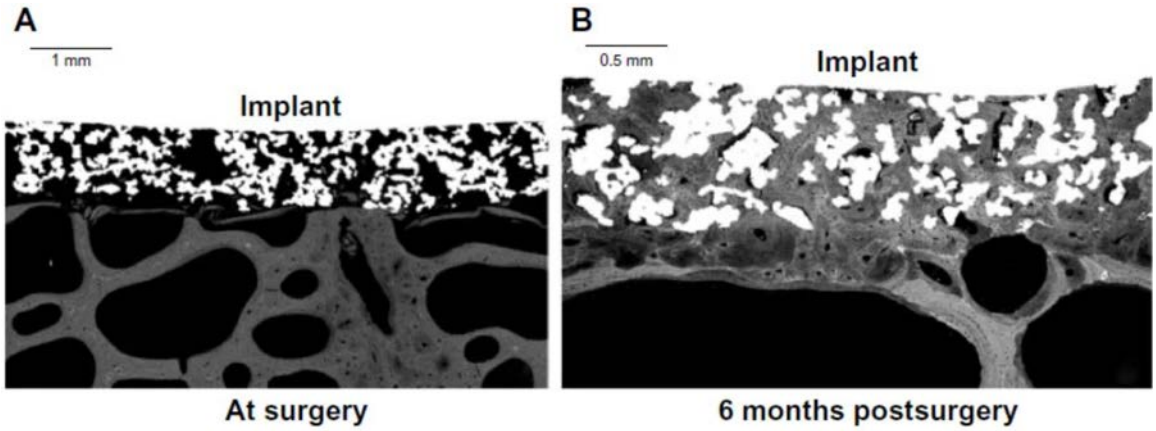

Figure 1. A representative set of BSE micrographs showing the ingrowth and interdigitation of new bone tissue into the porous, coated region at 6 months post-surgery (B) compared with time 0 (at surgery), when the implant was placed in close apposition with the host bone (A). The image shows porous coating (white), bone (gray), and marrow cellular components (black). Reprinted from Isaacson and Jeyapalina [10] with permission from Dove Medical Press.

1.2 Orthopaedic Implant Materials

In addition to implant surface structure, successful osseointegration relies on the biocompatibility and composition of the material implanted. Currently, orthopaedic and spinal implants are commonly manufactured from metallic biomaterials such as titanium alloy and cobalt-chromium (CoCr). These materials, however, exhibit low wear resistance, greater moduli of elasticity compared to bone (leading to bone stress shielding and reduced osseointegration), and may not be suitable for patients with certain metal sensitivities [15, 19]. Metals also have the potential to corrode and release metallic debris into the periprosthetic tissue, which is a potential cause of implant loosening [15, 20]. For these reasons,

polyetheretherketone (PEEK) has recently gained popularity as an alternative biomaterial for orthopaedic devices. PEEK is a thermoplastic polymer within the PAEK (polyaryletherketone) family with a modulus of elasticity similar to bone, natural radiolucency, and biocompatible wear debris [13, 14, 19, 21, 22]. Already, machined PEEK has been successfully used for cranial, dental, and spinal implants, and more orthopaedic uses are anticipated [21]. Some researchers even expect the introduction of all-polymer knee devices using PEEK [15, 19], with one study by de Ruiter et al. comparing CoCr and PEEK femoral components under gait cycle loading [23]. The study reports differences in the stress patterns observed for each material type and found that the cement interface between component and bone underwent greater loading for CoCr compared to PEEK [23].

Whether metallic or not, there is significant interest in adapting the implant surface to achieve cementless fixation given its potential for preserved bone stock and elimination of cement debris [5, 19, 24]. This has become especially important as the mean age of patients undergoing total joint arthroplasty is decreasing and longevity of the population is increasing [8, 25]. Highly porous surfaces are therefore gaining attention for a variety of materials, and the cost and difficulty associated with creating porous ingrowth materials traditional machining methods has contributed to the adoption of additive manufacturing for implant manufacturing.

1.3 Medical Additive Manufacturing

Additive manufacturing (AM, 3D printing) has been used in the medical field for a variety of materials and applications. Among the most common applications are surgical guides, teaching and training aids, and prosthetic devices, with a growing number of implantable device applications as well [26-30]. AM provides the possibility of creating PSI with relatively low costs and lead times, and already the technology has been widely adopted for dental, cranio-maxillofacial, and orthopaedic reconstruction procedures [28-30]. The number of hospitals having AM facilities in-house or nearby has been growing in recent years, and demand for patient specific implants is growing along with the considerable interest in creating implants at the point of care [28, 31]. There are several technologies used 3D printing including fused filament fabrication (FFF), stereolithography (SLA), selective laser sintering or melting (SLS, SLM), and electron beam melting (EBM), each having its own advantages and disadvantages in terms of speed, cost, ease of use, and part properties and quality [27]. There is a range of materials that can be used with each system, though the techniques for metal and polymer printing can differ greatly.

AM of metal components utilizes a high powered energy source, such as a laser or electron beam, to produce a three dimensional part by selectively melting metal powder or wire feedstock, layer by layer, to produce complex geometries with near net shape production and low material waste [32]. However, in addition to the common concerns regarding metal implants (e.g. harmful wear debris, long-term metal ion release [33, 34]), AM of metallic components is complex and introduces a

host of issues including high levels of residual stress, increased surface roughness, and anisotropic microstructure [34-37]. This results in worsened fatigue, ductility, and porosity, which requires post process heat treatment, additional surface machining, CT inspection, and/or isostatic pressing [37-40]. These issues, the necessity of post-processing, and the material hazards (i.e. flammability and health risks associated with metal powder handling) raise significant concern for point of care AM applications and limit the potential for patient-specific metal implants without high costs and long lead times [28].

In the fused filament fabrication process, material filament is melted by a heated nozzle and deposited in successive microscopic layers to create a component from the bottom up (**Figure 2**). For parts with overhanging features, supports are typically printed and removed in postprocessing, though the introduction of dual extrusion with two materials, including dissolvable and easy-to-remove support material, can reduce the effort associated with support removal [41]. So far, the use of FFF in clinical settings has been mostly restricted to low temperature polymers with relatively low strength. However, FFF printing of high temperature implantable polymers like PEEK has recently become possible [13, 29, 42]. Given its low initial machine cost and ease of use compared to laser-based printing methods, FFF is poised to further pave the way to PSI manufacturing at or near the point of care.

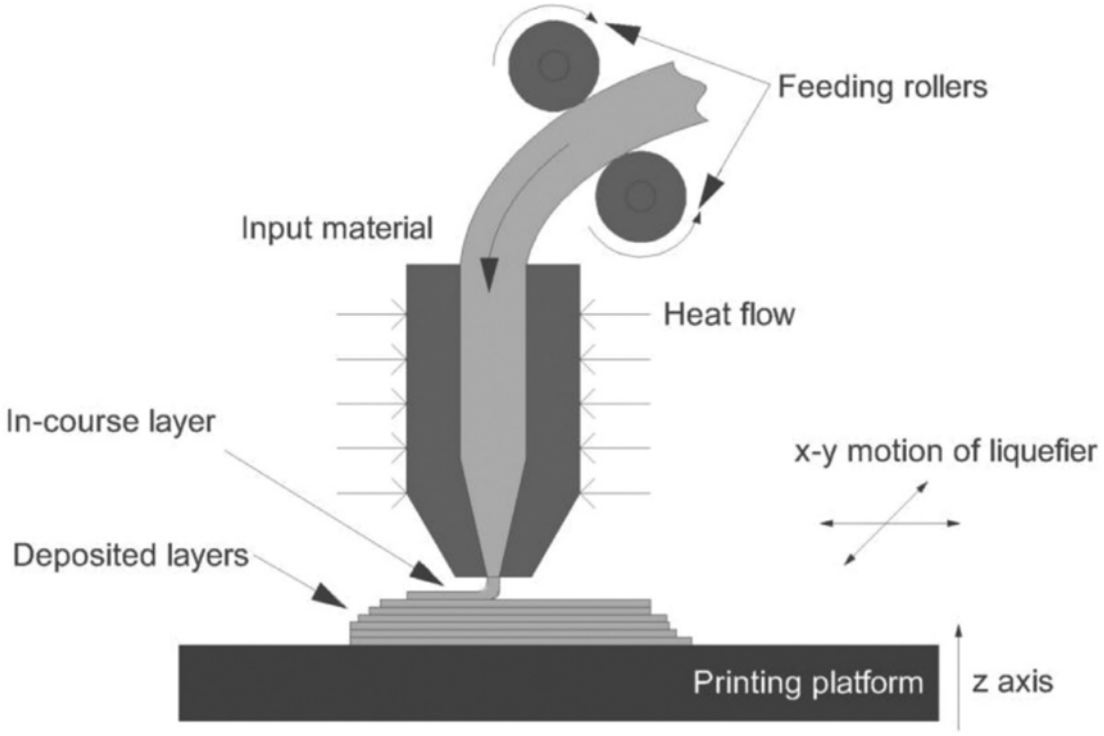

Figure 2. Schematic representation of a Fused Filament Fabrication process. Reprinted from Jerez-Mesa et al. [43] with permission from Elsevier.

1.3.1 3D Printed Biomaterials for Orthopaedic Applications

The ability to create complex structures using 3D printing has led to development of advanced bone ingrowth surfaces with traditional (i.e., metallic) implant materials (**Figure 3**) [4, 18]. While each of the laser-based printing techniques can be applied to a variety of materials, titanium or titanium alloys such as Ti6Al4V are the

most commonly used for bone ingrowth surfaces. Some early studies examined 3D printed porous titanium at a relatively fundamental level, with two studies focusing on long-term bone healing at 26 weeks of implantation [44, 45]. In one of these studies, Palmquist et al. described the successful bone ingrowth both around and inside a pTi scaffold, with significantly less fibrous capsule growth compared to solid Ti [44]. In the other, Shah et al. focused on bone composition instead of bone amount, reporting that tissue maturation was more advanced for porous implants compared to solid [45]. Commercially 3D printed porous titanium has been used experimentally for joint arthroplasty implants, interbody fusion cages, and bone reconstruction components, and considerable success has been reported clinically for pTi in hip arthroplasty cups [4, 46], metaphyseal cones [47, 48], and patient-specific bone reconstructions [49, 50].

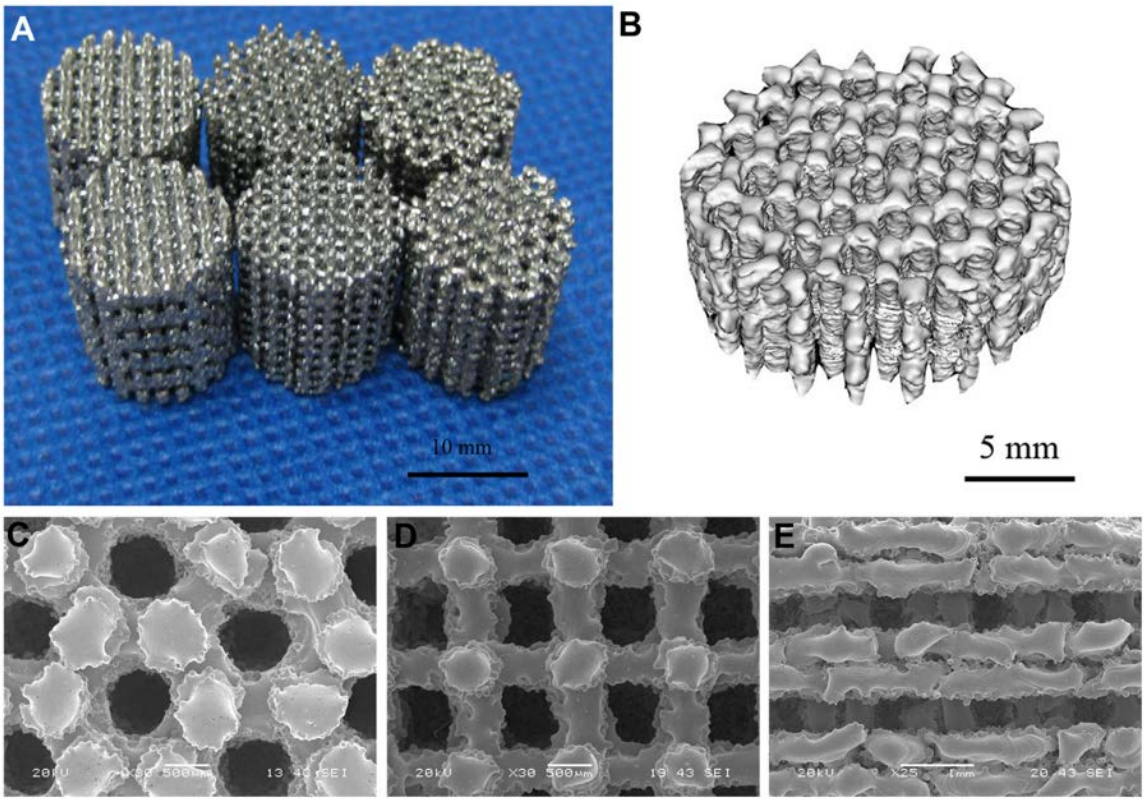

Figure 3. (A) Porous Ti6Al4V scaffolds created by EBM. (B) Reconstructed 3D image of scaffold with honeycomb-like structure. SEM images of scaffolds with (C) honeycomb structure, (D) orthogonal structure, and (E) layer structure. Reprinted with permission from Li et al. [18]

Alternatively, fused filament fabrication (FFF) allows for the creation of complex structures while avoiding the hazards and complexities of metal AM. While some hospitals have already adopted FFF for creating custom non-implantable instruments, this method has thus far been suitable only for low-temperature plastics with relatively poor mechanical properties. Only recently, innovations in

FFF have allowed for the printing of implantable, high-performance polymers such as polyetheretherketone (PEEK). While relatively few studies discuss FFF of PEEK, the results have been encouraging with regard to mechanical performance [51-54]. In one study, Basgul et al. compared 3D printed and machined PEEK spinal cages, reporting that the printed cages demonstrated 63-92% the strength of machined cages for different loading conditions [53]. Similarly, Yang et al. measured maximum tensile strengths of 84 MPa for FFF PEEK and noted a molded PEEK strength of 100 MPa for comparison [54]. This study also reports that a significant factor in achieving desirable properties for FFF PEEK is temperature control [54], which importantly is becoming a focus of new generation printers [55].

Although concerns have been raised about the bioinert nature of PEEK and its limited interaction with bone, the creation of porous networks has shown promising results for bone ingrowth [22, 56-59]. So far, porosity in PEEK has mainly been achieved by methods including chemical modification, salt leaching, grit blasting, and plasma treatment, though the disadvantages of some of these processes include complexity in processing, lack of control in pore sizing, and reduced strength [59-64]. For additive manufacturing, most research on the creation of porous PEEK includes composite materials or chemically induced porosity, with very few reports of virgin PEEK with tunable pore structures. One study with promising results comes from Roskies et al. who performed *in vitro* testing for porous PEEK created via SLS [65]. It was reported that the porous structure, which was designed as a

network of repeating trabecular subunits, maintained cell viability for adipose and bone marrow derived mesenchymal stem cells [65]. However, similar to AM of metal, SLS processing of PEEK involves undesirable powder handling and waste, and is complicated by particle morphology and size distribution [66]. While there are few instances of porous PEEK created via FFF [67-70], the structures have been limited to simple rectilinear lattices.

1.3.2 Triply Periodic Minimal Surfaces

For PEEK, 3D printed porous structures have thus far consisted of simple rectilinear patterns or random pore architecture [65, 71, 72]. However more complex forms have been investigated for other materials using designs created stochastically, often with Voronoi patterning, or using a defined tessellating geometry [73]. Increasingly, and for metal printing especially, researchers are investigating the porosity achieved using triply periodic minimal surfaces (TPMS, **Figure 4**). The complexity of TPMS-based structures makes them difficult and potentially impossible to create by traditional manufacturing, but their continuous surfaces and lack of self-intersections are fitting for creation by 3D printing [74-77]. Like standard minimal surfaces, TPMS structures are based on the principles of area minimization and thus have a mean curvature of zero [77, 78]. TPMS structures, however, also display symmetry in three directions, leading to desirable structural, mechanical, and mass transport properties [74, 77]. Due to their high surface area-to-volume

ratio and permeable pore architecture, TPMSs are particularly well-suited for creating porous networks that mimic trabecular bone and aid in bone ingrowth [76, 77, 79, 80]. Additionally, the surfaces' smooth convergence of struts helps to alleviate stress concentrations typically seen at the sharp joints of strut-based lattices [81, 82].

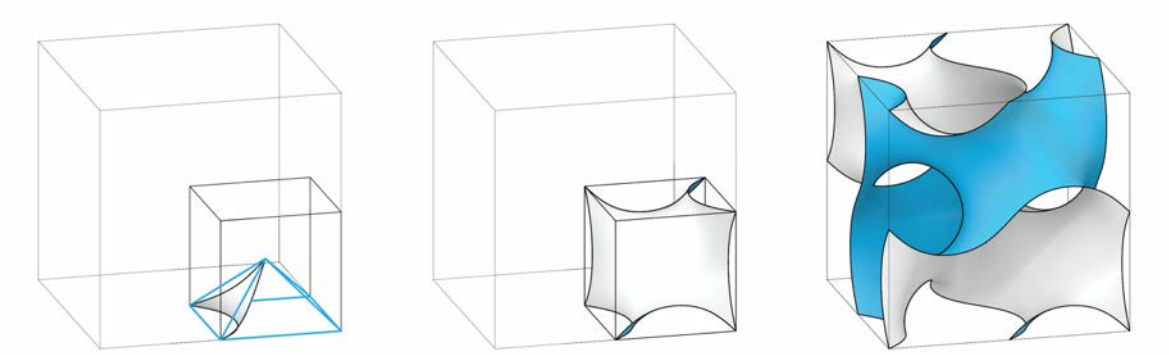

Figure 4. Evolution of a gyroid TPMS from a minimal surface patch. Image reprinted from https://wewanttolearn.wordpress.com/2019/02/03/triply-periodic-minimal-surfaces with permission from author.

TPMSs can be found in nature, with the gyroid microstructure of butterfly wings being a common example [83], and they may also be modeled using a few different methods [84]. The structures can be defined parametrically using the Enneper-Weierstrass representation, though the necessary functions are known only for a very small subset of TPMSs [84-86]. Alternatively, boundary methods, which

involve the iterative refinement of a polygonal model to calculate a minimal surface within the given boundary, can be used [84]. Finally, the structures can be modeled implicitly using nodal approximation equations determined from Fourier series [84, 85, 87], which is perhaps the most common method used for biomedical applications. The research presented in the current work uses these approximation equations and focuses specifically on the gyroid and diamond TPMSs (**Figure 5**), discovered by Schoen and Schwarz, respectively [88].

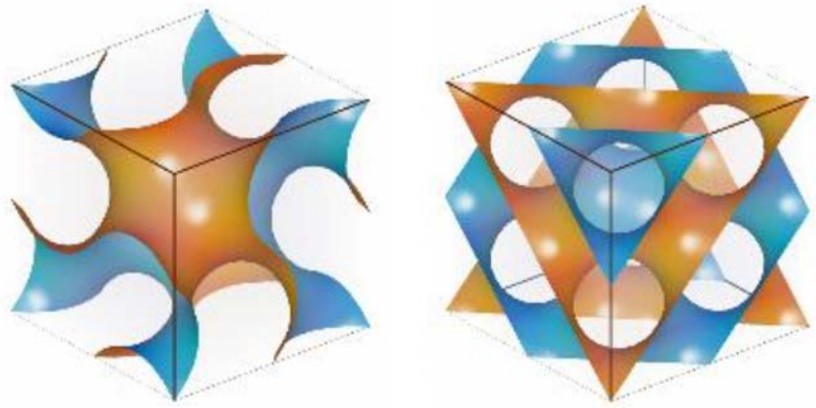

Figure 5.(Left) gyroid and (right) diamond TPMS geometries. Reprinted from The Scientific Graphics Project under the copyright notice at [89].

1.4 Mechanical Properties of Porous Biomaterials

For bone ingrowth surfaces, successful osseointegration depends not only on the structure's architecture but also on its mechanical properties. First, these materials must be strong enough to withstand impaction during initial fixation and other

expected loading scenarios. Second, they must have an elastic modulus similar enough to native bone to reduce the issue of stress shielding sometimes seen with metallic implants [16, 90]. Adding porosity to a material affects each of these properties, and the ability to control the porous architecture, and subsequently the mechanical response, is an extraordinary advantage of 3D printing.

Porous structure and property tunability through AM have been demonstrated for a number of orthopaedic biomaterials including titanium and ceramic [91-94]. In one study from Arabnejad et al., porous metal structures were created using SLM for two unit cell geometries, a tetrahedron and octet truss, and with multiple porosities [93]. Compression tests showed that a range of mechanical properties were achievable with Young's modulus tending to decrease with increasing porosity, and that the 3D printed samples demonstrated a strength up to 5 times greater than clinically-used porous tantalum foam. Further, the study included an *in vivo* canine model which showed a difference in bone ingrowth based on structure porosity [93]. In another study, Vijayavenkataraman et al. additively manufactured TPMS structures from Alumina with the goal of mitigating hip implant stress-shielding [92]. Despite considerable error between the as-designed and actual porosities, the study reports elastic modulus values similar to natural bone and a trend of decreasing stiffness with increasing porosity [92]. For PEEK specifically, mechanical properties similar to bone have been achieved for porous structures created using 3D printing and surface treatments, though the latter

method provides limited control over porous architecture for tuning mechanical properties [22, 64]. The few instances of 3D printed porous PEEK have been based on simple lattice structures, and the properties of TPMS-inspired PEEK remain to be seen.

1.4.1 Anisotropy in Bone and Other Porous Materials

Although current porous biomaterials are designed to generally imitate native bone's mechanical properties, the anisotropy of bone is not often replicated. The degree of anisotropy in both cortical and trabecular bone is determined by the composition and organization of their constituents [95-97]. On one hand, cortical bone is solid and dense, being composed of closely packed osteons. On the other hand, trabecular bone has a more porous structure consisting of a network of plate and rod-shaped bone. Owing in part to these structural differences, the elastic behavior of cortical bone is often considered transversely isotropic with greater strength and stiffness parallel to the long axis of the bone [95, 97], while trabecular bone is best described as orthotropic [96]. Despite efforts to mimic the mechanical properties of bone, anisotropic behavior is often not reflected in implant materials [98]. With additive manufacturing, however, anisotropy can be achieved through the porous structure architecture, through the printing method itself, or through additives such as carbon fiber [98, 99]. An example of the first is provided in a study from Xu et al. who designed several truss-based unit cells and modeled their

directional Young's moduli [98]. It was found that spatial distribution of the moduli were governed by the arrangement of rods within each structure, leading to the suggestion of controlling anisotropy with techniques including rod diameter adjustments and combining unit cells with complementary stiffnesses [98]. For anisotropy resulting from additive manufacturing, the degree of anisotropy depends greatly on the method of printing and the specific parameters (e.g. layer height, print orientation, process temperature) used [100, 101]. FFF in particular has been shown to result in transversely isotropic material properties, as bonding between layers is often affected by undesirable melting and cooling conditions [43, 99, 101, 102]. While some investigations into the mechanical properties of FFF PEEK have been conducted, results have so far been limited to tensile testing conditions, single direction printing, and nonporous samples [103].

1.4.2 Modeling and Prediction of Mechanical Properties

Predictive modeling is an indispensable step in the design of medical devices, and for 3D printed biomaterials specifically, it can be especially useful for optimizing a porous structure or preclinically assessing PSI biomechanics. Several approaches can be used to model the mechanical properties of porous materials with each method having its own benefits and limitations. In this work, an approach using homogenization of representative volume elements is used.

Representative Volume Elements

From a mechanical point of view, porous materials, including TPMS-based structures, can be modelled as a heterogeneous material with two phases: the constituent material and the void space. Because the exact determination of effective elastic properties for heterogeneous materials is generally not possible, rigorous bounds are often estimated instead [104]. A number of techniques can be used to establish upper and lower bounds for effective elasticity, with the Hashin-Shtrikman and Reuss-Voigt bounds being particularly common [104]. As for cellular solids, Gibson and Ashby used analytical methods based on beam theory to propose well-known semi-empirical relationships between structure density and effective mechanical properties including elastic modulus and yield strength [105, 106]. In the same vein, the concept of a representative volume element (RVE), first formally defined by Hill in 1963, is often used in the estimation of effective material properties [107]. The RVE is the smallest volume of a material that can represent its macroscale characteristics, thus making it an important tool for studying material properties such as mechanical response or thermal conductivity. In order to be typical of the overall structure, the RVE must be large enough to capture samplings of all the microstructural heterogeneities in the material [108, 109]. Analyzing an RVE under boundary conditions (BCs) such as uniform displacement or traction allows one to predict the effective stiffness that can be considered representative of

the entire structure [107, 108, 110]. The relationship between average (macroscopic) and local (microscopic) strain can also be determined in the process.

Asymptotic Homogenization

Analytical methods have been used extensively for predicting the mechanical response of materials. However, analyzing the micromechanics of a porous structure with complex geometry can be extremely difficult and computationally costly [111, 112]. To mitigate this, a homogenization method which uses an asymptotic expansion of the relevant governing equations can be implemented to predict the effective properties of RVEs.

The theory of homogenization arose in the 1970's from the study of partial differential equations with rapidly varying coefficients [108]. The basic working principles of the theory allow one to describe a heterogeneous material by determining the effective properties of an equivalent homogenized material, often using the numerical method of asymptotic expansion (**Figure 6**). Traditionally, homogenization theory includes two assumptions [108, 110, 113, 114]. The first is that the field examined (i.e., deformation in the case of elasticity modeling) varies on multiple spatial scales given the presence of a microstructure within a greater macrostructure. In general, the macroscopic scale is relevant to the overall system while the microscopic scale is associated with the material heterogeneities [104, 111], with quantities on the microscale fluctuating more rapidly [108, 110]. The second

traditional assumption is that the microstructure comprising the macrostructure is spatially periodic [108, 110], though it should be noted that homogenization can also be implemented for non-periodic structures [115]. In this work, periodic boundary conditions will be applied to the RVE [113].

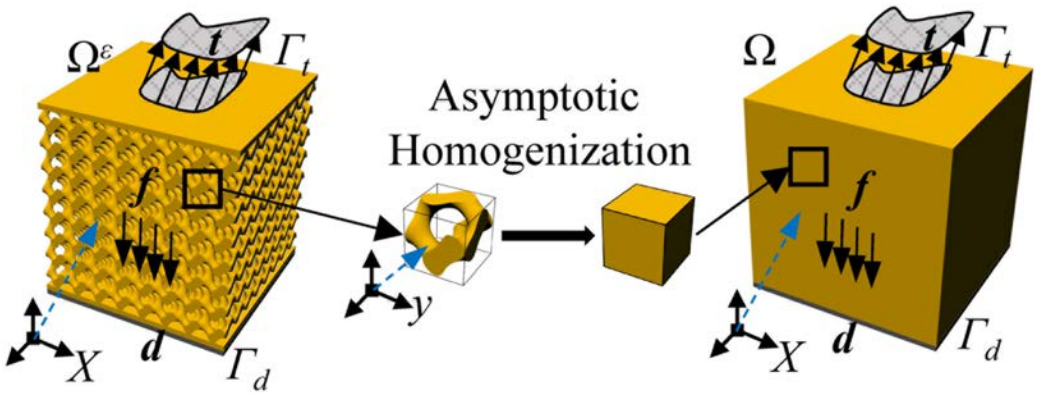

Figure 6. Asymptotic homogenization concept of a cellular structure. Image reprinted from Li et al. [114] with permission from the American Society of Mechanical Engineers.

In elasticity theory specifically, homogenization can be used to approximate a relevant field variable (i.e., displacement) of a microstructured material using the asymptotic expansion [108]:

$$u_i^{\eta}(x_i, y_i) = u_{0i}(x_i, y_i) + \eta u_{1i}(x_i, y_i) + \eta^2 u_{2i}(x_i, y_i) + \cdots \qquad (1.1)$$

where u_i^η is the total displacement, u_{0i} is the macroscopic (average) displacement, and u_{1i}, u_{2i}, etc. are perturbations in displacement due to the microstructure. x_i represents the macroscopic level (also called continuum level) coordinates, y_i represents the microstructural level coordinates, and η is the ratio of the microstructure size to the total size of the analysis region. The accuracy of this homogenization concept has been extensively studied and notably, it has been shown that error decreases as η decreases for periodic materials [110]. Applying the chain rule to the asymptotic expansion of displacement (Equation 1.1) gives the equation for the deformation strain tensor as:

$$\varepsilon_{ij}(u) = \frac{1}{2}\left(\frac{\partial u_i^\eta}{\partial x_j} + \frac{\partial u_j^\eta}{\partial x_i}\right) = \frac{1}{2}\left[\left(\frac{\partial u_{0i}}{\partial x_j} + \frac{\partial u_{0j}}{\partial x_i}\right) + \left(\frac{\partial u_{1i}}{\partial y_j} + \frac{\partial u_{ij}}{\partial y_i}\right) + \eta\left(\frac{\partial u_{1i}}{\partial x_j} + \frac{\partial u_{ij}}{\partial x_i}\right)\right] + h.o.t. \quad (1.2)$$

where h.o.t. stands for higher order terms. Neglecting higher order terms allows the strain tensors to be written as

$$\varepsilon_{ij}(u) = \bar{\varepsilon}_{ij}(u) + \bar{\varepsilon}_{ij}^*, \qquad \bar{\varepsilon}_{ij}(u) = \frac{1}{2}\left(\frac{\partial u_{0i}}{\partial x_j} + \frac{\partial u_{0j}}{\partial x_i}\right), \qquad \varepsilon_{ij}^*(u) = \frac{1}{2}\left(\frac{\partial u_{1i}}{\partial y_j} + \frac{\partial u_{1j}}{\partial y_i}\right) \quad (1.3)$$

where ε_{ij} is the microstructural strain tensor, $\bar{\varepsilon}_{ij}$ is the macroscopic strain tensor, and ε_{ij}^* is the fluctuating microstructural strain tensor which is assumed to vary

periodically. Similarly, the virtual displacement can be expanded asymptotically with higher order terms neglected to give the virtual strain tensors as:

$$\varepsilon_{ij}(v) = \varepsilon_{ij}^{0} + \varepsilon_{ij}^{1}, \qquad \varepsilon_{ij}^{0}(v) = \frac{1}{2}\left(\frac{\partial v_{0i}}{\partial x_j} + \frac{\partial v_{0j}}{\partial x_i}\right), \qquad \varepsilon_{ij}^{1}(v) = \frac{1}{2}\left(\frac{\partial v_{1i}}{\partial y_j} + \frac{\partial v_{1j}}{\partial y_i}\right) \tag{1.4}$$

where $\varepsilon_{ij}(v)$ denotes virtual strain. The expanded forms of these strain tensors can then be substituted into the standard weak form of the equilibrium equation, written as

$$\int_{\Omega^{\eta}} C_{ijkl}\varepsilon_{ij}(v)\varepsilon_{kl}(u)d\Omega^{\eta} = \int_{\Gamma} t_i v_i \, d\Gamma \tag{1.5}$$

where C_{ijkl} is the stiffness tensor, Ω^{η} represents the total domain (macroscopic + microscopic) of the periodic material, $v_i$is the virtual displacement, Γ represents the macroscopic domain boundary, and t_i is the traction applied only to the macroscopic material boundaries. More information on the derivation of Equation 1.5 can be found in publications describing the RVE method [108, 113, 116]. The substitution of the strain tensors into the standard weak form of the equilibrium equation gives

$$\int_{\Omega^\eta} C_{ijkl}(\varepsilon_{ij}^0(v) + \varepsilon_{ij}^1(v))(\bar{\varepsilon}_{kl} + \varepsilon_{kl}^*)d\Omega^\eta = \int_\Gamma t_i v_i \, d\Gamma. \tag{1.6}$$

Because v is an arbitrary (virtual) function, it can be assumed to vary on either the microscopic or macroscopic level. Allowing v to vary on the microscopic level, it will remain constant on the macroscopic level ($\varepsilon_{ij}^0(v) = 0$), with the resulting microscopic equilibrium equation written as

$$\int_{\Omega^\eta} C_{ijkl}\varepsilon_{ij}^1(v)(\bar{\varepsilon}_{kl} + \varepsilon_{kl}^*)d\Omega^\eta = 0. \tag{1.7}$$

Assuming η (ratio of microstructure size to the total analysis region size) goes to zero, Equation 1.7 can be written as

$$\int_\Omega \frac{1}{|V_{RVE}|}\int_{V_{RVE}} C_{ijkl}\,\varepsilon_{ij}^1(v)(\bar{\varepsilon}_{kl} + \varepsilon_{kl}^*)dV_{RVE}d\Omega = 0. \tag{1.8}$$

Equation 1.8 can be satisfied by setting the integral over the RVE as zero, leading to

$$\int_{V_{RVE}} C_{ijkl}\varepsilon_{ij}^1(v)\varepsilon_{kl}^* dV_{RVE} = -\int_{V_{RVE}} C_{ijkl}\,\varepsilon_{ij}^1(v)\bar{\varepsilon}_{kl}dV_{RVE}. \tag{1.9}$$

Though the strain is typically not known prior to solving, the problem can be solved using an arbitrary $\bar{\varepsilon}_{kl}$. The discretization and solving of the homogenization equation are included in **Chapter 4**.

1.5 Overview of Specific Aims

The overall goal of this work is to explore the use of fused filament fabrication to create porous PEEK for bone ingrowth applications and to determine the effect of design and print parameters on the mechanical properties. A sub-goal of this work is to provide methods to assist in the design of TPMS-based structures for achieving porosity with 3D printed materials. It is hypothesized that designing the porous PEEK after TPMS geometries will allow for highly customizable porous structures which support the biological process necessary for osseointegration and display mechanical properties suitable for use in orthopaedic implants. The goals of this thesis will be achieved through the following Specific Aims:

Specific Aim 1: Design and manufacture porous PEEK constructs via fused filament fabrication and determine the effect of porous geometry on osseogenic ability and mechanical properties. Highly porous materials are commonly used to achieve cementless implant fixation through osseointegration and incorporating porosity in PEEK using laser sintering or surface modification has shown promising results [56-58]. The goal of this aim is to determine the feasibility of creating porous PEEK with lattice and TPMS-based geometries through fused filament fabrication.

A further objective is to preliminarily assess the material's suitability as a bone ingrowth material by investigating both the cell response compared to nonporous PEEK and the compressive behavior.

Specific Aim 2: Determine the orthotropic mechanical properties imparted on PEEK by the fused filament fabrication process used to create porous structures. The FFF printing process has been shown to result in transversely isotropic mechanical properties [51, 52, 102]. However, little is known about the directional properties of FFF PEEK, the constituent material of the porous structures investigated throughout this thesis. In this aim, solid (nonporous) PEEK will be additively manufactured with the same print parameters (e.g., nozzle temperature, speed, layer height) used for creating porous PEEK structures, and the resulting elastic behavior and degree of anisotropy will be determined. The results of this aim will contribute to the material property modeling in Specific Aim 3.

Specific Aim 3: Develop a design tool for guiding the creation of gyroid and diamond triply periodic minimal surface structures and model the relationship between the resulting architecture and the predicted elastic modulus for 3D printed porous PEEK. More and more researchers are exploring triply periodic minimal surfaces to achieve desirable material properties, and a visualization of the interplay between TPMS design parameters and resulting structure can be a useful tool across many different applications. The goal of this aim is to create such a model and to

determine the relationship between architecture and mechanical properties for TPMS-inspired PEEK. Numerical homogenization is used to predict the elastic modulus of the porous structures, which will be validated in Specific Aim 4.

Specific Aim 4: Investigate the elastic behavior of 3D printed porous PEEK to validate the architecture-property model created in Aim 3. Predictive models are an important tool in understanding the behavior of biomaterials, though experimental validation of such models is needed to determine their efficacy. The goal of this aim is to investigate the effect of porous characteristics on the compressive mechanical properties of diamond TPMS-based PEEK structures with a range of pore sizes, porosities, and strut thicknesses. Results will be compared to the model created in Specific Aim 3.

Ultimately, the results presented in this thesis further the understanding of porous PEEK as an osseointegrative biomaterial, potentially providing an alternative to metallic and cement-based forms of implant fixation. This work has the potential to further advance the use of FFF AM for point of care manufacturing and the creation of affordable patient-specific implants.

1.6 References

1. Cieza, A., et al., Global estimates of the need for rehabilitation based on the Global Burden of Disease study 2019: a systematic analysis for the Global Burden of Disease Study 2019. The Lancet, 2020. **396**(10267): p. 2006-2017.

2. Gittens, R.A., et al., Implant osseointegration and the role of microroughness and nanostructures: lessons for spine implants. Acta biomaterialia, 2014. **10**(8): p. 3363-3371.

3. Postler, A., et al., Analysis of total knee arthroplasty revision causes. BMC musculoskeletal disorders, 2018. **19**(1): p. 1-6.

4. Malahias, M.-A., et al., Highly porous titanium acetabular components in primary and revision total hip arthroplasty: a systematic review. The Journal of Arthroplasty, 2020. **35**(6): p. 1737-1749.

5. Newman, J.M., et al., Cementless Total Knee Arthroplasty: A Comprehensive Review of the Literature. Orthopedics, 2018. **41**(5): p. 263-273.

6. Duncan, J.W. and R.A. Bailey, An analysis of fusion cage migration in unilateral and bilateral fixation with transforaminal lumbar interbody fusion. European Spine Journal, 2013. **22**(2): p. 439-445.

7. Sloan, M., A. Premkumar, and N.P. Sheth, Projected volume of primary total joint arthroplasty in the US, 2014 to 2030. JBJS, 2018. **100**(17): p. 1455-1460.

8. Kurtz, S., et al., Prevalence of primary and revision total hip and knee arthroplasty in the United States from 1990 through 2002. J Bone Joint Surg Am, 2005. **87**(7): p. 1487-97.

9. Mavrogenis, A.F., et al., Biology of implant osseointegration. J Musculoskelet Neuronal Interact, 2009. **9**(2): p. 61-71.

10. Isaacson, B.M. and S. Jeyapalina, Osseointegration: a review of the fundamentals for assuring cementless skeletal fixation. Orthopedic Research and reviews, 2014. **6**: p. 55-65.

11. Colnot, C., et al., Molecular analysis of healing at a bone-implant interface. J Dent Res, 2007. **86**(9): p. 862-7.

12. Gilbert, S., Osteogenesis: The Development of Bone, in Developmental Biology. 2000, Sinauer Associates: Sunderland

13. Honigmann, P., et al., Patient-Specific Surgical Implants Made of 3D Printed PEEK: Material, Technology, and Scope of Surgical Application. Biomed Res Int, 2018. **2018**: p. 4520636.

14. Carpenter, R.D., et al., Effect of porous orthopaedic implant material and structure on load sharing with simulated bone ingrowth: A finite element analysis comparing titanium and PEEK. J Mech Behav Biomed Mater, 2018. **80**: p. 68-76.

15. Koh, Y.-G., et al., Total knee arthroplasty application of polyetheretherketone and carbon-fiber-reinforced polyetheretherketone: A review. Materials Science and Engineering: C, 2019. **100**: p. 70-81.

16. Lewallen, E.A., et al., Biological strategies for improved osseointegration and osteoinduction of porous metal orthopedic implants. Tissue Eng Part B Rev, 2015. **21**(2): p. 218-30.

17. Karageorgiou, V. and D. Kaplan, Porosity of 3D biomaterial scaffolds and osteogenesis. Biomaterials, 2005. **26**(27): p. 5474-5491.

18. Li, X., et al., Evaluation of biological properties of electron beam melted Ti6Al4V implant with biomimetic coating in vitro and in vivo. PLoS One, 2012. **7**(12): p. e52049.

19. Du, Z., et al., Feasibility and Safety of a Cemented PEEK-on-PE Knee Replacement in a Goat Model: A Preliminary Study. Artificial organs, 2018. **42**(8): p. E204-E214.

20. Hallab, N.J., Biologic Responses to Orthopedic Implants: Innate and Adaptive Immune Responses to Implant Debris. Spine (Phila Pa 1976), 2016. **41 Suppl 7**: p. S30-1.

21. Panayotov, I.V., et al., Polyetheretherketone (PEEK) for medical applications. J Mater Sci Mater Med, 2016. **27**(7): p. 118.

22. Kurtz, S.M. and J.N. Devine, PEEK biomaterials in trauma, orthopedic, and spinal implants. Biomaterials, 2007. **28**(32): p. 4845-69.

23. de Ruiter, L., et al., A preclinical numerical assessment of a polyetheretherketone femoral component in total knee arthroplasty during gait. Journal of experimental orthopaedics, 2017. **4**(1): p. 3.

24. Meng, X., Z. Du, and Y. Wang, Feasibility of Magnetic Resonance Imaging Monitoring of Postoperative Total Knee Arthroplasty without Metal Artifacts: A Preliminary Study of a Novel Implant Model. BioMed research international, 2018. **2018**.

25. Aprato, A., et al., Cementless total knee arthroplasty. Ann Transl Med, 2016. **4**(7): p. 129.

26. Awad, A., et al., 3D printed medicines: A new branch of digital healthcare. International journal of pharmaceutics, 2018. **548**(1): p. 586-596.

27. Aimar, A., A. Palermo, and B. Innocenti, The role of 3D printing in medical applications: a state of the art. Journal of healthcare engineering, 2019. **2019**.

28. Teo, A.Q.A., et al., Point-of-Care 3D Printing: A Feasibility Study of Using 3D Printing for Orthopaedic Trauma. Injury, 2021.

29. Thieringer, F.M., et al. Patient specific implants from a 3D printer–an innovative manufacturing process for custom PEEK implants in cranio-

maxillofacial surgery. in International Conference on Additive Manufacturing in Products and Applications. 2017. Springer.

30. Wong, K.C., 3D-printed patient-specific applications in orthopedics. Orthopedic research and reviews, 2016. 8: p. 57.

31. Sharma, N., et al., Quality Characteristics and Clinical Relevance of In-House 3D-Printed Customized Polyetheretherketone (PEEK) Implants for Craniofacial Reconstruction. Journal of Clinical Medicine, 2020. 9(9): p. 2818.

32. Kruth, J.-P., Material incress manufacturing by rapid prototyping techniques. CIRP annals, 1991. 40(2): p. 603-614.

33. Okazaki, Y., et al., Effects of Ti, Al and V concentrations on cell viability. Materials Transactions, JIM, 1998. 39(10): p. 1053-1062.

34. Trevisan, F., et al., Additive manufacturing of titanium alloys in the biomedical field: processes, properties and applications. Journal of applied biomaterials & functional materials, 2018. 16(2): p. 57-67.

35. Thijs, L., et al., A study of the microstructural evolution during selective laser melting of Ti–6Al–4V. Acta materialia, 2010. 58(9): p. 3303-3312.

36. Yuan, L., S. Ding, and C. Wen, Additive manufacturing technology for porous metal implant applications and triple minimal surface structures: A review. Bioactive Materials, 2019. 4: p. 56-70.

37. Liu, S. and Y.C. Shin, Additive manufacturing of Ti6Al4V alloy: A review. Materials & Design, 2019. 164: p. 107552.

38. Dall'Ava, L., et al., 3D printed acetabular cups for total hip arthroplasty: a review article. Metals, 2019. 9(7): p. 729.

39. Chastand, V., et al., Fatigue characterization of Titanium Ti-6Al-4V samples produced by Additive Manufacturing. Procedia Struct. Integr, 2016. 2: p. 3168-3176.

40. Chastand, V., et al., Comparative study of fatigue properties of Ti-6Al-4V specimens built by electron beam melting (EBM) and selective laser melting (SLM). Materials Characterization, 2018. 143: p. 76-81.

41. Steuben, J., D.L. Van Bossuyt, and C. Turner. Design for fused filament fabrication additive manufacturing. in International Design Engineering Technical Conferences and Computers and Information in Engineering Conference. 2015. American Society of Mechanical Engineers.

42. Rahman, K.M., T. Letcher, and R. Reese, Mechanical Properties of Additively Manufactured PEEK Components Using Fused Filament Fabrication. 2015.

43. Jerez-Mesa, R., et al., Finite element analysis of the thermal behavior of a RepRap 3D printer liquefier. Mechatronics, 2016. 36: p. 119-126.

44. Palmquist, A., et al., Long-term biocompatibility and osseointegration of electron beam melted, free-form-fabricated solid and porous titanium alloy: experimental studies in sheep. J Biomater Appl, 2013. 27(8): p. 1003-16.

45. Shah, F.A., et al., 3D printed Ti6Al4V implant surface promotes bone maturation and retains a higher density of less aged osteocytes at the bone-implant interface. Acta Biomater, 2016. 30: p. 357-367.

46. Castagnini, F., et al., Highly porous titanium cup in cementless total hip arthroplasty: registry results at eight years. International orthopaedics, 2019. 43(8): p. 1815-1821.

47. Denehy, K.M., et al., Metaphyseal Fixation Using Highly Porous Cones in Revision Total Knee Arthroplasty: Minimum Two Year Follow Up Study. The Journal of arthroplasty, 2019. 34(10): p. 2439-2443.

48. Ohlmeier, M., et al., Preliminary clinical results of coated porous tibia cones in septic and aseptic revision knee arthroplasty. Archives of Orthopaedic and Trauma Surgery, 2020: p. 1-6.

49. Wei, F., et al., Upper cervical spine reconstruction using customized 3D-printed vertebral body in 9 patients with primary tumors involving C2. Annals of Translational Medicine, 2020. 8(6).

50. Zou, Y., et al., Novel exploration of customized 3D printed shoulder prosthesis in revision of total shoulder arthroplasty: a case report. Medicine, 2018. 97(47).

51. Arif, M., et al., Performance of biocompatible PEEK processed by fused deposition additive manufacturing. Materials & Design, 2018. 146: p. 249-259.

52. Costa, A.E., A.F. da Silva, and O.S. Carneiro, A study on extruded filament bonding in fused filament fabrication. Rapid Prototyping Journal, 2019.

53. Basgul, C., et al., Structure–property relationships for 3D-printed PEEK intervertebral lumbar cages produced using fused filament fabrication. Journal of materials research, 2018. 33(14): p. 2040-2051.

54. Yang, C., et al., Influence of thermal processing conditions in 3D printing on the crystallinity and mechanical properties of PEEK material. Journal of Materials Processing Technology, 2017. 248: p. 1-7.

55. Singh, S., C. Prakash, and S. Ramakrishna, 3D printing of polyether-ether-ketone for biomedical applications. European Polymer Journal, 2019. 114: p. 234-248.

56. Landy, B.C., et al., Mechanical and in vitro investigation of a porous PEEK foam for medical device implants. J Appl Biomater Funct Mater, 2013. 11(1): p. e35-44.

57. Torstrick, F.B., et al., Getting PEEK to Stick to Bone: The Development of Porous PEEK for Interbody Fusion Devices. Techniques in orthopaedics (Rockville, Md.), 2017. 32(3): p. 158-166.

58. Wang, S., et al., Enhanced antibacterial property and osteo-differentiation activity on plasma treated porous polyetheretherketone with hierarchical micro/nano-topography. Journal of Biomaterials science, Polymer edition, 2018. 29(5): p. 520-542.

59. Torstrick, F.B., et al., Do Surface Porosity and Pore Size Influence Mechanical Properties and Cellular Response to PEEK? Clin Orthop Relat Res, 2016. 474(11): p. 2373-2383.

60. Han, X., et al., An In Vitro Study of Osteoblast Response on Fused-Filament Fabrication 3D Printed PEEK for Dental and Cranio-Maxillofacial Implants. J Clin Med, 2019. 8(6).

61. Hieda, A., et al., In vivo bioactivity of porous polyetheretherketone with a foamed surface. Dent Mater J, 2017. 36(2): p. 222-229.

62. Siddiq, A.R. and A.R. Kennedy, Porous poly-ether ether ketone (PEEK) manufactured by a novel powder route using near-spherical salt bead porogens: characterisation and mechanical properties. Mater Sci Eng C Mater Biol Appl, 2015. 47: p. 180-8.

63. Evans, N.T., et al., Local deformation behavior of surface porous polyether-ether-ketone. J Mech Behav Biomed Mater, 2017. 65: p. 522-532.

64. Harting, R., et al., Functionalization of polyethetherketone for application in dentistry and orthopedics, in BioNanoMaterials. 2017.

65. Roskies, M., et al., Improving PEEK bioactivity for craniofacial reconstruction using a 3D printed scaffold embedded with mesenchymal stem cells. J Biomater Appl, 2016. 31(1): p. 132-9.

66. Berretta, S., K.E. Evans, and O. Ghita, Processability of PEEK, a new polymer for High Temperature Laser Sintering (HT-LS). European Polymer Journal, 2015. 68(Supplement C): p. 243-266.

67. Su, Y., et al., Additively-manufactured poly-ether-ether-ketone (PEEK) lattice scaffolds with uniform microporous architectures for enhanced cellular response and soft tissue adhesion. Materials & Design, 2020. 191: p. 108671.

68. Elhattab, K., et al., Fabrication and evaluation of 3-D printed PEEK scaffolds containing Macropores by design. Materials Letters, 2020. 263: p. 127227.

69. Deng, L., Y. Deng, and K. Xie, *AgNPs-decorated 3D printed PEEK implant for infection control and bone repair.* Colloids and Surfaces B: Biointerfaces, 2017. **160**: p. 483-492.

70. Vaezi, M. and S. Yang, *Extrusion-based additive manufacturing of PEEK for biomedical applications.* Virtual and Physical Prototyping, 2015. **10**(3): p. 123-135.

71. Li, P., et al., *A novel 3D printed cage with microporous structure and in vivo fusion function.* Journal of Biomedical Materials Research Part A, 2019.

72. Tan, K.H., et al., *Scaffold development using selective laser sintering of polyetheretherketone-hydroxyapatite biocomposite blends.* Biomaterials, 2003. **24**(18): p. 3115-23.

73. Tamburrino, F., S. Graziosi, and M. Bordegoni, *The design process of additively manufactured mesoscale lattice structures: a review.* Journal of Computing and Information Science in Engineering, 2018. **18**(4).

74. Ma, S., et al., *Mechanical behaviours and mass transport properties of bone-mimicking scaffolds consisted of gyroid structures manufactured using selective laser melting.* J Mech Behav Biomed Mater, 2019. **93**: p. 158-169.

75. Kelly, C.N., et al., *Fatigue behavior of As-built selective laser melted titanium scaffolds with sheet-based gyroid microarchitecture for bone tissue engineering.* Acta biomaterialia, 2019. **94**: p. 610-626.

76. Zhu, L.Y., et al., *Mechanical characterization of 3D printed multi-morphology porous Ti6Al4V scaffolds based on triply periodic minimal surface architectures.* Am J Transl Res, 2018. **10**(11): p. 3443-3454.

77. Bobbert, F.S.L., et al., *Additively manufactured metallic porous biomaterials based on minimal surfaces: A unique combination of topological, mechanical, and mass transport properties.* Acta Biomater, 2017. **53**: p. 572-584.

78. Kapfer, S.C., et al., *Minimal surface scaffold designs for tissue engineering.* Biomaterials, 2011. **32**(29): p. 6875-82.

79. Liu, F., et al., *Mechanical properties of optimized diamond lattice structure for bone scaffolds fabricated via selective laser melting.* Materials, 2018. **11**(3): p. 374.

80. Zadpoor, A.A., *Bone tissue regeneration: the role of scaffold geometry.* Biomater Sci, 2015. **3**(2): p. 231-45.

81. Khan, S.Z., et al., *Compressive behaviour of Neovius Triply Periodic Minimal Surface cellular structure manufactured by fused deposition modelling.* Virtual and Physical Prototyping, 2019. **14**(4): p. 360-370.

82. Almeida, H.A. and P.J. Bartolo, *Design of tissue engineering scaffolds based on hyperbolic surfaces: structural numerical evaluation.* Med Eng Phys, 2014. **36**(8): p. 1033-40.

83. Han, L. and S. Che, *An overview of materials with triply periodic minimal surfaces and related geometry: from biological structures to self-assembled systems.* Advanced Materials, 2018. **30**(17): p. 1705708.

84. Ambu, R. and A.E. Morabito, *Modeling, assessment, and design of porous cells based on schwartz primitive surface for bone scaffolds.* The Scientific World Journal, 2019. **2019**.

85. Von Schnering, H. and R. Nesper, *Nodal surfaces of Fourier series: fundamental invariants of structured* matter. Zeitschrift für Physik B Condensed Matter, 1991. **83**(3): p. 407-412.

86. Fogden, A. and S. Hyde, *Parametrization of triply periodic minimal surfaces. I. Mathematical basis of the construction algorithm for the regular class.* Acta Crystallographica Section A: Foundations of Crystallography, 1992. **48**(4): p. 442-451.

87. Wohlgemuth, M., et al., *Triply periodic bicontinuous cubic microdomain morphologies by symmetries.* Macromolecules, 2001. **34**(17): p. 6083-6089.

88. Schoen, A.H., *Reflections concerning triply-periodic minimal surfaces.* Interface focus, 2012. **2**(5): p. 658-668.

89. *The Scientific Graphics Project*. Available from: https://www.msri.org/publications/sgp/jim/papers/morphbysymmetry/table/index.html.

90. Kienapfel, H., et al., *Implant fixation by bone ingrowth.* The Journal of arthroplasty, 1999. **14**(3): p. 355-368.

91. Bandyopadhyay, A., et al., *Influence of porosity on mechanical properties and in vivo response of Ti6Al4V implants.* Acta biomaterialia, 2010. **6**(4): p. 1640-1648.

92. Vijayavenkataraman, S., L.Y. Kuan, and W.F. Lu, *3D-printed ceramic triply periodic minimal surface structures for design of functionally graded bone implants.* Materials & Design, 2020: p. 108602.

93. Arabnejad, S., et al., *High-strength porous biomaterials for bone replacement: A strategy to assess the interplay between cell morphology, mechanical properties, bone ingrowth and manufacturing constraints.* Acta biomaterialia, 2016. **30**: p. 345-356.

94. Li, L., et al., *Early osteointegration evaluation of porous Ti6Al4V scaffolds designed based on triply periodic minimal surface models.* J Orthop Translat, 2019. **19**: p. 94-105.

95. Li, S., E. Demirci, and V.V. Silberschmidt, *Variability and anisotropy of mechanical behavior of cortical bone in tension and compression.* Journal of the mechanical behavior of biomedical materials, 2013. **21**: p. 109-120.

96. Marangalou, J.H., et al., *A novel approach to estimate trabecular bone anisotropy using a database approach.* Journal of biomechanics, 2013. **46**(14): p. 2356-2362.

97. Morgan, E.F., G.U. Unnikrisnan, and A.I. Hussein, *Bone mechanical properties in healthy and diseased states.* Annual review of biomedical engineering, 2018. **20**: p. 119-143.

98. Xu, S., et al., *Design of lattice structures with controlled anisotropy.* Materials & Design, 2016. **93**: p. 443-447.

99. Casavola, C., et al., *Orthotropic mechanical properties of fused deposition modelling parts described by classical laminate theory.* Materials & design, 2016. **90**: p. 453-458.

100. Maroti, P., et al., *Printing orientation defines anisotropic mechanical properties in additive manufacturing of upper limb prosthetics.* Materials Research Express, 2018. **6**(3): p. 035403.

101. Zaldivar, R., et al., *Influence of processing and orientation print effects on the mechanical and thermal behavior of 3D-Printed ULTEM® 9085 Material.* Additive Manufacturing, 2017. **13**: p. 71-80.

102. Basgul, C., et al., *Thermal localization improves the interlayer adhesion and structural integrity of 3D printed PEEK lumbar spinal cages.* Materialia, 2020. **10**: p. 100650.

103. Basgul, C., et al., *Structure, properties, and bioactivity of 3D printed PAEKs for implant applications: A systematic review.* Journal of Biomedical Materials Research Part B: Applied Biomaterials, 2021.

104. Torquato, S. and H. Haslach Jr, *Random heterogeneous materials: microstructure and macroscopic properties.* Appl. Mech. Rev., 2002. **55**(4): p. B62-B63.

105. Gibson, L.J. and M.F. Ashby, *Cellular solids: Structure and properties*. 2nd ed. 1997, Cambridge, United Kingdom: Cambridge University Press.

106. Gibson, I. and M.F. Ashby, *The mechanics of three-dimensional cellular materials.* Proceedings of the royal society of London. A. Mathematical and physical sciences, 1982. **382**(1782): p. 43-59.

107. Hill, R., *Elastic properties of reinforced solids: some theoretical principles.* Journal of the Mechanics and Physics of Solids, 1963. **11**(5): p. 357-372.

108. Hollister, S.J. and N. Kikuchi, *A comparison of homogenization and standard mechanics analyses for periodic porous composites.* Computational mechanics, 1992. **10**(2): p. 73-95.

109. Kanit, T., et al., *Determination of the size of the representative volume element for random composites: statistical and numerical approach.* International Journal of solids and structures, 2003. **40**(13-14): p. 3647-3679.

110. Hollister, S.J., J. Brennan, and N. Kikuchi, *A homogenization sampling procedure for calculating trabecular bone effective stiffness and tissue level stress.* Journal of biomechanics, 1994. **27**(4): p. 433-444.

111. Hassani, B. and E. Hinton, *A review of homogenization and topology optimization I—homogenization theory for media with periodic structure.* Computers & Structures, 1998. **69**(6): p. 707-717.

112. Nguyen, C.H.P., Y. Kim, and Y. Choi, *Design for additive manufacturing of functionally graded lattice structures: a design method with process induced anisotropy consideration.* International Journal of Precision Engineering and Manufacturing-Green Technology, 2019: p. 1-17.

113. Sanchez-Palencia, E. and A. Zaoui, Homogenization techniques for composite media. Homogenization techniques for composite media, 1987. 272: p. 194 - 278.

114. Li, D., et al., Design and optimization of graded cellular structures with triply periodic level surface-based topological shapes. Journal of Mechanical Design, 2019. 141(7).

115. Hollister, S.J., et al., Application of homogenization theory to the study of trabecular bone mechanics. Journal of biomechanics, 1991. 24(9): p. 825-839.

116. Bensoussan, A., J.-L. Lions, and G. Papanicolaou, Asymptotic analysis for periodic structures. Vol. 374. 2011: American Mathematical Soc.

Chapter 2: Determining the Feasibility of 3D Printed Porous PEEK Created via Fused Filament Fabrication for Osteoconductive Orthopaedic Surfaces

2.1 Abstract

Due to its unique and advantageous material properties, polyetheretherketone (PEEK) is an attractive biomaterial for implantable devices. Though concerns exist regarding PEEK for orthopaedic implants due to its bioinertness, the creation of porous networks has shown promising results for interaction with surrounding tissue. In this study porous PEEK is created via clinically-available fused filament fabrication (FFF, 3D printing), and the pore structure morphology, mechanical properties, and biologic response are assessed. The designs of the porous structures were based on a simple rectilinear pattern as well as triply periodic minimal surfaces (TPMS), specifically the gyroid and diamond types. The material characteristics, including porosity, yield strength, and roughness, were evaluated using micro-computed tomography (micro-CT), static compression testing, and optical profilometry. The porous PEEK, along with 3D printed solid PEEK, was then seeded with MC3T3-E1 preosteoblast cells for evaluation of cell proliferation and alkaline phosphatase activity (ALP). The samples were then imaged via scanning electron microscopy (SEM) to observe cell morphology. Micro-CT imaging showed the porous networks to be open and interconnected, with porous sizes similar ($p > 0.05$) to the as-designed size of 600 μm. Average compressive properties ranged

from 210 - 268 MPa for elastic modulus and 6.6 – 17.1 MPa for yield strength, with strength being greatest for TPMS constructs. SEM imaging revealed cells attaching to and bridging micro-topological features of the porous constructs, and cell activity was significantly greater for the porous PEEK compared to solid at multiple time points.

2.2 Introduction

In recent years, clinical interest in additive manufacturing (AM), or 3D printing, of biomaterials has been increasing significantly. This is especially true for osteoconductive surfaces used for orthopaedic implant surfaces or bone defect repair, which benefit from complex trabecular-like morphology not achievable by traditional manufacturing. AM methods already have a history of use for creating synthetic osteoconductive materials that, in addition to avoiding morbidities related to auto- or allografts, can be bio-functionalized and highly customized [1-3]. However, there are reported drawbacks to many of these materials, including dimensional inaccuracy and inadequate mechanical properties [1-3]. Even the dominant method for creating AM osteoconductive scaffolds, laser-based metal sintering, comes with significant cost and safety considerations, unlike the extrusion-based fused filament fabrication (FFF) method already being used in-hospital to create custom non-implantable instruments. While FFF has thus far been suitable only for low temperature plastics, recent innovations in FFF have allowed

for the printing of high temperature, implantable polymers such as polyetheretherketone (PEEK), opening the door for more advanced osteoconductive surfaces.

PEEK has a modulus of elasticity similar to bone, high yield strength and fatigue resistance, and natural radiolucency, making it an attractive biomaterial for implantable medical devices [4, 5]. While machined PEEK interbody fusion devices have been used for spinal fusion treatments with positive results since the early 2000's [6], interest in PEEK for total joint arthroplasty (TJA) has recently been growing [7-9]. The success of such implants relies on long-term fixation at the bone-implant interface, currently achieved via cementation or porous metal surfaces. However, significant drawbacks of these methods, including harmful debris generation, damage to host bone through stress shielding, attenuated bone fixation, and high costs have led to a push for alternative orthopaedic bone ingrowth surfaces [7, 9, 10]. And while clinical concerns exist regarding the bioinert nature of PEEK and, consequently, its limited ability to interact with bone to establish fixation, the introduction of porosity has shown promising results for promoting the osteogenic potential of PEEK [11-14]. The interconnected pores of these networks create scaffolding that mimics bone morphology, provides anchorage for cell attachment, and allows for vascularization, thus exhibiting inherent osteoconductivity [15]. This is an alternative to bolstering osteoconductivity through coatings and composites, which can negatively impact mechanical performance, imaging compatibility,

material cost, and ease of manufacturing [12, 16-19]. Methods for creating porous PEEK, which cannot be produced by traditional machining methods, have thus far focused on surface modifications such as sulfonation, salt leaching, plasma treatment, and grit blasting [11-13, 18, 20-23]. While these methods have met a range of success, considerable disadvantages include complex processing, uncontrollable pore size, treatment residue, and reduced strength [12, 20, 21, 23].

In this study, the objective is to manufacture porous PEEK structures via FFF, which offers the benefit of high customizability and tunable pore sizes, ease of production in a hospital setting, and relatively low costs. Several studies have already examined FFF printed PEEK and observed positive cell responses and mechanical properties [5, 20, 24, 25], though similar work has not yet been reported for TPMS-designed PEEK. In addition to characterizing the morphology and mechanical properties of 3D printed porous PEEK, another aim is to assess the resulting *in vitro* cellular response as compared to solid PEEK. It is hypothesized that the porous PEEK structures will promote greater preosteoblast cell viability and activity as compared to solid PEEK controls, and that porous structures designed as triply periodic minimal surfaces will display increased mechanical strength compared to a traditional rectilinear lattice.

2.3 Methods

Scaffold Design

Three different porous constructs, herein referred to as “rectilinear”, “gyroid”, and “diamond” were designed to mimic the morphology of trabecular bone in pore size and porosity. Pore interconnectedness, to aid in cell migration and vascularization during osteogenesis, was considered along with manufacturability by FFF when determining the geometries [26]. The rectilinear structure is a strut-based network of cubic pores created by repeatedly alternating the direction of layer deposition during printing. The gyroid and diamond constructs were designed from repeating unit cells of triply periodic minimal surfaces (TPMS), specifically the Schoen Gyroid and Schwarz Diamond types. The theoretical pore size for each construct was designed to be 600 μm with a 250 μm strut size, and the theoretical porosities were 70%, 74%, and 72% for the rectilinear, gyroid, and diamond constructs, respectively. A pore size of 600 μm was selected based on previous studies regarding optimized pore size for bone ingrowth [27-29]. Models were created using MathMod-9.1 (open source, www.sourceforge.net) and 3ds Max (Autodesk, Inc., San Rafael, CA), and sliced for printing using Simplify3D (Cincinnati, OH).

Scaffold Fabrication

The constructs were additively manufactured via fused filament fabrication using PEEK (PEEK 450G, Victrex, Lancashire, UK) filament. All samples were manufactured with a high temperature polymer FFF 3D printer (Apium P220, Karlsruhe, Germany). Iterative testing of printing parameters such as temperature,

speed, and layer height was performed in order to establish a set of consistent parameters that can be used to print each geometry (**Table 1).** These parameters determined the structure quality by affecting printing conditions including the flow of melted filament, the success of inter-layer adhesion, and the ability of PEEK filament to bridge between underlying struts. Iterative testing was performed once a set of parameters was obtained which could produce sturdy cubes (within 5% of 15 mm for each side) of each porous geometry, with pores that appeared consistent in shape and size under visual inspection. Additionally, the openness of the inner pores was preliminarily examined by holding the cubes up to a light and confirming that the illuminated grid of pores was consistent with the grid seen in the designed model. Solid PEEK cubes were also printed for use as controls using these parameters, though a higher temperature was needed to ensure inter-layer adhesion over the larger surface area. Samples used for mechanical testing were 15 mm cubes, and samples for cell seeding were 10 mm x 10 mm x 2 mm.

Table 1. Final printing parameters used for printing porous and solid PEEK.

Nozzle Size	Layer Height	Nozzle Temperature	Printing Speed
0.2 mm	0.1 mm	420 – 450° C	2200 mm/min

Porous PEEK Topology Characterization

Following manufacturing, four samples (15 mm cubes) of each geometry were imaged using a Scanco micro-CT 80 (Scanco Medical AG, Brüttisellen, Switzerland) at a maximum resolution of 18 microns. The inbuilt 3D Analysis tool was used to determine porosity, calculated as the ratio of void to total volume, and pore size, determined by measurement of spheres fitted into the porous structure. The structures were then rendered in Analyze 12.0 software (AnalyzeDirect, Overland Park, KS) to determine the interconnectivity of the internal pore structures. By establishing intensity thresholds to segment each image, voxels representing PEEK and void space were separated. Image intensities were then inverted to render the PEEK transparent with the internal pores represented as visible volumes. The visible pore structure was then segmented by 6-connected voxels, so that each interconnected section of pores was made distinct from other non-connected pores. A minimal volume size of 0.005 mm^3 was used for defining pores in order to exclude material voids resulting from imperfections in the extruded filament, often a result of moisture uptake. The pore interconnectivity was then taken as the fractional volume of non-connected pores to interconnected pores. Rough contact angle measurements, a measure of material wettability, were also taken on the dry surfaces of the PEEK constructs ($n = 5$ for each geometry). Digital images were taken perpendicular to the 10 μL droplets of distilled water placed on each surface, and the angle tangential to the water-surface interface was directly measured from each image.

Surface microroughness was measured using an optical profiler (NewView™ 9000, Zygo, Middlefield, CT) with a 50x Mirau objective at 1.0x image zoom (n = 3 for each geometry). The measurements were post processed by fitting and removing 4th order terms from the data to remove low order surface curvature and form from the roughness measurements. All measurements were taken within the area of a single PEEK strut in order to capture the microroughness resulting from printing and not the overall structure roughness due to the macropores. Average roughness from a best fit to the test part surface (Sa) and maximum peak-to-valley height (Sz) were recorded.

Static Compression Testing

Five 15 mm cubes of each porous material were mechanically tested to determine the material compressive properties according to ASTM D695-15 [30] and in accordance with ISO 17025 quality system requirements [31]. Testing was conducted using a MTS Mini Bionix 858 system (MTS Systems Corporation, Eden Prairie, MN) equipped with calibrated load and displacement sensors, using a 15kN load cell. Five samples of each geometry were tested at a constant displacement rate of 1.3 mm/min [30], with the load applied perpendicular to the direction of layer deposition until failure. Stress-strain curves were generated from the data, and the modulus of elasticity and yield strength (taken as the 0.2% offset stress) [32] for each

porous design were then determined using a custom script in MATLAB 2019a (MathWorks, Natick, MA) with recommendations in ASTM D695-15 [30] as a guide.

In Vitro Cell Culturing and Imaging

Prior to cell seeding, the 10 mm x 10 mm x 2 mm PEEK constructs were washed and sterilized in UV light and 70% ethanol 3x for 30 minutes each. The PEEK constructs were then incubated in cell culture media overnight. MC3T3-E1 preosteoblast cells were seeded onto the porous PEEK constructs at a cell density of 30,000 cells/construct for 7 and 14 days. Cell proliferation and alkaline phosphatase activity (ALP) were evaluated at each time point (n = 6 for each geometry and timepoint combination). Briefly, the MTT tetrazolium dye was added to each construct for 4 hours at 37°C and solubilized in dimethyl sulfoxide for 10 minutes. The solution was read in a TECAN at 540 nm [33]. For ALP, p-nitrophenol phosphate was added (pNPP) to each construct for 1 hour at room temperature. The ALP enzyme secreted by the cells in culture dephosphorylates the pNPP reagent and turns to a yellow solution, which was read in a TECAN at 405 nm [34].

Additional constructs with cells cultured for 7 days and 14 days (n= 4 for each design and timepoint) and constructs with no cells were imaged using a Zeiss Supra 50VP scanning electron microscope (Zeiss, Oberkochen, Germany) in order to examine the cell morphology at both time points and the PEEK surface topology both with and without cell seeding. Prior to imaging, samples were fixed with

Karnovsky's fixative (2.5% glutaraldehyde and 2% paraformaldehyde) for 30 minutes, dehydrated in a series of increase alcohol concentration, and dried in hexamethyldisilazane for 4 hours. The constructs were sputter coated with platinum/palladium alloy. Micrographs were collected with a secondary electron detector at an accelerating voltage of 20 kV.

Statistical analysis

Differences between the groups of printed PEEK were identified for each dataset resulting from the biological and mechanical testing. Data normality was determined via the Shapiro-Wilk test, and parametric tests were then used when applicable. Differences were determined via Student's t-test for comparisons within each geometry (designed vs. actual pore size) and via one-way ANOVA for biological and mechanical differences between the porous groups. For all analyses, SPSS Statistics 25 (IBM, Armonk, NY) was used, and significance was determined at an alpha value of 0.05.

2.4 Results

Porous scaffold morphology

Imaging via micro-CT scanning and SEM showed the pores in the PEEK constructs to be open and interconnected throughout (**Figure 7**). Average pore size, strut size, and porosity for each design are provided in **Table 2**. The printed scaffolds were

compared with the original CAD designs to determine the error resulting from the printing process. For each geometry, the average pore size and porosities of the scaffolds showed no significant difference ($p > 0.05$) when compared to the as-designed size. The average errors between the designed and actual pore size were -54 μm, 108 μm, and -3.1 μm for the rectilinear, gyroid, and diamond, respectively. The negative difference for the rectilinear and diamond constructs denotes pore shrinkage, whereas the gyroid constructs exhibited larger pores than designed. When the porous networks were segmented to determine pore interconnectivity, multiple instances of disconnected pores were observed, though at an extremely low volumes compared to the connected pore network. In each case, the aggregate volume of non-connected pores was less than 0.5 mm^3, with the volume of connected pores orders of magnitude greater (> 1000 mm^3). Contact angle measurements showed decreased angles, indicating improved wettability, for the TPMS porous surfaces, but the difference was not significant compared to the solid control ($p > 0.05$). The rectilinear structure resulted in the largest contact angle, with the diamond resulting in the smallest (**Table 2**). Optical profilometry (**Figure 8**) showed the average roughness to be 2.0 ± 0.8 μm (range: 1.4 – 2.9 μm) for rectilinear, 1.0 ± 0.3 μm (range: 0.9 – 1.4 μm) for gyroid, 1.3 ± 0.1 μm (range: 1.2 – 1.4 μm) for diamond, and 0.8 ± 0.1 μm (range: 0.7 – 0.9 μm) for solid (**Table 2**). The average maximum peek-to-valley height was 22.6 ± 10.4 μm (range: 16.0 – 34.6 μm) for rectilinear, 16.2 ± 12.6 μm (range: 7.5 – 30.6 μm) for gyroid, 17.5 ± 7.4 μm (range: 13.0

– 26.0 μm) for diamond, and 7.1 ± 0.6 μm (range: 6.4 – 7.5 μm) for solid. No significant difference was found between the average roughness for the four geometries.

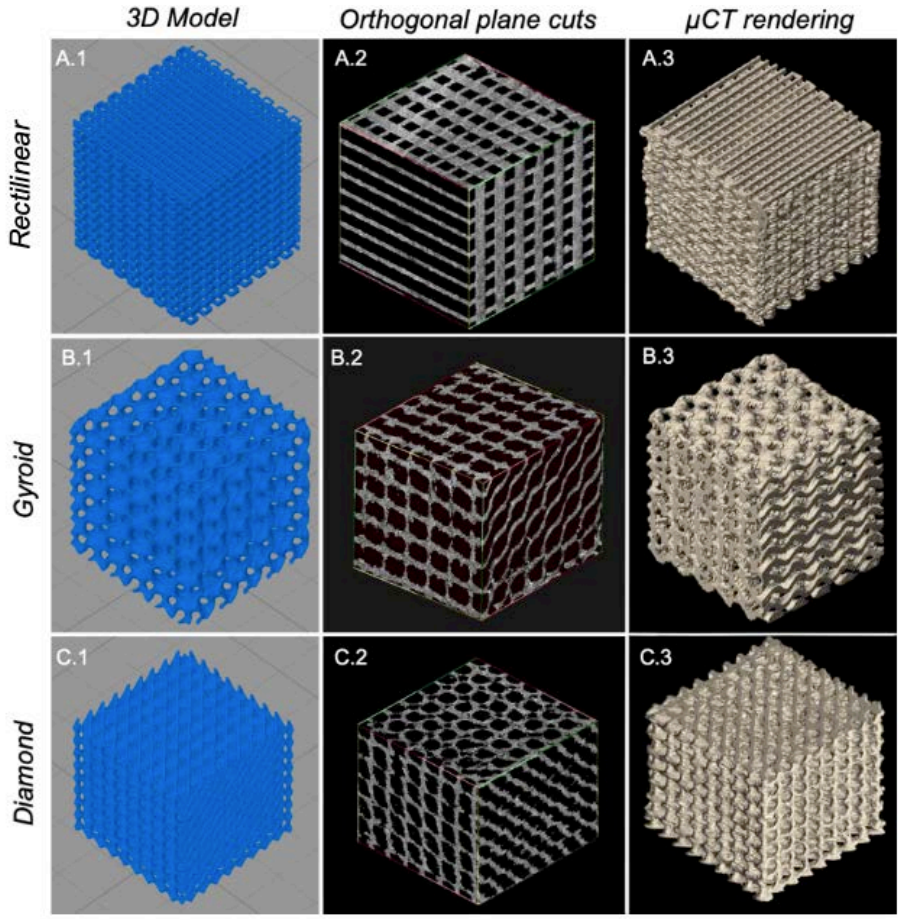

Figure 7. (First column) 3D design models of porous surfaces and (second and third columns) 3D images generated via micro-CT. The second column displays orthogonal cuts of each face to show the inner interconnected pore structure. The (row 1) rectilinear, (row 2) gyroid, and (row 3) diamond constructs are shown

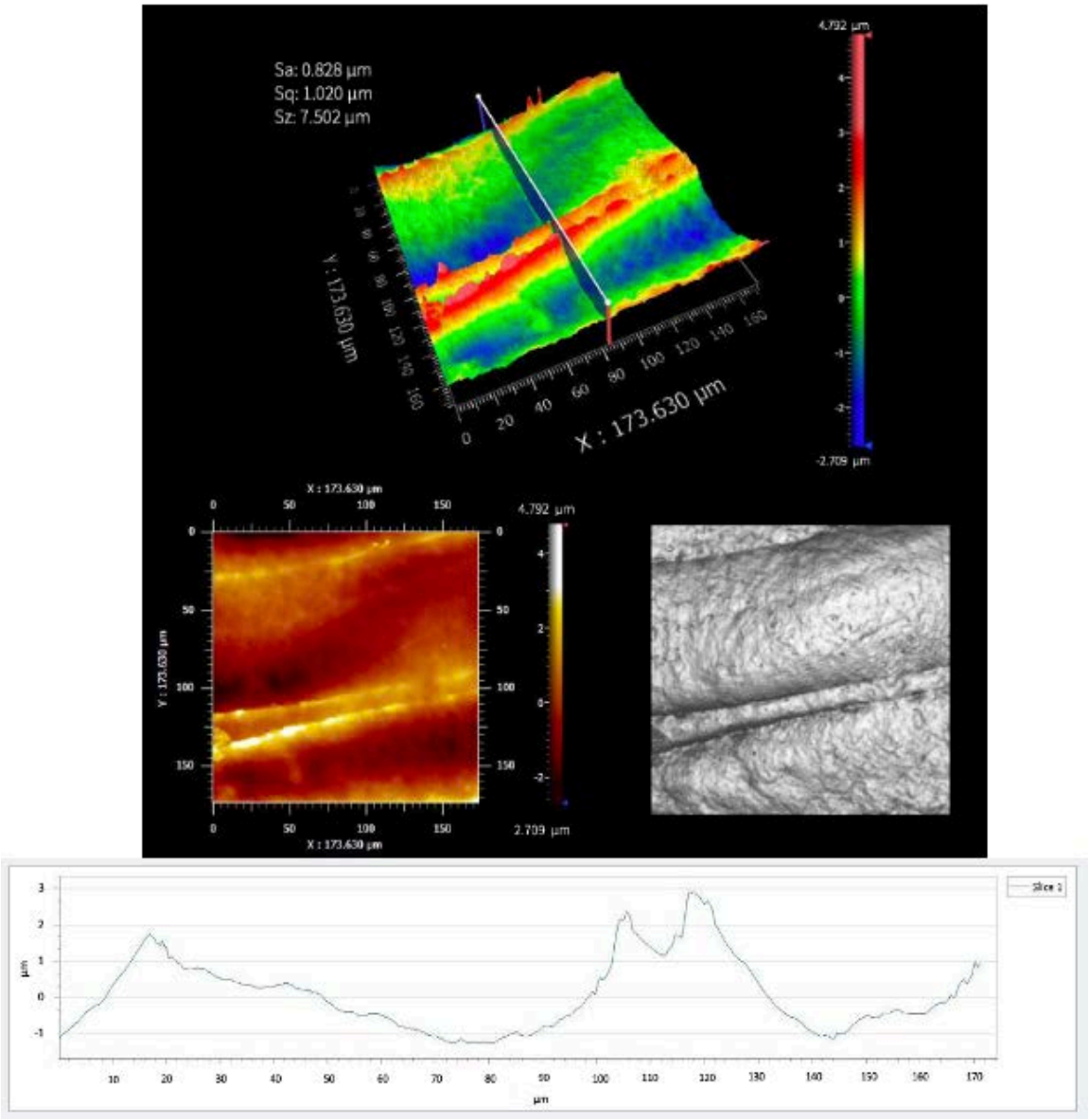

Figure 8. Example optical profilometry roughness measurement of a gyroid strut showing a measured roughness of 0.828 and peak-to-valley height of 7.502.

Table 2. Material characteristics for the porous PEEK constructs as determined by micro-CT imaging, sessile drop method, optical profilometry, and static compression testing. p-values correspond to comparison with as-designed values.

		Rectilinear	Gyroid	Diamond	Solid
Designed	**Pore size (μm)**	600	600	600	-
	Porosity (%)	70	74	72	-
Actual	**Pore size (μm)**	545 ± 43 ($p = 0.16$)	708 ± 64 ($p = 0.10$)	596 ± 94 ($p = 0.96$)	-
	Porosity (%)	70 ± 1.5 ($p = 0.67$)	68 ± 1.8 ($p = 0.06$)	69 ± 6.2 ($p = 0.47$)	-
	Contact Angle (°)	99.9 ± 7	64.2 ± 10	52.2 ± 5	69.2 ± 1.1
	Pore interconnectivity (%)	100	100	100	-
	Sa (μm)	2.0 ± 0.8	1.0 ± 0.3	1.3 ± 0.1	0.8 ± 0.1
	Sz (μm)	22.6 ± 10.4	16.2 ± 12.6	17.5 ± 7.4	7.1 ± 0.6
	Elastic Modulus (MPa)	238 ± 43.8	210 ± 39.1	268 ± 9.1	-
	Yield Strength (MPa)	6.6 ± 1.2	14.8 ± 0.7	17.1 ± 0.6	-

Mechanical testing

The main failure mode observed for each porous construct was successive layer collapse caused by the buckling of struts. For the TPMS constructs, the struts of consecutive layers tended to buckle in a similar direction, leading to a slight bulging effect. For the rectilinear, struts tended to break more sporadically throughout the structure with few instances of full layer collapse. The stress-strain curves exhibited behavior typical of porous materials, with a linear elastic region followed by a

plateau and a sharp, fluctuating increase in stress as the material becomes compressed and densified [1, 35, 36] (**Figure 9**). The fluctuations in stress following the linear region appeared to result from struts collapsing one at a time under the load. Very short toe regions were present prior to the linear elastic region in some samples, but these regions were excluded from modulus of elasticity calculations. The average yield strength was 6.6 ± 1.2 MPa (range: 5.6 – 8.5 MPa) for rectilinear, 14.8 ± 0.7 MPa (range: 14.1 – 15.5 MPa) for gyroid, and 17.1 ± 0.6 MPa (range: 16.3 – 17.9 MPa) for diamond. The average elastic modulus was for 238 ± 43.8 MPa (range: 179 – 281 MPa) for the rectilinear, 210 ± 39.1 MPa (range: 150 – 251 MPa) for gyroid, and 268 ± 9.1 MPa (range: 252 – 273 MPa) for diamond. Differences were seen between the yield strength of each geometry, with the diamond exhibiting significantly greater strength than the gyroid ($p < 0.05$) and rectilinear ($p < 0.05$) (**Figure 9, Table 2**). The gyroid structure was also found to have a greater yield strength than the rectilinear ($p < 0.05$). The mechanical property values can be found in **Table 2**.

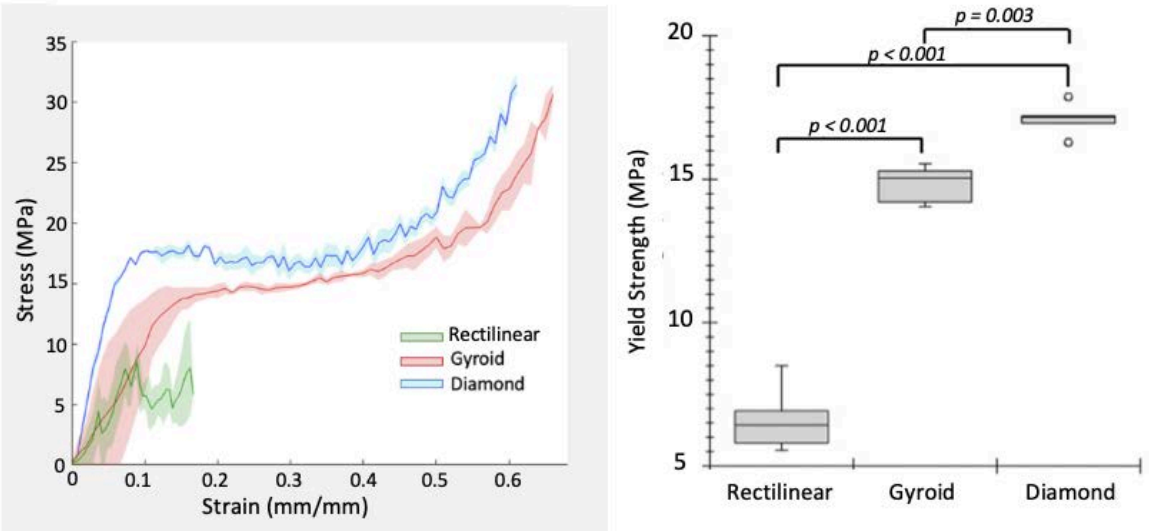

Figure 9. (Left) Stress-strain curves and (right) yield strength for porous PEEK constructs under compression loading, loaded perpendicular to layer deposition direction. Median values for yield strength for the rectilinear, gyroid, and diamond respectively are 6.4, 15.1, and 17.2 MPa.

In vitro biological assays

Using the MTT assay results, ALP activity was normalized to the cell number at each time point to determine the ALP activity per unit cell. Normalized ALP activity of the three porous PEEK samples at 7 days was found to be significantly greater than the solid sample ($p < 0.05$ for rectilinear, $p < 0.005$ for gyroid, $p < 0.001$ for diamond, **Figure 10**). At 14 days, the same relationships were observed but with greater significance ($p < 0.001$ for all three designs, **Figure 10**). No difference between the three porous constructs was found.

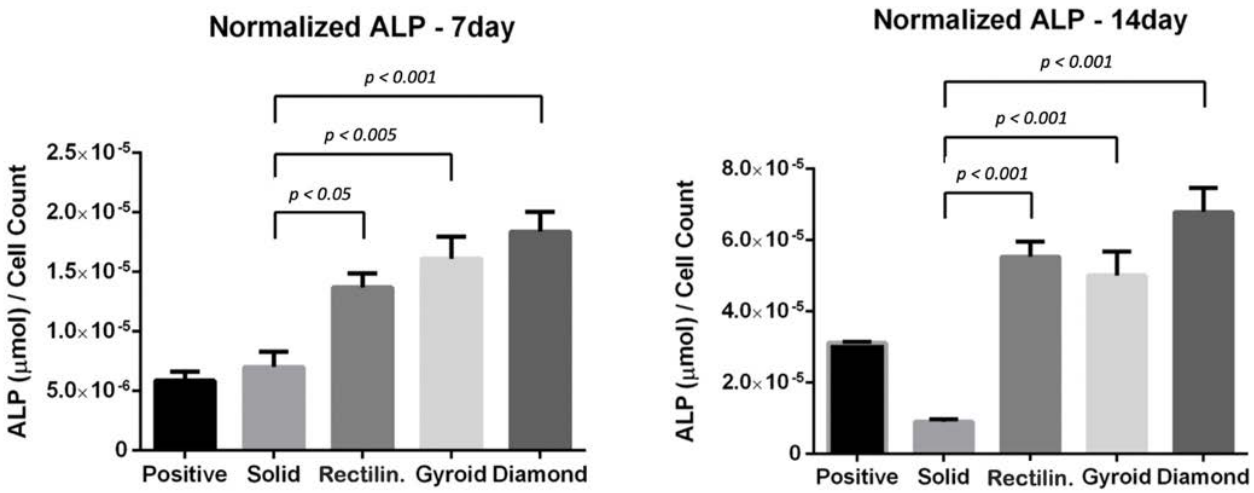

Figure 10. Normalized ALP assay results of cells cultured on porous PEEK constructs for (left) 7 days and (right) 14 days. n = 6 for each design and timepoint combination. The "Positive" bar represents no-PEEK positive control wells.

SEM Imaging

SEM images at 20 X magnification for flat and porous geometries with no cell seeding are included in **Figure 11**. SEM imaging of the 7-day samples revealed cells with flat, elongated morphology attached to the surface of the PEEK (**Figure 12a and 12b**). The cells were distributed sporadically on the both the solid and porous constructs with some instances of cell-to-cell interaction in the form of connecting cell extensions. There were also many instances of cells attaching to and/or bridging small pores and imperfections that resulted from the printing process (**Figure 12c and 12d**), particularly for the porous constructs. At 14 days, the cells appeared to have proliferated well and further spread on the PEEK with more apparent

filopodia and lamellipodia. More cell-to-cell interactions were observed, and in many instances a monolayer of cells could be observed covering the PEEK and obscuring the underlying surface (**Figure 12e and 12f**). While these morphologies were viewed for both solid and porous PEEK, relatively larger aggregates of cells were seen for the porous structures, commonly near the rough intersections of deposited filament, and cells were observed both on the outer surface and deeper into the pore network.

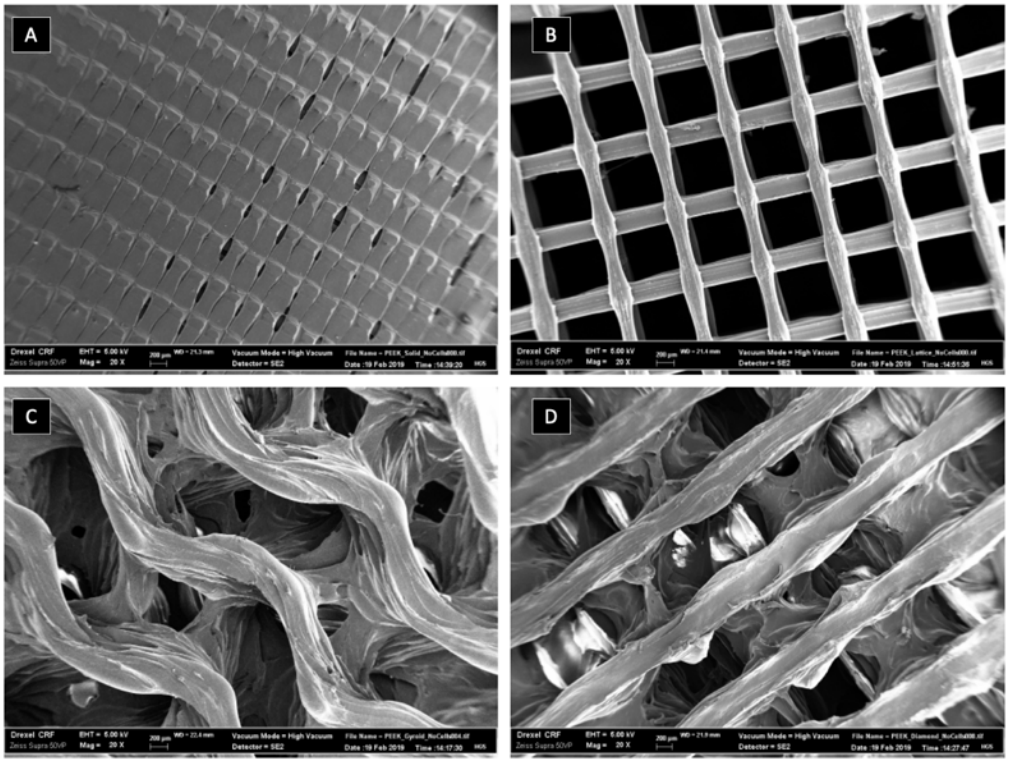

Figure 11. SEM images of example PEEK samples with no cell seeding at 20X magnification. Sample types are (A) flat, (B) rectilinear, (C) gyroid, and (D) diamond.

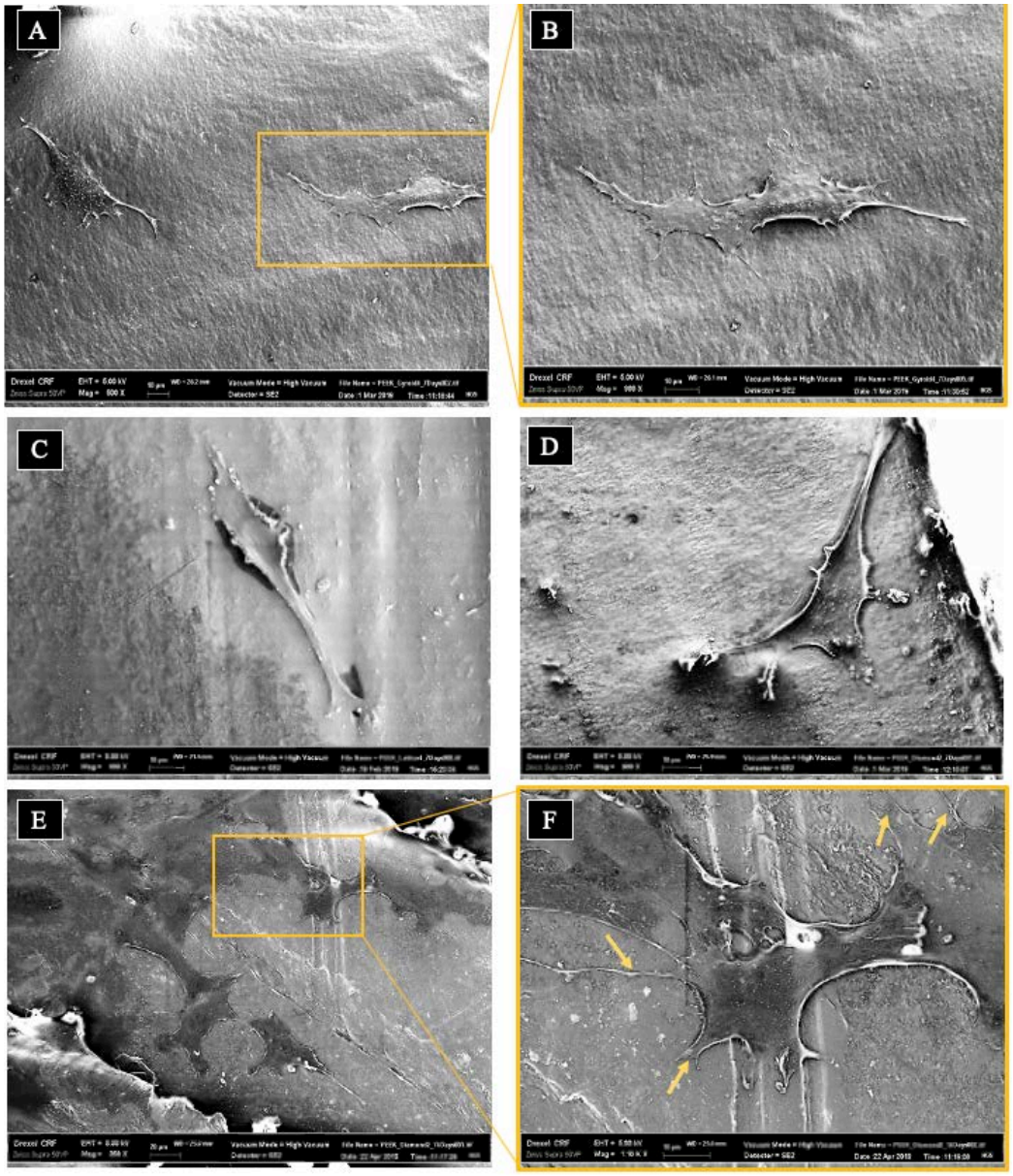

Figure 12. SEM images of pre-osteoblast cells cultured on porous PEEK structures for (A-D) 7 days and (E and F) 14 days. (A and b) Cells appeared attached to the PEEK surface and displayed a flat, elongated morphology. (C) A cell bridges a material void created during the printing process. (D) A cell is attached to a roughened filament junction (top right corner) and

numerous rough printing imperfections. (E and F) At 14 days, the cells have proliferated and spread, and extending lamellipodia and filopodia are apparent (examples indicated by arrows).

2.5 Discussion

PEEK is an attractive biomaterial for implantable devices due to its unique material properties including high yield strength, low elastic modulus, and natural radiolucency. Given its bioinert nature and consequently limited interaction with bone, there is significant interest in improving the material osteoconductivity through controlling porosity. This has historically been achieved through coatings, surface modifications, or laser sintering, though these methods have come with considerable disadvantages [12, 23]. In this study, the creation of porous PEEK using fused filament fabrication, an accessible and low-cost 3D printing method, was explored. The manufacturing of porous PEEK constructs based on triply periodic minimal surface design and with desirable pore morphology and mechanical properties was found to be possible. The porous PEEK was associated with increased preosteoblast activity compared to 3D printed solid controls, supporting the concept of 3D printed porous PEEK as an osteogenic biomaterial.

This study had a number of limitations. First, the investigation of porous PEEK characteristics was restricted to a single pore size and porosity for each geometry, limiting the ability to draw conclusions from the mechanical and biological testing. In terms of mechanical performance, it is well-known that porosity plays a large

role in determining the strength of cellular solids, with strength generally decreasing as porosity increases [35]. With regard to biological testing, pore size has been shown to affect cell response, and a gradient of sizes is suggested for bone ingrowth [37, 38]. However, because varying pore size or porosity would change other factors such as strut size or pore density, standardize the pore size was standardized across the structures, using a size that has been associated with positive bone cell and tissue response [28, 29, 39]. While the importance of future work to establish both phenomenologically and mechanistically how variable structure parameters (i.e. pore size, porosity) affect material functions is recognized, the aim of showing that porous PEEK can be successfully created via FFF to encompass desirable mechanical and biologic responses was achieved. Secondly, the mechanical strength of the porous PEEK was determined only under static loading conditions based on a testing standard and does not reflect complex physiological loads that may be encountered *in vivo*. Varying loading parameters or soaking the PEEK to simulate more realistic conditions will help improve the understanding of the porous PEEK mechanical properties in the future. Finally, given that this is an *in vitro* study, these findings represent the cell viability, proliferation, and ALP response to porous PEEK in a highly simplified environment. Further work is needed to explore the mechanisms behind the improved cell response to porous PEEK, as well as the histological response *in vivo*. Nevertheless, MC3T3-E1 preosteoblast cell testing has a history of use for

evaluating osteogenic biomaterials [12, 40, 41], and the hypothesis of improved cell response for porous PEEK was supported.

In this study, extrusion-based, commercially available 3D printing was used to successfully manufacture porous PEEK scaffolds with pore sizes and porosities similar to trabecular bone. Mimicking the morphology of trabecular bone is an important concept behind many highly porous implant surfaces that have been validated both experimentally and clinically for bone ingrowth [12, 42, 43]. Though porosities greater than 50% are generally accepted to support bone ingrowth for biomaterials [42], the optimal pore size for bone ingrowth is highly debated. Pore sizes ranging from approximately 150 to 1200 μm have been reported to support osteogenic cell responses and bone tissue ingrowth [44-47], with a minimum size recommendation 300 μm often cited as to allow for vascularization [15, 28, 47, 48]. Recent studies with promising results for 3D printed orthopaedic biomaterials helped inform the target of 600 μm pores, which has shown to achieve both sufficient mechanical strength and positive biologic responses [27-29, 39]. However, since significant discrepancies have been reported between designed and actual pore sizes for powder and resin-based printed scaffolds [2, 45, 49], it was important to determine the dimensional accuracy of the porous structures made via FFF. Varying degrees of mismatch in the pore sizes was found, denoting both shrinkage and enlargement. This can be attributed to microvariations in strut thickness observed via micro-CT and SEM imaging, an expected result of the FFF printing

process. Nonetheless, the measured pores did not significantly differ from the as-designed sizes and are well-within the size range recommended for bone ingrowth. This highlights an important advantage of 3D printing compared to other methods for creating porous scaffolds (e.g. salt leaching, sulfonation), that is, the ability to control pore characteristics.

While the strength of FFF printed PEEK has thus far shown promising results for solid and highly-infilled structures [5, 24, 25], the mechanical properties of FFF printed porous PEEK remain largely unknown. The measured properties of the PEEK scaffolds are comparable to the compressive strength and elastic modulus of trabecular bone (strength: 2 - 17 MPa, modulus: 344 - 3230 MPa) [50], and significantly less than the strength of cortical bone (strength: 118 - 211 MPa, modulus 16 - 18 GPa) [51]. Given the range of trabecular bone porosity and its inverse relationship to bone strength [52, 53], it is important to consider our results as compared to bone of similar porosity. In this study, the porous structure porosities were approximately 70%, indicating a ratio of material volume fraction of approximately 30%. In one study examining the relationship between the microstructure and mechanical properties of human trabecular bone, bone samples with an average bone volume fraction (bone volume/total volume, BV/TV) around 30% were found to have a compressive yield strengths of roughly 5 - 15 MPa, with strength increasing with decreasing porosity [54]. In another study, human iliac crest bone was structurally and mechanically characterized to reveal compressive

yield strengths roughly 10 MPa or less for trabecular bone with BV/TV measuring approximately 30% [53]. In both studies, variations in BV/TV were found to strongly predict the variations in bone strength [53, 54]. Future studies will determine whether a similar relationship exists between the porosity and strength of 3D printed PEEK. In addition to trabecular bone, the measured properties were also comparable to those reported for porous PEEK created via alternative methods [13, 22, 23, 55].

As a part of the mechanical analysis, it was observed that the compressive yield strength for the diamond and gyroid TPMS constructs was increased compared to the rectilinear. This was expected, given existing reports of superior mechanical performance for TPMS structures compared to strut-based structures [32, 36, 56, 57]. In one such study, matching lattices were designed using both conventional strut-based and TPSM methods and created via selective laser sintering [56]. When compared via compression testing and theoretical analysis, the TPMS structures were found to have increased yield strength and more homogenous stress distributions compared to the strut-based. The improved energy absorption behavior of the TPMS structures was attributed in part to their smooth convergence of struts, which reduces stress concentrations typically seen in sharp strut-to-strut connections [56]. Similar findings were presented in another study comparing SLS-printed strut-based lattices with multiple TPMS geometries [36]. The authors report superior compressive mechanical properties for the multiple TPMS structures in

general and recognize the diamond TPMS as having the most desirable properties. Again, these results indicated improved energy absorption for TPMS structures, as well as stretching-dominated deformation behavior as opposed to the more bending-dominated behavior of strut-based structures [36]. While a large body of research exists supporting the use of 3D printed TPMS structures for bone ingrowth due to their mechanical and osteoconductive properties [2, 49], the current report represents, to the authors' knowledge, the first examination of TPMS structures made from PEEK.

In addition to determining mechanical properties, the physical structures of biomaterials largely influence the biologic response at the bone-material interface [58], the foundation of implant fixation. In this study, the response of preosteoblast cells to FFF printed porous PEEK was therefore examined. Promising results were obtained, with porous PEEK resulting in increased ALP activity, an early marker for osteogenic differentiation, compared to non-porous controls. Using SEM, extended filopodia and lamellipodia were observed indicating communication between cells, surface adhesion, and cell monolayer formation, further indicating an overall positive biologic response [43, 44]. In general, the cell testing results were expected, as the addition of porosity has been shown to improve the osteogenic ability of different biomaterials. For orthopaedic materials, including PEEK, osteoconductivity has been increased by introducing porosity both chemically and, more recently, mechanically through laser-based printing [13, 19, 21, 43, 45, 59, 60].

However, because these studies often involve PEEK composite materials and/or chemically induced porosity, very few reports exist for virgin PEEK with tunable pore structures. In one such study, the osteogenic potential of macroporous PEEK, created via injection of PEEK into a 3D printed mold, was examined [60]. It was found that, similar to the current study, the inclusion of porosity increased the biologic response to PEEK *in vitro*. Additionally, in an *in vivo* rabbit model, the macroporous structure allowed for vascularization and soft tissue ingrowth, while solid PEEK led to fibrous capsule growth. The authors conclude that a combination of micro- and macropores, for supporting both early-stage cell attachment and strong tissue attachment, may greatly contribute to the long-term success of PEEK implants [60]. Similar results were reported by in a recent study comparing the osseointegration potential of smooth, macroporous and titanium-coated PEEK [19]. In this case, a macropore surface layer was created via salt leaching. The authors reported that the porous PEEK construct was associated with increased preosteoblast cell differentiation compared to the smooth and titanium-coated PEEK. In a rat tibia model, the macroporous PEEK also led to greater functional osseointegration as determined by pullout testing [19]. Surface roughness was considered alongside macropore structure, given the widespread use of roughness to induce osteoconductivity [12, 61]. The authors found that the macropore structure was more influential to cell response than micro-roughness, and they speculate that this is due in part to the ability of pore curvature to promote

osteogenic cellular cues similar to native bone [19]. In the present study, surface roughness was also assessed, and no significant difference was found between the solid and porous structures. While the greater peak-to-valley heights for porous structures (seemingly due to the irregular microtopology of filament/strut intersections created during the printing process) may have provided anchorage points for cell attachment as seen under SEM, the inclusion of porosity appeared to be the more important factor affecting cell response between solid and porous PEEK. Other studies considering both porosity and roughness have reported similar results [20, 62], with improved cell response at least partially attributed to increased surface area and altered mechanical cell stimulation related to the porous curvature [58]. For TMPS structures in particular, further work is essential for understanding the mechanisms behind how their curvature, known to be similar to trabecular bone [1, 58], may improve cell response.

In recent years, clinical interest has grown for both the use of PEEK in orthopaedic components and the application of 3D printing for creating complex porous structures. In this study, the feasibility of using FFF to create 3D printed porous PEEK with a tuned pore structure and desirable mechanical properties was demonstrated. Structures designed with TPMS topologies displayed improved mechanical strength compared to a traditional rectilinear structure. Additionally, in an *in vitro* cell viability test, it was found that 3D printed porous PEEK led to increased preosteoblast activity compared to 3D printed solid controls. While these

findings are promising, future studies exploring the effect of variable porosity on mechanical properties as well as the histological response to TPMS structures are essential for further assessing 3D printed porous PEEK as an orthopaedic biomaterial.

2.6 References

1. Bobbert, F.S.L., et al., Additively manufactured metallic porous biomaterials based on minimal surfaces: A unique combination of topological, mechanical, and mass transport properties. Acta Biomater, 2017. **53**: p. 572-584.

2. Yang, Y., et al., Additive manufacturing of bone scaffolds. International Journal of Bioprinting, 2019. **5**(1).

3. Lin, K., et al., 3D Printing of Bioceramic Scaffolds-Barriers to the Clinical Translation: From Promise to Reality, and Future Perspectives. Materials (Basel), 2019. **12**(17).

4. Panayotov, I.V., et al., Polyetheretherketone (PEEK) for medical applications. J Mater Sci Mater Med, 2016. **27**(7): p. 118.

5. Honigmann, P., et al., Patient-Specific Surgical Implants Made of 3D Printed PEEK: Material, Technology, and Scope of Surgical Application. Biomed Res Int, 2018. **2018**: p. 4520636.

6. Kurtz, S.M., Applications of polyaryletheretherketone in spinal implants: fusion and motion preservation, in PEEK Biomaterials Handbook. 2012, Elsevier. p. 201-220.

7. Du, Z., et al., Feasibility and Safety of a Cemented PEEK-on-PE Knee Replacement in a Goat Model: A Preliminary Study. Artificial organs, 2018. **42**(8): p. E204-E214.

8. de Ruiter, L., et al., A preclinical numerical assessment of a polyetheretherketone femoral component in total knee arthroplasty during gait. Journal of experimental orthopaedics, 2017. **4**(1): p. 3.

9. Cowie, R.M., et al., PEEK-OPTIMA™ as an alternative to cobalt chrome in the femoral component of total knee replacement: a preliminary study. Proceedings of the Institution of Mechanical Engineers, Part H: Journal of Engineering in Medicine, 2016. **230**(11): p. 1008-1015.

10. Newman, J.M., et al., Cementless Total Knee Arthroplasty: A Comprehensive Review of the Literature. Orthopedics, 2018. **41**(5): p. 263-273.

11. Kurtz, S.M. and J.N. Devine, PEEK biomaterials in trauma, orthopedic, and spinal implants. Biomaterials, 2007. **28**(32): p. 4845-69.

12. Torstrick, F.B., et al., Getting PEEK to Stick to Bone: The Development of Porous PEEK for Interbody Fusion Devices. Techniques in orthopaedics (Rockville, Md.), 2017. **32**(3): p. 158-166.

13. Landy, B.C., et al., Mechanical and in vitro investigation of a porous PEEK foam for medical device implants. J Appl Biomater Funct Mater, 2013. **11**(1): p. e35-44.

14. Wang, S., et al., Enhanced antibacterial property and osteo-differentiation activity on plasma treated porous polyetheretherketone with hierarchical micro/nano-topography. Journal of Biomaterials science, Polymer edition, 2018. **29**(5): p. 520-542.

15. Karageorgiou, V. and D. Kaplan, Porosity of 3D biomaterial scaffolds and osteogenesis. Biomaterials, 2005. **26**(27): p. 5474-5491.

16. Bakar, M.A., et al., Tensile properties, tension–tension fatigue and biological response of polyetheretherketone–hydroxyapatite composites for load-bearing orthopedic implants. Biomaterials, 2003. **24**(13): p. 2245-2250.

17. Mahjoubi, H., et al., Surface phosphonation enhances hydroxyapatite coating adhesion on polyetheretherketone and its osseointegration potential. Acta Biomater, 2017. **47**: p. 149-158.

18. Harting, R., et al., Functionalization of polyethetherketone for application in dentistry and orthopedics, in BioNanoMaterials. 2017.

19. Torstrick, F.B., et al., Porous PEEK improves the bone-implant interface compared to plasma-sprayed titanium coating on PEEK. Biomaterials, 2018. **185**: p. 106-116.

20. Han, X., et al., An In Vitro Study of Osteoblast Response on Fused-Filament Fabrication 3D Printed PEEK for Dental and Cranio-Maxillofacial Implants. J Clin Med, 2019. **8**(6).

21. Hieda, A., et al., In vivo bioactivity of porous polyetheretherketone with a foamed surface. Dent Mater J, 2017. **36**(2): p. 222-229.

22. Evans, N.T., et al., Local deformation behavior of surface porous polyether-ether-ketone. J Mech Behav Biomed Mater, 2017. **65**: p. 522-532.

23. Siddiq, A.R. and A.R. Kennedy, Porous poly-ether ether ketone (PEEK) manufactured by a novel powder route using near-spherical salt bead porogens:

characterisation and mechanical properties. Mater Sci Eng C Mater Biol Appl, 2015. **47**: p. 180-8.

24. Vaezi, M. and S. Yang, Extrusion-based additive manufacturing of PEEK for biomedical applications. Virtual and Physical Prototyping, 2015. **10**(3): p. 123-135.

25. Basgul, C., et al., Structure–property relationships for 3D-printed PEEK intervertebral lumbar cages produced using fused filament fabrication. Journal of materials research, 2018. **33**(14): p. 2040-2051.

26. Barba, D., E. Alabort, and R. Reed, Synthetic bone: Design by additive manufacturing. Acta Biomaterialia, 2019. **97**: p. 637-656.

27. Cavo, M. and S. Scaglione, *Scaffold microstructure effects on functional and mechanical performance: Integration of theoretical and experimental approaches for bone tissue engineering applications.* Mater Sci Eng C Mater Biol Appl, 2016. **68**: p. 872-879.

28. Taniguchi, N., et al., *Effect of pore size on bone ingrowth into porous titanium implants fabricated by additive manufacturing: an in vivo experiment.* Materials Science and Engineering: C, 2016. **59**: p. 690-701.

29. Frosch, K.H., et al., *Growth behavior, matrix production, and gene expression of human osteoblasts in defined cylindrical titanium channels.* J Biomed Mater Res A, 2004. **68**(2): p. 325-34.

30. International., A., *D695-15 Standard Test Method for Compressive Properties of Rigid Plastics*. 2015, ASTM International: West Conshohocken, PA.

31. *ISO/IEC 17025:2005. General requirements for the competence of testing and calibration laboratories International Organization for Standardization*. 2017: Geneva, Switzerland.

32. Maskery, I., et al., *Compressive failure modes and energy absorption in additively manufactured double gyroid lattices.* Additive Manufacturing, 2017. **16**: p. 24-29.

33. Niks, M. and M. Otto, *Towards an optimized MTT assay.* (0022-1759 (Print)).

34. Frohbergh, M.E., et al., *Electrospun hydroxyapatite-containing chitosan nanofibers crosslinked with genipin for bone tissue engineering.* Biomaterials, 2012. **33**(36): p. 9167-78.

35. Gibson, L.J. and M.F. Ashby, *Cellular solids: structure and properties*. 1999: Cambridge university press.

36. Al-Ketan, O., R. Rowshan, and R.K.A. Al-Rub, *Topology-mechanical property relationship of 3D printed strut, skeletal, and sheet based periodic metallic cellular materials.* Additive Manufacturing, 2018. **19**: p. 167-183.

37. Liu, F., et al., *Functionally graded porous scaffolds in multiple patterns: New design method, physical and mechanical properties.* Materials & Design, 2018. **160**: p. 849-860.

38. Vijayavenkataraman, S., L.Y. Kuan, and W.F. Lu, *3D-printed ceramic triply periodic minimal surface structures for design of functionally graded bone implants.* Materials & Design, 2020: p. 108602.

39. Li, P., et al., *A novel 3D printed cage with microporous structure and in vivo fusion function.* J Biomed Mater Res A, 2019. **107**(7): p. 1386-1392.

40. Bhattarai, S.R., et al., *Novel production method and in-vitro cell compatibility of porous Ti-6Al-4V alloy disk for hard tissue engineering.* J Biomed Mater Res A, 2008. **86**(2): p. 289-99.

41. Kim, H.-L., et al., *Preparation and characterization of nano-sized hydroxyapatite/alginate/chitosan composite scaffolds for bone tissue engineering.* Materials Science and Engineering: C, 2015. **54**: p. 20-25.

42. Li, Y., et al., *New Developments of Ti-Based Alloys for Biomedical Applications.* Materials (Basel, Switzerland), 2014. **7**(3): p. 1709-1800.

43. Fernandez-Yague, M.A., et al., *Biomimetic approaches in bone tissue engineering: Integrating biological and physicomechanical strategies.* Advanced drug delivery reviews, 2015. **84**: p. 1-29.

44. Zhao, D., et al., *Effect of pore geometry on the fatigue properties and cell affinity of porous titanium scaffolds fabricated by selective laser melting.* Journal of the mechanical behavior of biomedical materials, 2018. **88**: p. 478-487.

45. Van Bael, S., et al., *The effect of pore geometry on the in vitro biological behavior of human periosteum-derived cells seeded on selective laser-melted Ti6Al4V bone scaffolds.* Acta biomaterialia, 2012. **8**(7): p. 2824-2834.

46. Liu, Y., et al., *The physicochemical/biological properties of porous tantalum and the potential surface modification techniques to improve its clinical application in dental implantology.* Materials Science and Engineering: C, 2015. **49**: p. 323-329.

47. Feng, B., et al., *The effect of pore size on tissue ingrowth and neovascularization in porous bioceramics of controlled architecture in vivo.* Biomed Mater, 2011. **6**(1): p. 015007.

48. Lv, J., et al., *Enhanced angiogenesis and osteogenesis in critical bone defects by the controlled release of BMP-2 and VEGF: implantation of electron beam melting-fabricated porous Ti6Al4V scaffolds incorporating growth factor-doped fibrin glue.* Biomed Mater, 2015. **10**(3): p. 035013.

49. Melchels, F.P., et al., *Mathematically defined tissue engineering scaffold architectures prepared by stereolithography.* Biomaterials, 2010. **31**(27): p. 6909-16.

50. Morgan, E.F. and T.M. Keaveny, *Dependence of yield strain of human trabecular bone on anatomic site.* J Biomech, 2001. **34**(5): p. 569-77.

51. Reilly, D.T. and A.H. Burstein, *The elastic and ultimate properties of compact bone tissue.* J Biomech, 1975. **8**(6): p. 393-405.

52. Syahrom, A., et al., *Mechanical and microarchitectural analyses of cancellous bone through experiment and computer simulation.* Med Biol Eng Comput, 2011. **49**(12): p. 1393-403.

53. Thomsen, J.S., E.N. Ebbesen, and L. Mosekilde, *Relationships between static histomorphometry and bone strength measurements in human iliac crest bone biopsies.* Bone, 1998. **22**(2): p. 153-63.

54. Nazarian, A., et al., *Bone volume fraction explains the variation in strength and stiffness of cancellous bone affected by metastatic cancer and osteoporosis.* Calcif Tissue Int, 2008. **83**(6): p. 368-79.

55. Senatov, F., et al., *Comparative analysis of structure and mechanical properties of porous PEEK and UHMWPE biomimetic scaffolds.* Materials Letters, 2019. **239**: p. 63-66.

56. Zhao, M., et al., *Improved mechanical properties and energy absorption of BCC lattice structures with triply periodic minimal surfaces fabricated by SLM.* Materials, 2018. **11**(12): p. 2411.

57. Liu, F., et al., *Mechanical properties of optimized diamond lattice structure for bone scaffolds fabricated via selective laser melting.* Materials, 2018. **11**(3): p. 374.

58. Zadpoor, A.A., *Bone tissue regeneration: the role of scaffold geometry.* Biomater Sci, 2015. **3**(2): p. 231-45.

59. Roskies, M., et al., *Improving PEEK bioactivity for craniofacial reconstruction using a 3D printed scaffold embedded with mesenchymal stem cells.* J Biomater Appl, 2016. **31**(1): p. 132-9.

60. Feng, X., et al., *Three-Dimensionally-Printed Polyether-Ether-Ketone Implant with a Cross-Linked Structure and Acid-Etched Microporous Surface Promotes Integration with Soft Tissue.* Int J Mol Sci, 2019. **20**(15).

61. Ting, M., et al., *Classification and Effects of Implant Surface Modification on the Bone: Human Cell-Based In Vitro Studies.* J Oral Implantol, 2017. **43**(1): p. 58-83.

62. Cheng, A., et al., *Additively manufactured 3D porous Ti-6Al-4V constructs mimic trabecular bone structure and regulate osteoblast proliferation, differentiation and local factor production in a porosity and surface roughness dependent manner.* Biofabrication, 2014. **6**(4): p. 045007.

Chapter 3: Material Properties of 3D Printed Solid (Nonporous) PEEK

3.1 Abstract

Fused filament fabrication (FFF) of polyetheretherketone (PEEK) has been gaining attention for its potential use in creating orthopaedic implants at or near the point of care. Understanding the mechanical properties and degree of anisotropy imparted on PEEK by the FFF process is vital for designing and predicting the behavior of structures created using this technique. In this study, the mechanical behavior of solid (nonporous) FFF PEEK is described. Solid PEEK prisms with the dimensions 12.7 x 12.7 x 25.4 mm were designed and additively manufactured with the same printing parameters used for creating porous PEEK. Cyclic compression testing and testing until failure were then performed on the prisms, with loading oriented either parallel or perpendicular to the material layer deposition direction. Using the resulting force and displacement data, mechanical properties including Young's modulus, yield strength, and Poisson's ratio were calculated for each print orientation. Loading perpendicular to the layer direction resulted in an elastic modulus of 2.34 ± 0.22 GPa and yield strength of 58.0 ± 1.2 MPa, while parallel loading resulted in a modulus of 2.20 ± 0.46 GPa and yield strength of 68.0 ± 8.1 MPa. The degree of elastic modulus anisotropy was relatively low, with a difference of 6.2% between the values in each orientation and no statistical difference found.

The difference in yield strength between orientations was 14.8%, with the xy-direction having significantly greater yield strength. Using scanning electron microscopy, it was observed that the failed specimens exhibited layer splitting which occurred cleanly along the interface between layers. The results of this study will establish the constitutive material properties to be used in the architecture-property model validation in the coming chapters.

3.2 Introduction

As additive manufacturing processes and materials continue to advance, the ability to 3D print implantable medical devices at the point of care is gaining significant interest. Much of that interest is focused on fused filament fabrication, given its suitability for use in a hospital setting [1]. While FFF with low temperature polymers is currently utilized by clinicians to create tools such as surgical guides and teaching aids [1-3], recent advancements in the process have allowed for the printing of high temperature implantable polymers like PEEK [4]. PEEK has a history of use in medical devices such as spinal cages, dental implants, and maxillofacial and cranial implants [5], though these devices have thus far relied on traditional manufacturing methods. However, the ability to 3D print PEEK with mechanical properties similar to injection molded PEEK has opened the door to more 3D printed medical devices [6-8], making it essential to better understand the characteristics imparted on the material by the manufacturing process.

Fused filament fabrication is a process in which material is melted and deposited layer-by-layer to create an object from the bottom-up. Unlike injection molding in which melted material quickly cures as a single part within a predesigned mold, FFF works by melting only one filament strand at a time. As a line of filament is deposited, it forms a bond with the material next to and below it. Bonding in the z-direction (between layers) tends to be weaker than bonding in the x and y directions (within layers) due to gaps in the layer interfaces, uncontrolled cooling and curing, and residual stresses resulting from repeated thermal expansion and contraction [9-13]. Properties in the x and y-directions are influenced more equivalently, thus the material tends to be transversely isotropic with an axis of symmetry in the z axis and a plane of isotropy in the x-y plane (**Figure 13**).

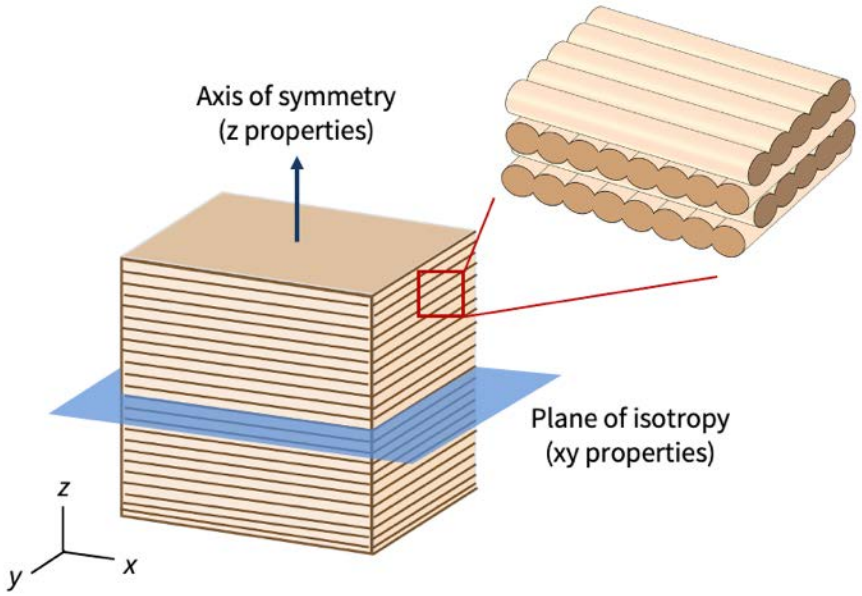

Figure 13. Schematic showing the material layer deposition direction and fusion leading to anisotropic properties for FFF structures.

FFF-induced anisotropy has been well-studied for low temperature materials like polylactic acid (PLA) and acrylonitrile butadiene styrene (ABS) [9, 12-14], with a study by Coogan et al. directly investigating the factors affecting interlayer bonding by printing ABS samples with a single fiber thickness [15]. The researchers highlighted the factors most important to determining bond strength as layer height, followed by layer width, nozzle temperature, and print speed, which affect wetting, diffusion, and intimate contact between deposits [15]. Similar investigations for PEEK are comparatively limited. In a study from Arif et al., PEEK specimens were printed both horizontally (at 0° and 90° orientations) and vertically, then tested in tension and flexion [10]. The results showed greater tensile strength,

Young's modulus, flexural strength, and flexural modulus for samples loaded parallel to the filament deposit direction and significantly lower property values for samples loaded perpendicularly. In another study, Basgul et al. focused on interlayer adhesion for FFF PEEK and showed improved bonding for samples having less cooling time, which was attributed to thermal conditions allowing for improved healing between layers [16]. The spinal cages created in this study were compression tested parallel to the layer deposition direction to simulate a worst-case loading scenario, however no comparison to strength perpendicular to the deposition direction was made.

Direction-dependent material properties in 3D printed porous materials can result both from the structure architecture and the printing method itself. While descriptions of anisotropy have been reported for a number of materials and printing processes, little is known about the directional properties of FFF PEEK, the material comprising the porous structures throughout this work. The aim of this study is to characterize the mechanical properties of solid AM PEEK and to understand the anisotropy resulting from the layer-by-layer material deposition process of fused filament fabrication. It is hypothesized that the mechanical properties of the printed PEEK will be transversely isotropic. Results from this study will inform the model validation for porous PEEK the coming chapters.

3.3 Methods

3D Printing of PEEK samples

Solid constructs were additively manufactured via FFF using VESTAKEEP i4 PEEK filament (Evonik Industries AG, Essen, Germany), which was dried in an oven prior to printing. All samples were manufactured with a high temperature polymer FFF 3D printer (HTRD 1.3, Kumovis, Munich, Germany) and were designed as prisms with dimensions 12.7 x 12.7 x 25.4 mm according to ASTM D695 [17]. Half of the samples (n = 5) were printed vertically and half (n = 5) horizontally to allow for testing multiple print orientations in compression. Because printing parameters including speed and temperature impact the resulting mechanical properties of printed PEEK [16, 18, 19], it is important that the printing parameters used to create representative constituent material (solid PEEK) match those used to ultimately create the porous structures. Since porous PEEK is significantly more sensitive to parameter choice than nonporous, the choice of printing parameters was based on their ability to successfully produce a range of porous structures (**Table 3**). To determine these values, iterative testing was performed using the porous architectures introduced in **Chapter 5**. As a part of this testing, the main parameters controlling structure quality were systematically varied, and the structures were visually assessed for consistent pore size and shape, uniform material color and texture, and openness and interconnectedness of pores (determined by backlighting the structures). Pin gauges were also used to help assess the size and openness of the pores.

Table 3. Printing parameters used in the manufacturing of solid PEEK samples.

Nozzle Size	Layer Height	Nozzle Temperature	Bed Temperature	Chamber Temperature	Printing Speed	Raster Angle
0.2 mm	0.12 mm	415° C	240° C	150° C	2200 mm/min	0°, 90°

Mechanical Testing

The 3D printed PEEK samples underwent cyclic loading in compression to determine the elastic properties and were then compressed until failure. All tests were conducted in accordance with ISO 17025 quality system requirements [20]. For each test, the prisms were oriented standing upright so that samples printed vertically were loaded perpendicular to the layer deposition direction (z-direction) and samples printed horizontally were loaded parallel to layer deposition (xy-direction). Cyclic testing was performed using an MTS 858 Mini Bionix (MTS Systems, Eden Prairie, MN), with calibrated axial and lateral extensometers attached to each sample to measure displacement in two directions (**Figure 14**). The loading cycled between 50 and 750 N ten times for each sample. The upper limit was chosen to ensure loading remained in the linear-elastic region of the material behavior. Following cyclic testing, the samples then underwent compression to failure using an MTS Criterion Model 43 with calibrated load and displacement

sensors and lubricated platens at a displacement rate of 1.3 mm/min per ASTM D695 [21].

Stress-strain curves were generated from the data, and the elastic modulus, Poisson's ratio, and yield strength for each porous structure were determined using a custom script in MATLAB 2021a (MathWorks, Natick, MA) with recommendations from ASTM D695-15 [21] as a guide. Using the cyclic loading data, Young's modulus was calculated as the slope of the linear region for each cycle, and the values from all 10 cycles were averaged. The data from the extensometers was used to calculated Poisson's ratio according to the methods below (**Equation 3.7**), with the final value being an average of the 10 cycles for each sample. The yield strength was taken as the 0.2% offset stress from the stress-strain curves generated from the compression to failure testing data.

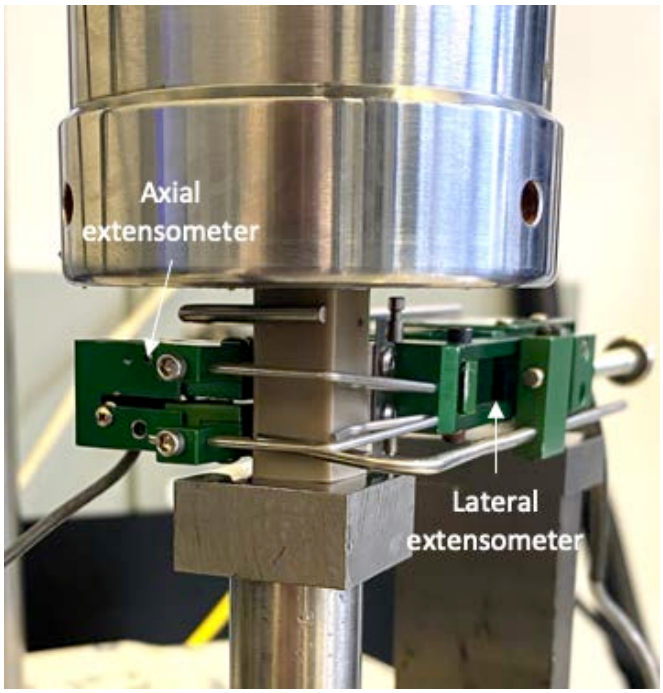

Figure 14. Testing setup for solid PEEK cyclic loading.

Fracture Analysis

Following mechanical testing, the structures were imaged via scanning electron microscopy (SEM) using a Zeiss Supra 50VP SEM (Zeiss, Oberkochen, Germany) in order to help elucidate the fracture behavior. The samples were sputter coated with platinum-palladium alloy prior to imaging and micrographs were collected with a secondary electron detector at an accelerating voltage of 20 kV.

Determination of Elastic Constants

The stress and strain of a material can be written as second rank tensors, each having nine components. In the case of stress, this includes three axial stresses (σ_{xx}, σ_{yy}, σ_{zz}) and six shear (σ_{xy}, σ_{yx}, $\sigma_{xz}, \sigma_{zx}, \sigma_{yz}, \sigma_{zy}$). According to Hooke's Law, the stress in a linear elastic material can be related to the strain components using a fourth order stiffness tensor of material properties. Using integers 1, 2, 3 to represent the x, y, z directions, this relationship can be written as

$$\sigma_{ij} = C_{ijkl}\varepsilon_{kl} \tag{3.1}$$

with $i, j, k, l = 1, 2, 3$. In Equation 3.1, σ_{kl} represents stress, ε_{ij} is strain, and C_{ijkl} represents the stiffness tensor (also referred to as the stiffness or elasticity matrix, which is the inverse of the compliance matrix). For a 3-dimensional problem, C_{ijkl} has 81 independent components. Taking into consideration the symmetry of stress and strain ($\sigma_{ij} = \sigma_{ji}$ and $\varepsilon_{ij} = \varepsilon_{ji}$), the number of stress components reduces to six and the number of stiffness matrix components to 36 (with symmetry further reducing this number to 21). Thus, the stiffness matrix can be written as

$$C = \begin{bmatrix} C_{1111} & C_{1122} & C_{1133} & C_{1123} & C_{1113} & C_{1112} \\ & C_{2222} & C_{2233} & C_{2223} & C_{2213} & C_{2212} \\ & & C_{3333} & C_{3323} & C_{3313} & C_{3312} \\ & symmetric & & C_{2323} & C_{2313} & C_{2312} \\ & & & & C_{1313} & C_{1312} \\ & & & & & C_{1212} \end{bmatrix}. \tag{3.2}$$

For anisotropic materials, the 21 stiffness matrix components are all unique. However, further material property symmetries may arise due to the structure of the material. For orthotropic materials having three orthogonal planes of symmetry, the number of unique elastic constants reduces to 9. Using the compliance matrix and introducing the engineering constants for elasticity gives the equation for orthotropic materials as

$$\begin{bmatrix} \varepsilon_{11} \\ \varepsilon_{22} \\ \varepsilon_{33} \\ \gamma_{23} \\ \gamma_{13} \\ \gamma_{12} \end{bmatrix} = \begin{bmatrix} \frac{1}{E_1} & -\frac{v_{21}}{E_2} & -\frac{v_{31}}{E_3} & 0 & 0 & 0 \\ -\frac{v_{12}}{E_1} & \frac{1}{E_2} & -\frac{v_{32}}{E_3} & 0 & 0 & 0 \\ -\frac{v_{13}}{E_1} & -\frac{v_{23}}{E_2} & \frac{1}{E_3} & 0 & 0 & 0 \\ 0 & 0 & 0 & \frac{1}{G_{23}} & 0 & 0 \\ 0 & 0 & 0 & 0 & \frac{1}{G_{13}} & 0 \\ 0 & 0 & 0 & 0 & 0 & \frac{1}{G_{12}} \end{bmatrix} \begin{bmatrix} \sigma_{11} \\ \sigma_{22} \\ \sigma_{33} \\ \sigma_{23} \\ \sigma_{13} \\ \sigma_{12} \end{bmatrix} \tag{3.3}$$

where γ_{ij} denotes shear strain, E_i is the Young's modulus of the material, v_{ij} is Poisson's ratio, and G_{ij} is the shear modulus.

In this study, the FFF printed PEEK was assumed to be transversely isotropic with both orientations parallel to the layer printing direction (x and y directions) behaving similarly. For a material with x-y symmetry

$$E_1 = E_2, \qquad G_{13} = G_{23}, \qquad v_{31} = v_{32}, \qquad v_{13} = v_{23}, \qquad v_{12} = v_{21} \tag{3.4}$$

and because the shear modulus G_{12} is related to the x-y stiffness and Poisson's ratio by

$$G_{12} = \frac{E_1}{2(1 + v_{12})} \tag{3.5}$$

the number of constants needed to define the transversely isotropic material properties is reduced to 5. Designating the x and y directions as in-plane and z as transverse, the material property relationship can be written as

$$\begin{bmatrix} \varepsilon_{xx} \\ \varepsilon_{yy} \\ \varepsilon_{zz} \\ \gamma_{yz} \\ \gamma_{xz} \\ \gamma_{xy} \end{bmatrix} = \begin{bmatrix} \frac{1}{E} & -\frac{v}{E} & -\frac{v'}{E'} & 0 & 0 & 0 \\ -\frac{v}{E} & \frac{1}{E} & -\frac{v'}{E'} & 0 & 0 & 0 \\ -\frac{v'}{E'} & -\frac{v'}{E'} & \frac{1}{E'} & 0 & 0 & 0 \\ 0 & 0 & 0 & \frac{1}{G'} & 0 & 0 \\ 0 & 0 & 0 & 0 & \frac{1}{G'} & 0 \\ 0 & 0 & 0 & 0 & 0 & \frac{2(1+v)}{E} \end{bmatrix} \begin{bmatrix} \sigma_{xx} \\ \sigma_{yy} \\ \sigma_{zz} \\ \sigma_{yz} \\ \sigma_{xz} \\ \sigma_{xy} \end{bmatrix} \tag{3.6}$$

where transverse properties are denoted by the prime superscript (i.e., E', v', G'). In this study, compression testing both parallel and perpendicular to the layer printing direction were used to determine the E, E', E, and v', with G' determined using the Saint-Venant relation [22, 23] described below. Each elastic modulus can be determined from the linear portion of the stress-strain plots created following cyclic

compression in both testing orientations. Poisson's ratio, the ratio of lateral to longitudinal strain, can be calculated from the displacements measured by the extensometers using the equation

$$v = -\frac{\varepsilon_{lat}}{\varepsilon_{long}} = -\frac{\frac{\Delta D}{D}}{\frac{\Delta L}{L}} \tag{3.7}$$

where *D* is the length along the horizontal axis and *L* is the length along the vertical axis. The in-plane shear modulus *G* can then be calculated using **Equation 3.5**, and the remaining constant G' can be determined using the Saint-Venant principle [23], which approximates the shear modulus for orthotropic materials based on the values of the solved elastic constants as

$$\frac{1}{G_{ij}} = \frac{1}{E_i} + \frac{1+2v_{ji}}{E_j}. \tag{3.8}$$

When behavior is isotropic in the ij plane, as is the case for the x-y plane, this relation can be simplified to the form in **Equation 3.5**. A diagram of how each constant applies to a material is provided in **Figure 15**.

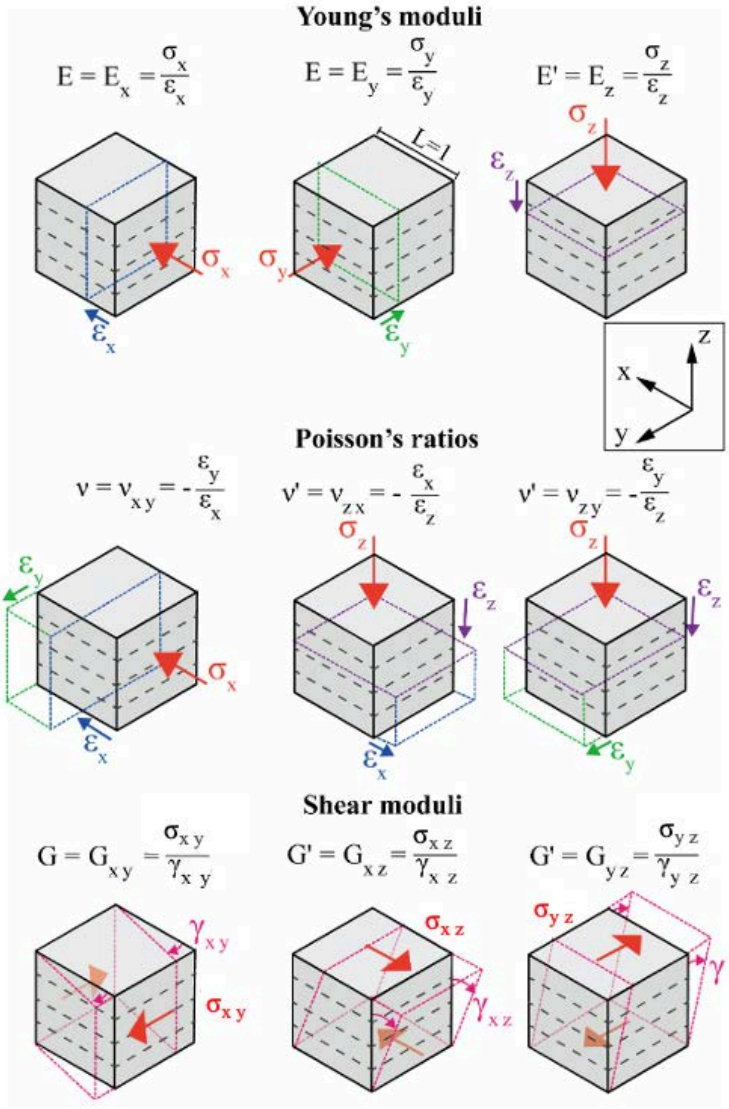

Figure 15. Schematic definition of the elastic constants in transversely isotropic material. Image adapted from Nejati et al. [23] with permission from the Journal of Rock Mechanics and Geotechnical Engineering.

Statistical Analysis

Differences between the mechanical properties of the two testing orientations were determined using independent sample t-tests. For all analyses, SPSS Statistics 26 (IBM, Armonk, NY) was used, and significance was determined at an alpha value of 0.05.

3.4 Results

Determination of Mechanical Properties

An example of a single loading cycle with a fitted line showing elastic modulus is provided in **Figure 16**. The calculated elastic constants are provided in **Table 4**. The elastic modulus values between the two testing directions differed by 6.2%, but no significant difference was found ($p = 0.29$). The similarity between the in-plane and transverse values suggests near isotropy for the linear-elastic behavior of AM solid PEEK.

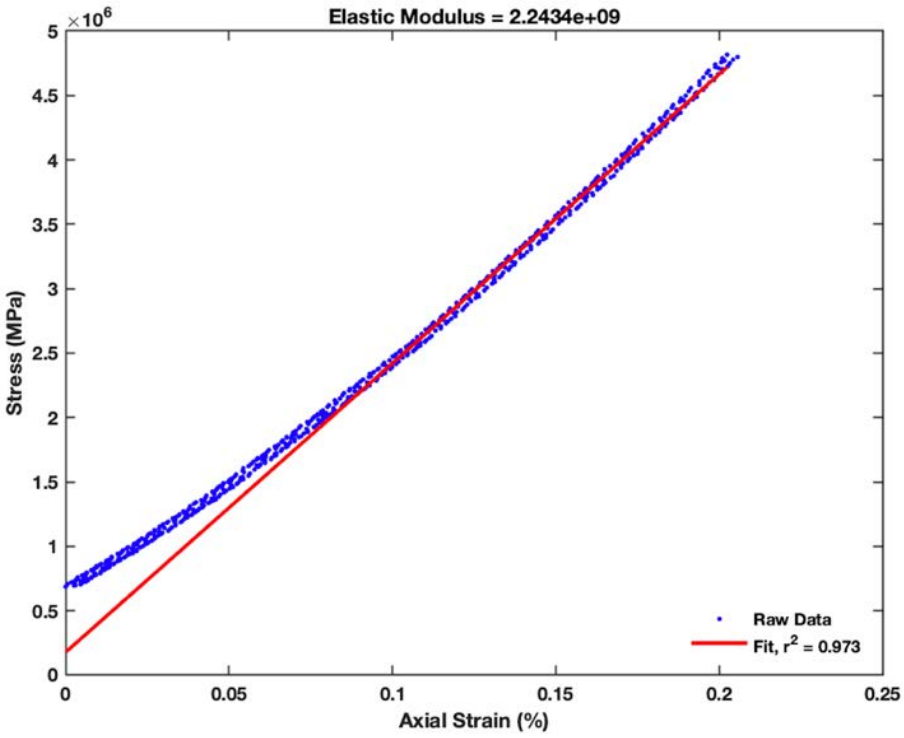

Figure 16. Data from a single compressive loading cycle with elastic modulus determined as the slope of the linear portion of the stress-strain curve.

Table 4. Elastic constants for solid PEEK determined via cyclic compression testing.

E (Gpa)	E' (Gpa)	v	v'	G' (Gpa)
2.20 ± 0.46	2.34 ± 0.22	0.29 ± 0.08	0.29 ± .06	0.885

For the compression to failure, the z-direction samples show a plateau following the linear-elastic region as the samples become compressed, and they were generally

more ductile than the xy-direction samples (**Figure 17**). No cracking was observed during loading for the z-direction, but some layer splitting occurred as the samples were unloaded. The measured yield stress was 58.0 ± 1.2 MPa and yield occurred around a strain of 0.05. The xy-direction samples failed suddenly following the linear-elastic region as the samples cracked and completely split along the layer interfaces. The measured yield strain for these samples was 68.0 ± 8.1 and yield occurred around a strain of 0.05. A difference of 14.8% was observed between the yield strength values, and this difference was statistically different ($p < 0.05$).

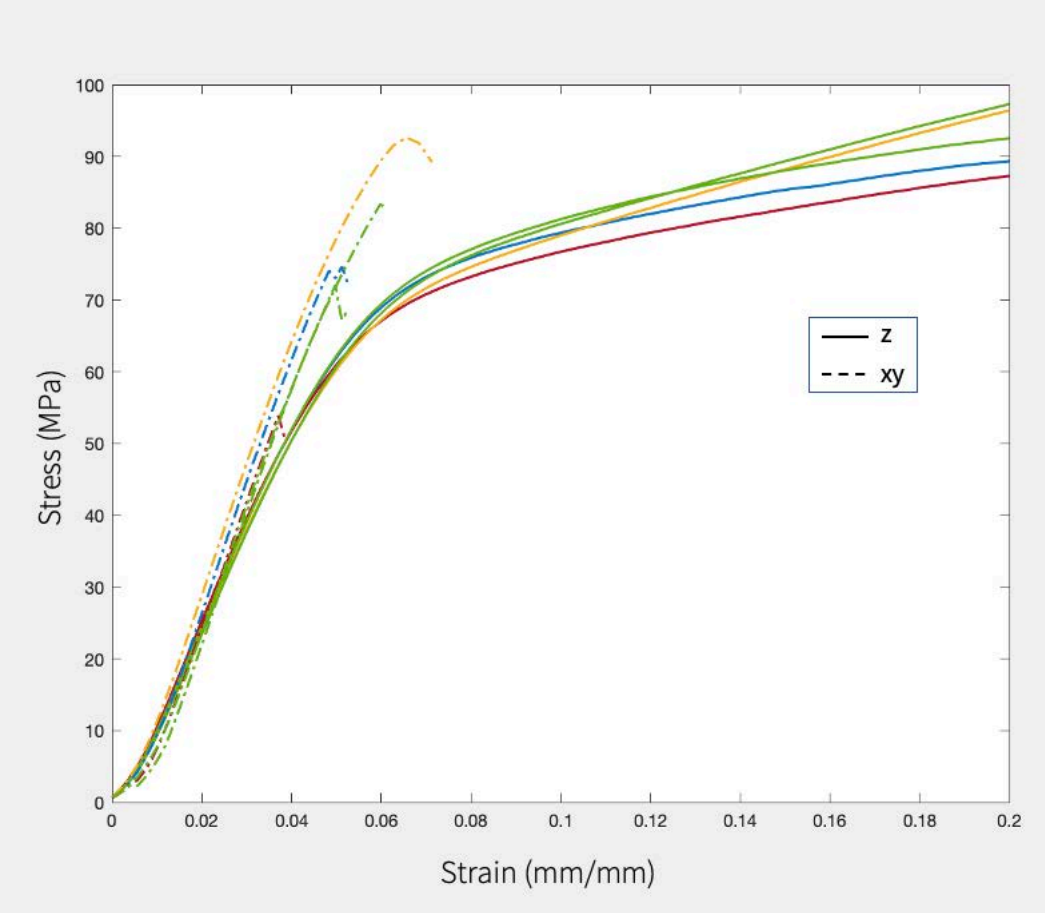

Figure 17. Stress-strain plots for solid PEEK loaded perpendicular and parallel to layer direction

Fracture Analysis

For both loading directions, post-compression samples showed cracking and splitting between layers, with most splits occurring cleanly at the layer interface. Individual layers remained intact even at the site of splitting, suggesting that the

interlayer bonding is weaker than the intralayer bonding. For the xy-direction samples, cracking coincided with failure during testing while cracking appeared on the z-direction samples after unloading. **Figure 18** shows the separation of layers in post-compression samples.

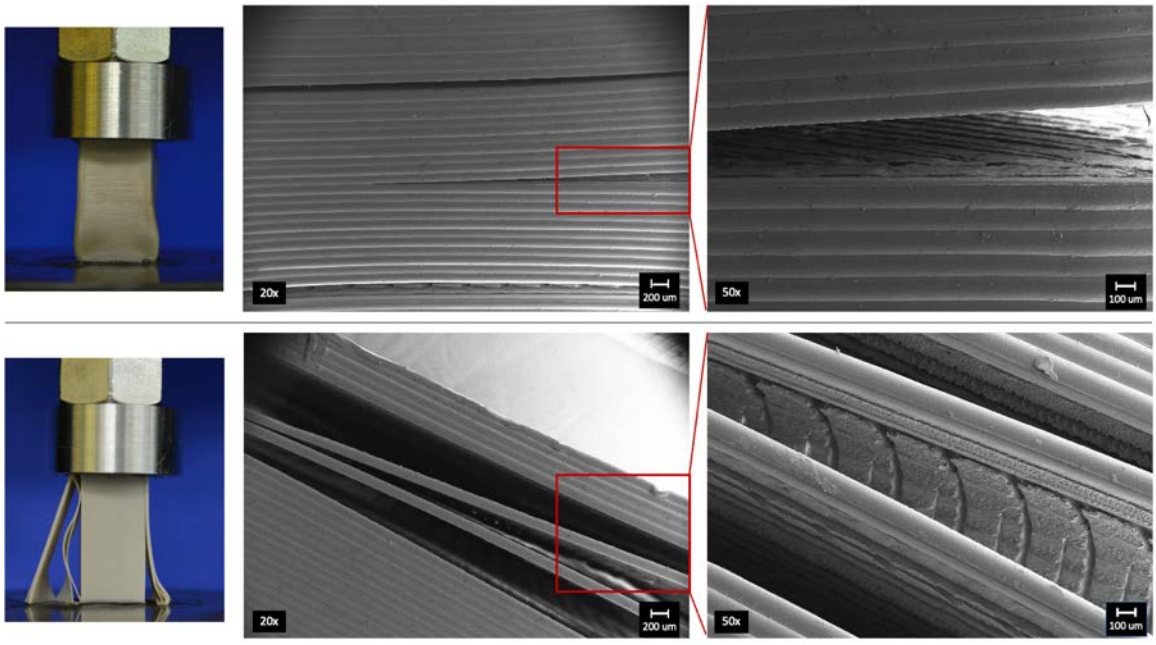

Figure 18. Layer splitting in z-direction samples (top) and xy-direction samples. Individual layers remained intact even after splitting from nearby layers

3.5 Discussion

The FFF printing process has been shown to result in transversely isotropic mechanical properties [9, 10, 16]. However, little is known about the directional properties of FFF PEEK, the constituent material of the porous structures

investigated throughout this thesis. The purpose of this study was to characterize the mechanical properties of solid nonporous PEEK created with the same print parameters (e.g., nozzle temperature, speed, layer height) used for creating porous PEEK structures, specifically to determine the elastic constants which can then be used in the modeling of more complex structures. In addition to reporting the compressive yield strength and elastic modulus of FFF PEEK, it was found that solid PEEK had a low degree of anisotropy between print orientations and failure resulting from debonding at the layer interface was observed.

This study had some limitations. First, the printing parameters used to create the solid PEEK was not varied to achieve a specific range of elastic constants, therefore the ability to draw conclusions regarding the effect of printing process factors on the mechanical properties of PEEK is limited. While varying the factors would be useful for determining how to further tune the structure properties and degree of anisotropy, the printing parameters established for creating porous PEEK structures were used to reduce confounding factors in later modeling and validation of those structures. Further, there are already several studies which have investigated the impact of FFF process parameters for PEEK, though the effect of chamber temperature has yet to be fully explored, and optimization of these parameters for increasing strength will be useful. Second, the study was limited to a single printer and PEEK formulation/manufacturer, and therefore may not be generalizable to other printers and PAEK materials. The printer used in this study was also an

experimental model, and future testing will be needed to determine if the results remain applicable for the commercial model, which allows for improved temperature and cooling control. Finally, the mechanical testing in this study was restricted to uniaxial compression, and shear properties and were not directly measured. However, shear modulus determination using the Saint-Venant principle has been shown to result in suitable approximation values for other transversely isotropic materials, particularly for materials with a low degree of anisotropy [23, 24]. Future direct measurement of shear properties and testing under different conditions to determine properties like fracture and fatigue behavior will be valuable for better understanding the FFF PEEK properties.

In this study the mechanical properties of solid PEEK were assessed, thus comparisons with existing studies will be limited to similarly solid samples with simple geometries (e.g. dog-bone, cylinder, or rectangular prism), while porous PEEK properties will be explored in **Chapter 5**. The material properties of solid PEEK have been studied most often in tension, with ranges of values reported for different manufacturing methods. For traditionally-made (e.g. injection or compression molded) PEEK at room temperature, yield strength in tension and compression are approximately 100 MPa and 125 MPa, respectively, while the tensile and compressive elastic moduli are 4 GPa and 3.2 GPa [8, 25]. PEEK samples created using AM have shown a range of success as compared to these benchmarks. For SLS, the maximum values found in the literature for tensile and compressive

yield strength were 88.7 MPa and 184 MPa, respectively, while maximum tensile and compressive elastic moduli were 2.76 GPa and 0.61 GPa, respectively [26-30]. For FFF PEEK, similar properties have been reported by existing studies which aim to optimize strength. Properties may approach, and in some compression cases exceed, that of injection molded PEEK. In the literature, reported maximum tensile and compressive yield strength values were found to be 99 MPa and 139 MPa, respectively, and maximum tensile and compressive moduli were found to be 4.1 GPa and 2.79 GPa, respectively [8, 31-33]. In this study, maximum average compressive yield strength and elastic modulus were measured as 68.0 MPa and 2.34 GPa thus achieving 54% of traditionally manufactured PEEK strength and 73% of stiffness. However, some confounding factors must be considered when comparing AM PEEK properties.

The mechanical properties of PEEK depend significantly on several factors, most notably the amount of material crystallization and, for AM PEEK, the degree of bonding between layers [9, 16, 34-37]. These factors of course are influenced by the manufacturing method. For PEEK created using FFF, it has been shown that printing parameters like nozzle temperature, nozzle diameter, raster angle, extrusion speed, and layer height may affect mechanical properties [4, 11, 18, 38-40], with perhaps the most impactful parameters being those related to the thermal history of the material [16, 36, 41]. This notion is exemplified by a study from Liaw et al. which uses a design of experiments approach to establish correlations between

printing parameters (nozzle temperature, print speed, layer height, and wait time between layers) and interlayer bonding [11]. It was found that nozzle temperature had the greatest impact on bonding, with increased temperature leading to greater flexural stress at break, flexural strain at break, and crystallinity [11]. Heat treatment by post-printing annealing also affected material properties though to a lesser effect, similar to what has been reported elsewhere [32, 40]. The influence of heat control can be attributed to its effect on polymer chain diffusion and entanglement across the interface of extruded filament, a concept some researchers aim to utilize to produce stronger bonds in AM [11, 36, 37, 41, 42]. Strategies include increasing the printing envelope temperature and controlling the cooling rate of deposited materials, with some studies reporting compressive yield strength as great as 87 MPa for unannealed samples [18]. While the yield strength determined in the current study is less than previous reports [18, 43, 44], it is important to note that the printing parameters were not optimized for strength as is the typical practice for determining FFF PEEK properties. Instead, the parameter selection was based on the ability to print the fine details of the various porous structures described in **Chapter 5**. The compressive elastic modulus for FFF PEEK is relatively less varied between studies, with most reported values falling between 1.8 and 2.9 GPa [31, 32, 43, 45], in agreement with the current findings.

In this study, the mechanical properties of solid PEEK under both in-plane and transverse loading were assessed, as the orientation of the sample plays an

important role determining its mechanical properties. This is especially true for FFF printing, which has been shown to result in transversely isotropic structures [13]. The degree of anisotropy imparted by the FFF process, especially for tensile properties, is well-studied for low temperature polymers but has been explored far less often for PEEK. One of the few studies reporting FFF PEEK properties for more than one build orientation comes from Arif et al. who printed dog bone samples both horizontally and vertically with raster angles of 0° (H-0°) and 90° (H-90° and V-90°) with respect to tensile loading direction [10]. A significant different was observed between the orientations, with the H-0°, H-90°, and V-90° samples reaching 84%, 74%, and 10% tensile strength of the referenced molded PEEK. Additionally, the authors characterize the morphology of the interfacial defects and point to the build chamber ambient temperature as an important factor in determining interfacial bonding, and therefore, anisotropy [10]. Similar findings were reported by Rinaldi et al. who showed that samples printed vertically achieved less than half the elastic modulus and less than 1/5 the tensile strength of horizontally printed samples [33]. Aside from tensile properties, PEEK print orientation has also been shown to affect Martens hardness parameters, flexural properties, and fracture toughness [10, 46, 47], though currently, to the author's knowledge, there are no studies which report FFF PEEK compressive properties for more than one build orientation. The findings demonstrate far less anisotropy between the in-plane and transverse properties compared to previous tensile

results, with stiffness and yield strength varying 6.2% and 14.8% respectively between the orientations. The relatively low degree of anisotropy for compressive properties agrees with some findings for FFF of low temperature polymers [48, 49]. Although future studies which optimize printing parameters to achieve increased layer bonding may result in even less anisotropy and greater strength, it is again important to note that the properties reported here resulted from a printing process particularly suited for porous structure creation.

Although AM PEEK has been receiving considerable attention for its use in orthopaedic devices, relatively little is known about its mechanical properties and the degree of anisotropy imparted by the FFF process. In this study, solid PEEK was printed and loaded both parallel and perpendicular to the layer deposition direction in order to determine the elastic constants for solid FFF-printed PEEK. It was found that the elastic modulus and yield strength was similar between the two orientations, and the results therefore did not support the hypothesis of transverse isotropy for the material. Ultimately, in addition to supporting the porous PEEK modeling in the upcoming chapters, the findings reported here may help inform future studies regarding additively manufactured PEEK for medical devices and other applications.

3.6 References

1. Otero, J.J., A. Vijverman, and M.Y. Mommaerts, *Use of fused deposit modeling for additive manufacturing in hospital facilities: European certification directives.* Journal of Cranio-Maxillofacial Surgery, 2017. **45**(9): p. 1542-1546.

2. Awad, A., et al., *3D printed medicines: A new branch of digital healthcare.* International journal of pharmaceutics, 2018. **548**(1): p. 586-596.

3. Aimar, A., A. Palermo, and B. Innocenti, *The role of 3D printing in medical applications: a state of the art.* Journal of healthcare engineering, 2019. **2019**.

4. Sharma, N., et al., *Quality Characteristics and Clinical Relevance of In-House 3D-Printed Customized Polyetheretherketone (PEEK) Implants for Craniofacial Reconstruction.* Journal of Clinical Medicine, 2020. **9**(9): p. 2818.

5. Panayotov, I.V., et al., *Polyetheretherketone (PEEK) for medical applications.* J Mater Sci Mater Med, 2016. **27**(7): p. 118.

6. Basgul, C., et al., *Structure, properties, and bioactivity of 3D printed PAEKs for implant applications: A systematic review.* Journal of Biomedical Materials Research Part B: Applied Biomaterials, 2021.

7. Wang, Y., et al., *Parameters influencing the outcome of additive manufacturing of tiny medical devices based on PEEK.* Materials, 2020. **13**(2): p. 466.

8. Zanjanijam, A.R., et al., *Fused filament fabrication of peek: A review of process-structure-property relationships.* Polymers, 2020. **12**(8): p. 1665.

9. Costa, A.E., A.F. da Silva, and O.S. Carneiro, *A study on extruded filament bonding in fused filament fabrication.* Rapid Prototyping Journal, 2019.

10. Arif, M., et al., *Performance of biocompatible PEEK processed by fused deposition additive manufacturing.* Materials & Design, 2018. **146**: p. 249-259.

11. Liaw, C.-Y., et al., *Interlayer bonding strength of 3D printed PEEK specimens.* Soft Matter, 2021. **17**(18): p. 4775-4789.

12. Casavola, C., et al., *Orthotropic mechanical properties of fused deposition modelling parts described by classical laminate theory.* Materials & design, 2016. **90**: p. 453-458.

13. Gao, X., et al., *Fused filament fabrication of polymer materials: A review of interlayer bond.* Additive Manufacturing, 2020: p. 101658.

14. Bertoldi, M., et al. *Mechanical characterization of parts processed via fused deposition*. in *1998 International Solid Freeform Fabrication Symposium*. 1998.

15. Coogan, T.J. and D.O. Kazmer, *Bond and part strength in fused deposition modeling.* Rapid Prototyping Journal, 2017.

16. Basgul, C., et al., *Thermal localization improves the interlayer adhesion and structural integrity of 3D printed PEEK lumbar spinal cages.* Materialia, 2020. **10**: p. 100650.

17. International, A., *D695-15 Standard Test Method for Compressive Properties of Rigid Plastics*. ASTM International: West Conshohocken, PA.

18. Wang, Y., et al., *Mechanical properties of fused filament fabricated PEEK for biomedical applications depending on additive manufacturing parameters.* journal of the mechanical behavior of biomedical materials, 2021. **115**: p. 104250.

19. Basgul, C., et al., *Structure–property relationships for 3D-printed PEEK intervertebral lumbar cages produced using fused filament fabrication.* Journal of materials research, 2018. **33**(14): p. 2040-2051.

20. *ISO/IEC 17025:2005. General requirements for the competence of testing and calibration laboratories International Organization for Standardization.* 2017: Geneva, Switzerland.

21. International., A., *D695-15 Standard Test Method for Compressive Properties of Rigid Plastics*. 2015, ASTM International: West Conshohocken, PA.

22. Horgan, C.O. and J.K. Knowles, *Recent developments concerning Saint-Venant's principle.* Advances in applied mechanics, 1983. **23**: p. 179-269.

23. Nejati, M., M.L.T. Dambly, and M.O. Saar, *A methodology to determine the elastic properties of anisotropic rocks from a single uniaxial compression test.* Journal of Rock Mechanics and Geotechnical Engineering, 2019. **11**(6): p. 1166-1183.

24. WOROTNICKI, G., *CSIRO triaxial stress measurement cell*, in *Rock Testing and Site Characterization*. 1993, Elsevier. p. 329-394.

25. Rae, P., E. Brown, and E. Orler, *The mechanical properties of poly (ether-ether-ketone)(PEEK) with emphasis on the large compressive strain response.* Polymer, 2007. **48**(2): p. 598-615.

26. El Halabi, F., et al., *Mechanical characterization and numerical simulation of polyether–ether–ketone (PEEK) cranial implants.* Journal of the mechanical behavior of biomedical materials, 2011. **4**(8): p. 1819-1832.

27. Shishkovsky, I., et al., *Nano-size ceramic reinforced 3D biopolymer scaffolds: Tribomechanical testing and stem cell activity.* Composite Structures, 2018. **202**: p. 651-659.

28. Hoskins, T., K. Dearn, and S. Kukureka, *Mechanical performance of PEEK produced by additive manufacturing.* Polymer Testing, 2018. **70**: p. 511-519.

29. Beitz, S., et al., *Influence of powder deposition on powder bed and specimen properties.* Materials, 2019. **12**(2): p. 297.

30. Berretta, S., K.E. Evans, and O. Ghita, *Processability of PEEK, a new polymer for High Temperature Laser Sintering (HT-LS).* European Polymer Journal, 2015. **68**(Supplement C): p. 243-266.

31. Han, X., et al., *Carbon fiber reinforced PEEK composites based on 3D-printing technology for orthopedic and dental applications.* Journal of clinical medicine, 2019. **8**(2): p. 240.

32. Tseng, J.-W., et al., *Screw extrusion-based additive manufacturing of PEEK.* Materials & Design, 2018. **140**: p. 209-221.

33. Rinaldi, M., et al., *Additive layer manufacturing of poly (ether ether ketone) via FDM.* Composites Part B: Engineering, 2018. **145**: p. 162-172.

34. Chivers, R. and D. Moore, *The effect of molecular weight and crystallinity on the mechanical properties of injection moulded poly (aryl-ether-ether-ketone) resin.* Polymer, 1994. **35**(1): p. 110-116.

35. Kurtz, S.M. and J.N. Devine, *PEEK biomaterials in trauma, orthopedic, and spinal implants.* Biomaterials, 2007. **28**(32): p. 4845-69.

36. Han, P., et al., *Effect of in-process laser interface heating on strength isotropy of extrusion-based additively manufactured PEEK.* Procedia Manufacturing, 2020. **48**: p. 737-742.

37. Yang, C., et al., *Influence of thermal processing conditions in 3D printing on the crystallinity and mechanical properties of PEEK material.* Journal of Materials Processing Technology, 2017. **248**: p. 1-7.

38. Deng, X., et al., *Mechanical properties optimization of poly-ether-ether-ketone via fused deposition modeling.* Materials, 2018. **11**(2): p. 216.

39. Li, Y. and Y. Lou, *Tensile and Bending Strength Improvements in PEEK Parts Using Fused Deposition Modelling 3D Printing Considering Multi-Factor Coupling.* Polymers, 2020. **12**(11): p. 2497.

40. Basgul, C., et al., *Does annealing improve the interlayer adhesion and structural integrity of FFF 3D printed PEEK lumbar spinal cages?* Journal of the mechanical behavior of biomedical materials, 2020. **102**: p. 103455.

41. Luo, M., et al., *Controllable interlayer shear strength and crystallinity of PEEK components by laser-assisted material extrusion.* Journal of Materials Research, 2018. **33**(11): p. 1632.

42. Sun, Q., et al., *Effect of processing conditions on the bonding quality of FDM polymer filaments.* Rapid prototyping journal, 2008.

43. Rahman, K.M., T. Letcher, and R. Reese, *Mechanical Properties of Additively Manufactured PEEK Components Using Fused Filament Fabrication*. 2015.

44. Wu, W., et al., *Influence of layer thickness and raster angle on the mechanical properties of 3D-printed PEEK and a comparative mechanical study between PEEK and ABS.* Materials, 2015. **8**(9): p. 5834-5846.

45. Vaezi, M. and S. Yang, *Extrusion-based additive manufacturing of PEEK for biomedical applications.* Virtual and Physical Prototyping, 2015. **10**(3): p. 123-135.

46. Li, Q., et al., *Flexural properties and fracture behavior of CF/PEEK in orthogonal building orientation by FDM: Microstructure and mechanism.* Polymers, 2019. **11**(4): p. 656.

47. Prechtel, A., et al., *Comparison of various 3D printed and milled PAEK materials: Effect of printing direction and artificial aging on Martens parameters.* Dental Materials, 2020. **36**(2): p. 197-209.

48. Lee, C., et al., *Measurement of anisotropic compressive strength of rapid prototyping parts.* Journal of materials processing technology, 2007. **187**: p. 627-630.

49. Song, Y., et al., *Measurements of the mechanical response of unidirectional 3D-printed PLA.* Materials & Design, 2017. **123**: p. 154-164.

Chapter 4: Modeling of Triply Periodic Minimal Surface Architectures and Mechanical Properties for 3D Printed PEEK

4.1 Abstract

With the widespread adoption of additive manufacturing for medical and industrial applications, more and more designers are turning to triply periodic minimal surfaces (TPMSs) to achieve desirable material characteristics. Therefore, the aim of this study was to create useful design tools for visualizing the interplay between TPMS design parameters and resulting architecture, and to predict the resulting mechanical properties. A custom MATLAB script was written to model and analyze families of gyroid and diamond TPMS-based structures in order to visualize the relationships between the TPMS equation scaling factor, strut thickness, porosity, and pore size. Then, to simplify the analysis of micromechanics for these complex structures, a representative volume element (RVE) of each porous structure was defined and numerical homogenization was performed to determine the predicted effective Young's moduli. The stiffness and porosity data were fit to the Gibson-Ashby scaling laws, and regression analysis was used to establish the relationships between the effective modulus and structural properties for each TPMS geometry. It was observed that predicted stiffness was similar between the geometries with slightly greater values for the diamond, and that the moduli

decreased quadratically with increasing porosity indicating a good fit with the proposed scaling laws. Plots of the stiffness values showed that while the structures were not completely isotropic, the Young's modulus values did not differ between the principal directions within a unit cell. Validation of these models for FFF PEEK will be carried out in the next chapter.

4.2 Introduction

For orthopaedic and spinal procedures including total joint arthroplasty and spinal fusion, long-term treatment success and prevention of implant loosening relies greatly on secure fixation between the host bone and device. For this reason, devices are often designed with highly porous surfaces which have a high strength-to-weight ratio, micro-texture for cell adhesion, and increased surface area allowing for greater amounts of perfusion and osseointegration [1-4]. Traditionally, orthopaedic bone ingrowth surfaces have been created using powder metallurgy or foaming technologies [3-5], though these methods allow for limited control of the porous characteristics. Additive manufacturing, on the other hand, provides greater control of porous surface properties and is being adopted by implant manufacturers for traditional implant metals like titanium alloy [6-8]. However, the cost, safety infrastructure, and necessary postprocessing associated with metal 3D printing may limit its widespread adoption into hospital settings [9-11].

As researchers continue to develop osseointegrative porous materials, a variety of geometries have been investigated, ranging from tessellated truss-based polyhedral shapes to stochastic structures such as Voronoi patterns [12, 13]. Recently, as 3D printing has allowed for the creation of more complex geometries, interest has been growing for porous structures design from triply periodic minimal surfaces (TPMSs) [13-16]. TPMSs are a family of minimal surfaces (i.e., having a mean curvature of zero at every point) which repeat in three directions and divide space up into interconnected void regions. The unit cell geometries can be repeated infinitely in each direction to build up a larger structure, and most are free from self-intersections and sharp corners that may result in stress-concentrations [17-19]. Certain TPMS geometries like the Schoen gyroid and Schwarz diamond types display unique properties which make them particularly well-suited for bone ingrowth materials, and studies have shown positive results both *in vitro* and *in vivo* for laser-based additive manufacturing methods [19-22]. In one study, Ma et al. created stainless steel gyroid-type TPMS structures and investigated bone cell attachment and proliferation in addition to structure morphology and mechanical properties [20]. The study reported Young's modulus and yield strength within the range of human bone for a variety of pore sizes and porosities and found structure permeability and related mass transport properties to be a significant factor in determining cell response [20]. In one of the few *in vivo* studies, Li et al. created Ti6Al4V porous structures designed using the primitive-type TPMS and assessed early osseointegration into the tibias of mini pigs [19]. The results were promising,

with significantly greater push-out forces and ingrown bone volume for the TPMS structures compared to solid material. The authors speculate that the excellent osseointegration results were attributable to the porous structure interconnectivity and curvature, promoting vascularization and bone tissue regeneration, respectively [19]. Like many others, each of these studies demonstrate the most common method of modelling TPMSs, that is, using a surface-approximating implicit functions derived from Fourier series expansions [16, 23, 24]. While this represents perhaps the most common method of TPMS modeling, it should be noted that most studies fail to describe a systematic method for manipulating the equations to achieve predetermined pore sizes and porosities.

In addition to the architecture, the mechanical properties of porous bone ingrowth surface also play an essential role in osseointegration. The material must be strong enough to withstand initial fixation and expected loading conditions, yet the Young's modulus must not be too large, as significant mismatch between bone and device stiffness can result in stress shielding [1, 4, 25]. TPMS structures are well-suited to meet these criteria, and studies have shown success in tuning the mechanical properties through manipulating the pore size, strut size, and porosity [20, 26, 27]. Predicting these properties plays an important role in the design process of medical devices. This presents a challenge, however, as modeling and analysis of microstructures is computationally expensive, and as the porous geometries become more complex, so too does the process of predicting their properties using

traditional finite element methods. An alternative approach can be taken using homogenization theory, which allows for the modeling of a heterogeneous material with a periodic microstructure as a homogeneous solid with equivalent effective material properties [26, 28, 29]. In this method, a representative volume element (RVE) of the periodic structure is used. Some studies have used homogenization theory to predict the mechanical responses of trabecular bone [30, 31], and others have used it for 3D printed periodic structures, often finding that the results of this method show agreement with traditional FEM and experimental values [13, 26, 27, 32, 33]. However, most of these analyses have so far been specific to metallic materials and laser-based AM. Now that TPMS structures can be 3D printed from implantable polymers (e.g., PEEK) with methods suitable for in-hospital use, creating an applicable model of mechanical response can help further advance point of care implant manufacturing.

In this study, one goal is to provide a tool for designers wanting to utilize TPMSs, specifically the gyroid and diamond types, with control over the structure pore size and porosity. Another goal is to predict the effective elastic properties of the TPMS-based porous structures using a homogenization method and to visualize the relationship between the resulting structural and mechanical properties. Importantly, the modeling in this chapter is designed to be applicable regardless of base constituent material. Evaluation of the model specifically for FFF PEEK will be performed in the following chapter.

4.3 Methods

Modeling of Triply Periodic Minimal Surfaces

A custom script was written in MATLAB 2021a (MathWorks, Natick, MA) to model the TPMS structures and determine their structural properties. The flow of the coding scheme can be divided into three parts: TPMS 3D plotting, structure thickening, and image analysis (**Figure 19**). In the first step, the TPMS structures are plotted in three dimensions using the approximation equations

$$U_{Gyroid} = \cos(k_x x) * \sin(k_y y) + \cos(k_y y) * \sin(k_z z) + \cos(k_z z) * \sin(k_x x) - t \quad (4.1)$$

$$U_{Diamond} = \sin(k_x x) * \sin(k_y y) * \sin + \sin(k_x x) * \cos(k_y y) * \cos(k_z z) + \cos(k_x x) * \sin(k_y y) * \cos(k_z z) + \cos(k_x x) * \cos(k_y y) * \sin(k_z z) - t \quad (4.2)$$

where x, y, and z are spatial coordinates and t determines the volume fraction on either side of the surface. For each equation, $U = 0$ represents the isosurface that can be treated as the boundary between solid and void space. The parameter k_i defines the surface periodicities as

$$k_i = 2\pi \frac{n_i}{s_i} \text{ (with } i = x, y, z) \tag{4.3}$$

where n_i is the number of unit cell repetitions (2π being the cubic side length of a single unit cell) and s_i represents a scaling factor. The parameters s and k can be varied to modify the surface architecture, with values of n =1, $t = 0$, and $s = 1$ serving as a single "standard" unit cell. For the remainder of this work, t will remain equal to 0 and volume fraction will be more directly modulated by varying strut thickness for the solidified surface. Of note, the parameter t is often used for the purpose of creating TPMS with graded density [27, 34]. The approach in this work, that is, assigning the desired thickness to the plotted surface itself, provides a sheet-based solid network. Alternatively, a strut-based network could be achieved by solidifying one of the volumes on either side of the surface [35, 36]. Scaling factor s will be varied between minimum and maximum values at which the integrity of porous architecture is lost, as values too small can result in pore occlusion when thickened and values too large result in a loss of a defined, interconnected pore structure. In this work, s values remain within the interval 0.3 to 1.1.

The second step of modeling involves solidifying these volume-less approximation surfaces with a selected strut thickness. There is no minimum to the thickness value that can be chosen, but designers should choose a value within their means of manufacturing. The maximum possible thickness is the one at which the pores become occluded. This maximum depends on the TPMS type and scaling factor, with greater strut thicknesses being possible for greater scaling factors. In this work thickness is distributed evenly on either side of the surface to ensure equal pore sizes throughout, however adding thickness on an offset is also possible for achieving pores of alternating size. Once thickened, the volume of the solid portion is then calculated and can be used to determine the structure porosity with the equation

$$porosity = \left(1 - \frac{v_{solid}}{v_{total}}\right) * 100 \tag{4.4}$$

where v_{solid} represents the volume of the solidified TPMS and v_{total} represents the volume of the cubic space occupied by the structure. The third step involves image analysis to determine pore size using a best fit circle function. In this process, the pixels of the solidified TPMS image are separated into solid and void space, and the diameter of the best fit circle in each pore is measured.

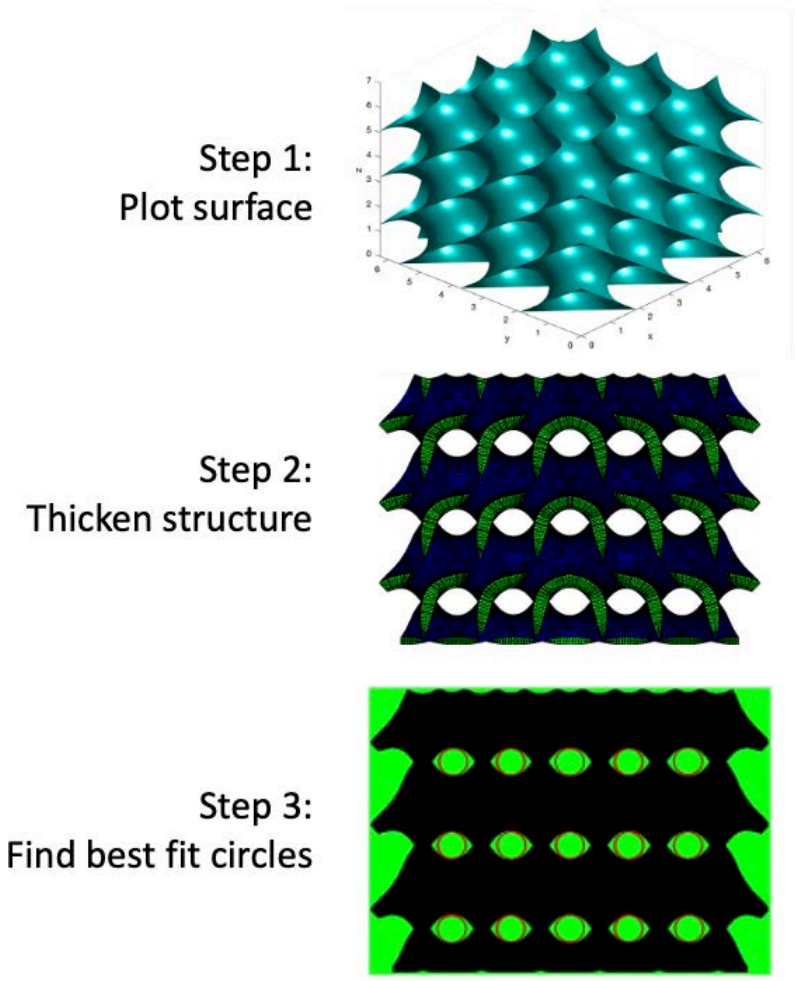

Figure 19. Flow of the coding scheme written to generate solid TPMS structures and calculate the resulting volume, porosity, and pore size

This modeling and analysis scheme was performed for families of diamond and gyroid TPMS structures with combinations of scaling factors and strut thicknesses. Scaling factors ranged from 0.3 to 1.1, and thicknesses ranged from 0.1 mm to the respective maximum value at which the pores became closed for each scaled

architecture. The results were plotted to show the interplay between TPMS type, scaling factor, strut thickness, pore size, and porosity.

Periodic Material Homogenization

In the prediction of mechanical properties for periodic materials, a representative volume element is often defined to simplify the analysis. An RVE is the smallest unit of material that can accurately represent the overall macroscale structure, and must be sufficiently large as to capture the microstructural heterogeneities in the bulk material [29, 37]. In this work, a single unit cell of each TPMS architecture represents the RVE.

The method of homogenization used in this thesis involves the asymptotic expansion of a relevant field variable (displacement, in the case of elasticity theory) to predict the effective properties of the repeating unit cell [29, 30, 38]. A summary of the relevant equation derivations is provided in **Chapter 1** (Equations 1.1 - 1.9). This scheme is performed numerically by discretizing the relevant equations and solving using finite element methods.

Equation 1.9 can be discretized and solved using displacement-based finite element analysis [29, 39, 40]. Simplified, Equation 1.9 can be written as

$$K\chi^{kl} = f^{kl} \tag{4.5}$$

where K is the global stiffness matrix, χ^{kl} is the microscopic displacement, and f^{kl} represents the load vector. The left side of the equation denoting the stiffness matrix K, can be discretized as

$$K = \sum_{e=1}^{N} \int_{V_e} B_e^T C_e B_e dV_e \tag{4.6}$$

where the summation denotes the assembly operator for N finite elements, V_e is the element volume, B_e is the strain-displacement matrix of the element with superscript "T" denoting the matrix transpose, and C_e is the constitutive matrix of the element. The discretized right side of Equation 4.5 can be written as

$$f^{kl} = \sum_{e=1}^{N} \int_{V_e} B_e^T C_e \, \bar{\varepsilon}_{kl} dV_e \tag{4.7}$$

where f^{kl} denotes the load vector and $\bar{\varepsilon}_{kl}$ corresponds to a chosen strain field, with 6 load cases needed for solving the problem in 3D (3 cases for 2D). Written as a linear combination of unit strains, $\bar{\varepsilon}_{kl}$ will be defined as

$$\bar{\varepsilon}_{11} = (1,0,0,0,0,0)^T, \quad \bar{\varepsilon}_{22} = (0,1,0,0,0,0)^T, \quad \bar{\varepsilon}_{33} = (0,0,1,0,0,0)^T,$$
$$\bar{\varepsilon}_{12} = (0,0,0,1,0,0)^T, \quad \bar{\varepsilon}_{23} = (0,0,0,0,1,0)^T, \quad \bar{\varepsilon}_{31} = (0,0,0,0,0,1)^T. \tag{4.8}$$

After applying the macroscopic unit strains to Equation 4.7, the force vector can be used to determine the microscopic displacement with Equation 4.5. The fluctuating strain tensor can be determined from the strain-displacement matrix used to calculate the microscopic strain tensor using Equation 1.3. The local structural tensor M_{ijkl} can be determined using the relationship between macroscopic and microscopic strain:

$$\varepsilon_{ij} = M_{ijkl}\bar{\varepsilon}_{kl}. \tag{4.9}$$

The local structural tensor can be used to determine the effective stiffness tensor C_{ijkl} by starting from the equation provided by Hooke's law

$$\sigma_{ij} = C_{ijkl}\varepsilon_{kl}. \tag{4.10}$$

Equation 4.10 can be integrated over the RVE on both sides and divided by the RVE volume, with a substitution for ε_{kl} using Equation 4.9 to give

$$\bar{\sigma}_{ij} = \frac{1}{|V_{RVE}|}\int_{V_{RVE}} C_{ijpm} M_{pmkl} dV_{RVE} \bar{\varepsilon}_{kl} \tag{4.11}$$

from which the effective macroscopic stiffness tensor can be computed as

$$\bar{C}_{ijkl} = \frac{1}{|V_{RVE}|}\int_{V_{RVE}} C_{ijpm} M_{pmkl} dV_{RVE} \ . \tag{4.12}$$

More thorough derivations of the RVE analysis, homogenization equations, and implementation via FEA are provided by early works on the subject [29, 30, 41, 42].

For this work, the homogenization scheme was performed using nTopology v 3.2.4, (nTopology Inc., New York City, NY). Sixty unit cells with varying strut size, pore size, and porosity were modeled to serve as the RVEs for gyroid (n = 30) and diamond (n = 30) geometries. Meshes with tetrahedral elements were generated for each structure and a mesh convergence test was conducted to confirm that the results were not influenced by the mesh size. The homogenization process was then implemented to find the compliance matrix for each unit cell and to generate a 3D plot of its effective elastic moduli in each direction. A custom MATLAB script was used to determine the effective elastic modulus values from each compliance matrix, and the moduli were normalized by the bulk material elastic modulus used in the homogenization scheme to remove the effect of the bulk constituent material. MATLAB was also used to fit a second degree polynomial surface to the TPMS data

to show the relationship between pore size, strut size, and normalized elastic modulus and to perform a regression analysis to identify coefficients for the Gibson-Ashby scaling law [43] given as

$$\frac{E}{E_0} = C(\frac{\rho}{\rho_0})^n \tag{4.13}$$

where $\frac{E}{E_0}$ is the relative modulus, $\frac{\rho}{\rho_0}$ is the relative density, C is the geometric constant and n is the exponent of power. Zener ratio was also determined from the compliance matrix to quantify the anisotropy of the structures, using the equation

$$A_Z = \frac{2C_{44}}{C_{11} - C_{12}} \tag{4.14}$$

where C_{ij} are the elastic constants.

4.4 Results

Modeling of Triply Periodic Minimal Surfaces

The comprehensive list of resulting pore size and porosity values for combinations of scaling factors and thickness values can be found in **Appendix A**, and the values were also plotted for each TPMS type (**Figure 20**). From the plots it appears that while pore size is similarly dependent on strut thickness and scaling factor, porosity

appears more effected by thickness than *s*. The tables and plots can be used to determine the necessary scaling factor and strut thickness needed to achieve a target porosity and/or pore size. Boundaries can also be added to the plots to establish a design space for a desired architecture or to denote the limits of a manufacturing method. For example, if aiming to design a TPMS with features similar to trabecular bone at a particular anatomical location, the plot lines corresponding to the applicable ranges of strut thickness, pores size, and porosity may be used as limits. **Figure 21** demonstrates this concept using structural features of trabecular bone reported for the patella and proximal tibia. In another example, a design space for more generalized trabecular bone is presented with bounds corresponding to porosity greater than 50% and pore size between 0.40 and 1.20 mm [44]. This design space can be further bounded with the addition of a limit at the minimum strut thickness achievable by a given manufacturing method. In the case of FFF printing with a 0.2 mm nozzle diameter, a strut thickness of at least 0.2 mm may be required (**Figure 21**).

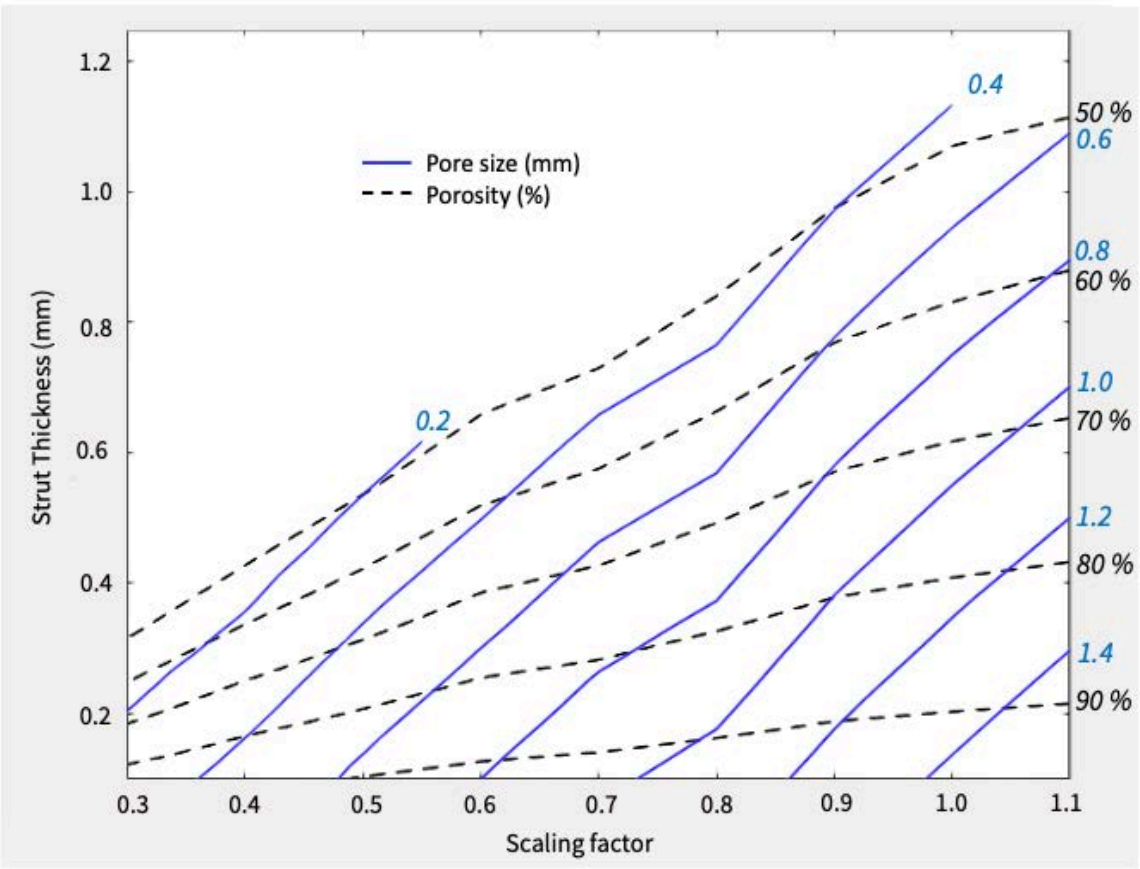
Gyroid TPMS
Strut Thickness (mm)
Scaling factor
Pore size (mm)
Porosity (%)
0.2
0.4
0.6
0.8
1.0
1.2
1.4
50 %
60 %
70 %
80 %
90 %
1.2
1.0
0.8
0.6
0.4
0.2
0.3
0.4
0.5
0.6
0.7
0.8
0.9
1.0
1.1

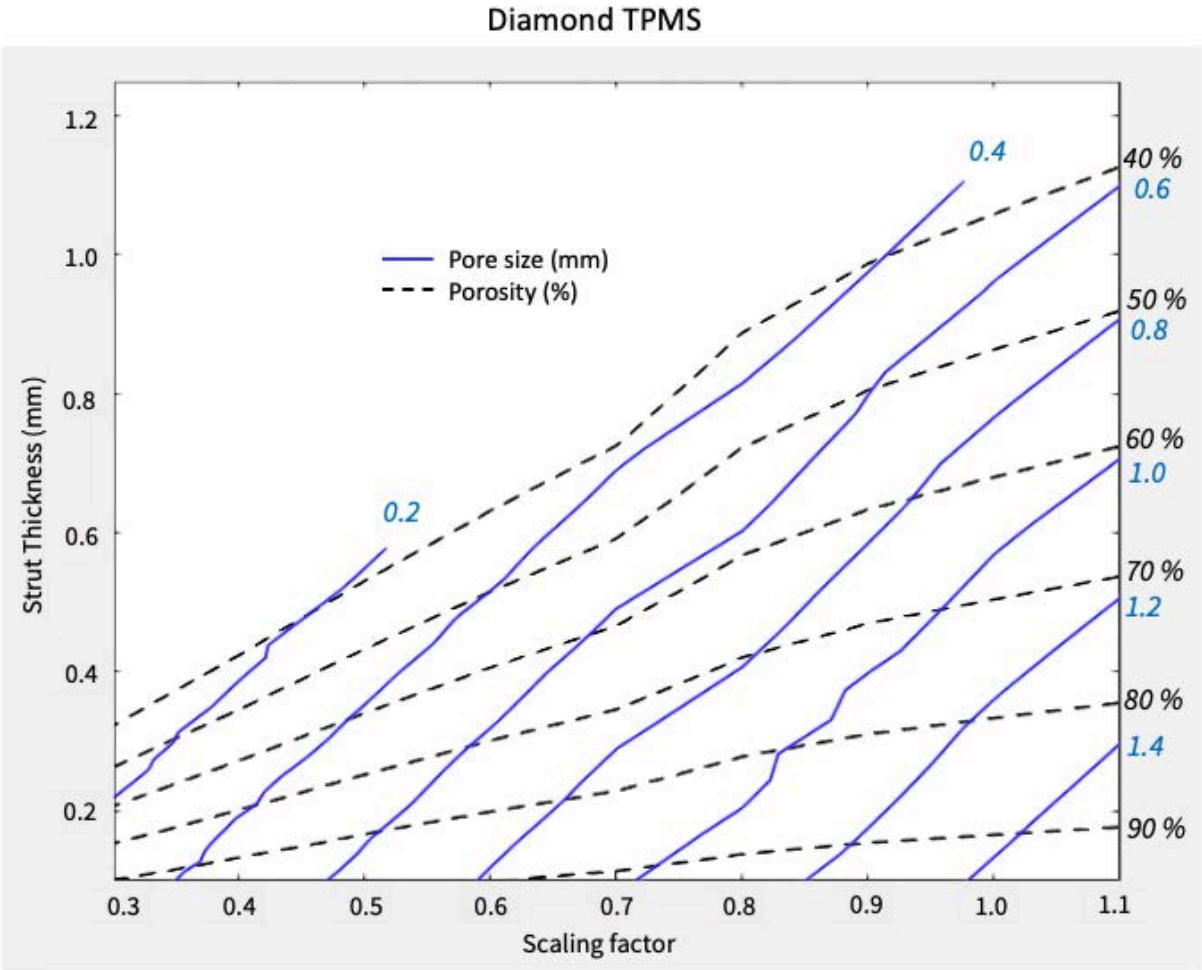

Figure 20. (Top) Gyroid and (bottom) diamond TPMS design plots showing the relationship between design parameters (scaling factor and strut thickness) and resulting properties (pore size and porosity).

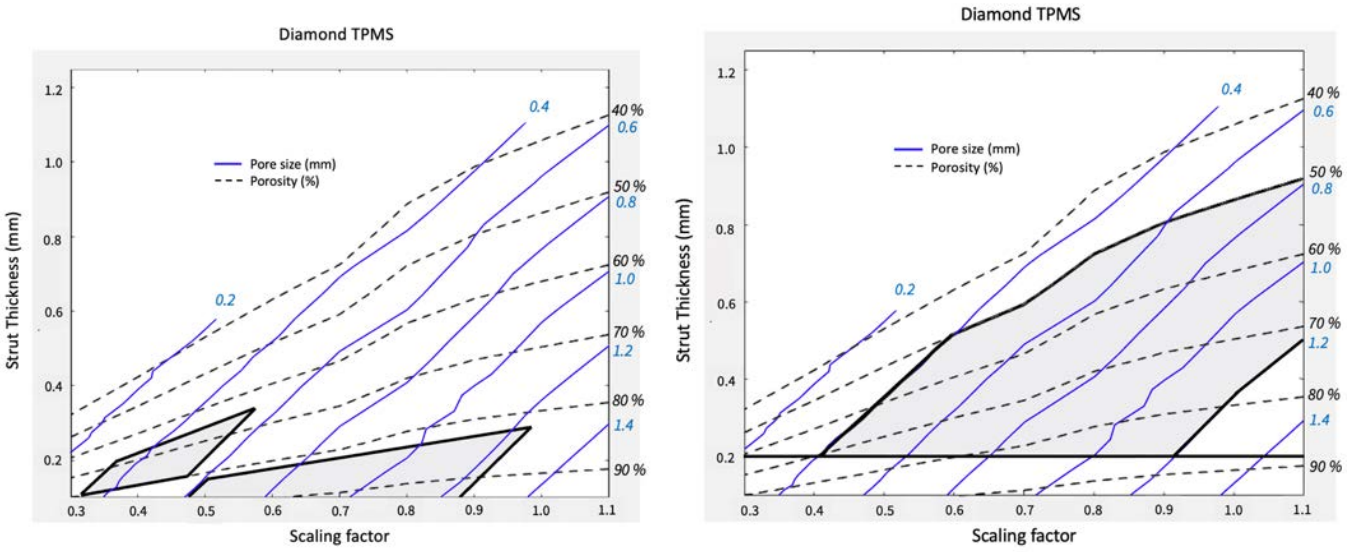

Figure 21. Example TPMS design plots bounded for particular design goals. (Left) Plot bounded by structural ranges for trabecular bone in the patella (porosity 67 – 80% and pore size 0.32 – 0.56 mm) [45] and proximal tibia (porosity 82 – 95% and pore size 0.61 – 1.23 mm) [46]. (Right) Plot bounded by general trabecular bone ranges (porosity > 50% and pore size 0.40 – 1.20 mm) [44] and minimum print extrusion diameter of 0.2 mm.

Periodic Material Homogenization

The 30 unit cells for each TPMS geometry were successfully modeled and homogenized. An example of the homogenization output is provided in **Figure 22**. It was evident from the differing degrees of protrusions in the 3D modulus plots that the overall degree of anisotropy varied slightly between unit cells, though in each case the effective elastic modulus did not differ between the three principal directions (**Figure 22**). Thus, only the normalized E_1 values are reported for both the gyroid and diamond in subsequent plots. The Zener ratio moved further from one (with a value of one indicating isotropy) as porosity increased, indicating greater

anisotropy for more porous structures (**Figure 23**). Fitting the data to the power law provided by Gibson and Ashby shows that the effective elastic modulus tends to decrease with increasing porosity (**Figure 24**). The data was fit with an R^2 value of 0.965 for the gyroid and 0.970 for the diamond. C and n values of 0.68 and 1.51 were found for the gyroid architecture, and C and n values of 0.66 and 1.29 were found for the diamond.

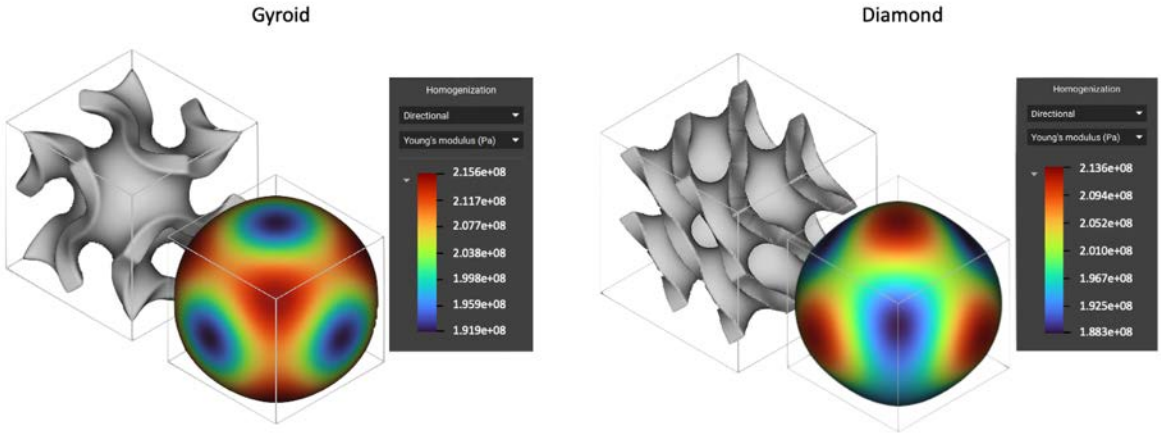

Figure 22. Example unit cells with corresponding spatial plots of effective Young's modulus determining using homogenization.

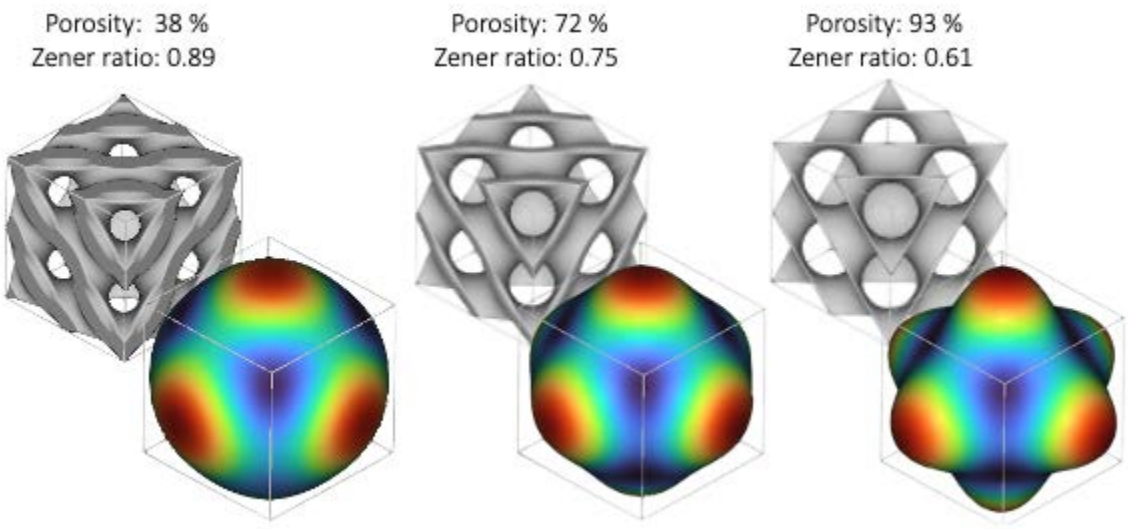

Figure 23. Visualization of the increase in anisotropy as structure porosity increases.

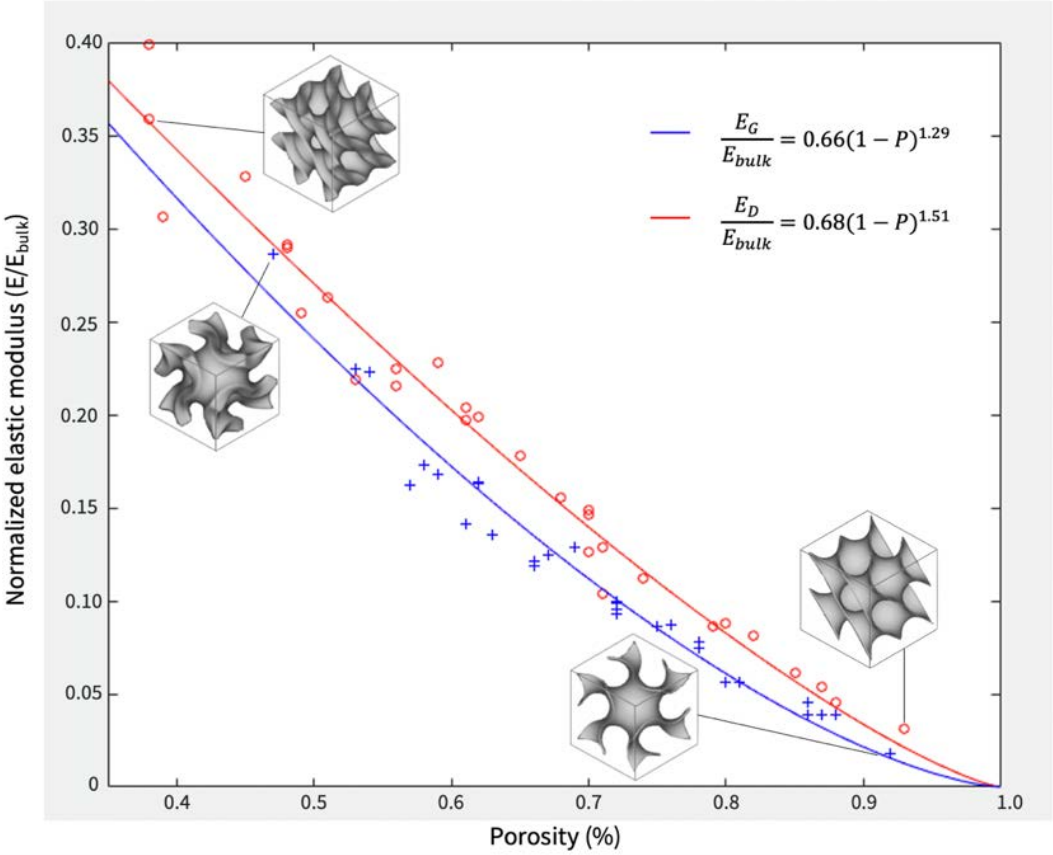

Figure 24. Scaling laws showing the relationship between the TPMS structure porosities and effective Young's modulus as predicted by the homogenization method. The red data denotes the diamond structure and blue denotes the gyroid.

Structure-Property Modeling

A second-degree polynomial was fit to the structure characteristic values (i.e., strut thickness, pore size, and normalized elastic modulus) for each geometry type, and the surface was overlaid with a plot of structure porosity. For both the gyroid and

diamond geometries, the effective elastic modulus generally increased with increasing strut thickness and decreasing pore size and porosity, with the modulus remaining relatively consistent along each porosity line. The structure-property plots are included in **Figure 25**.

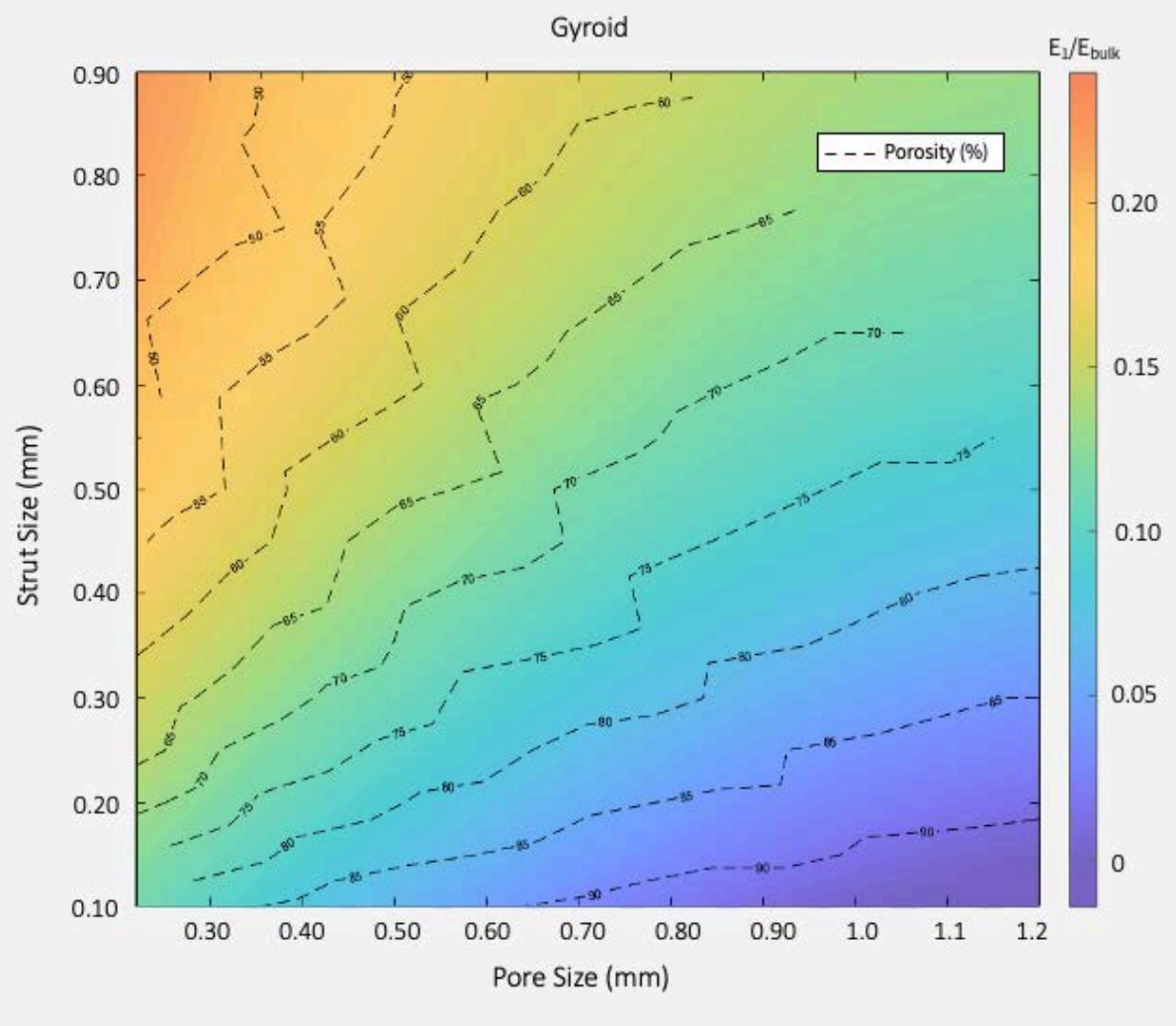

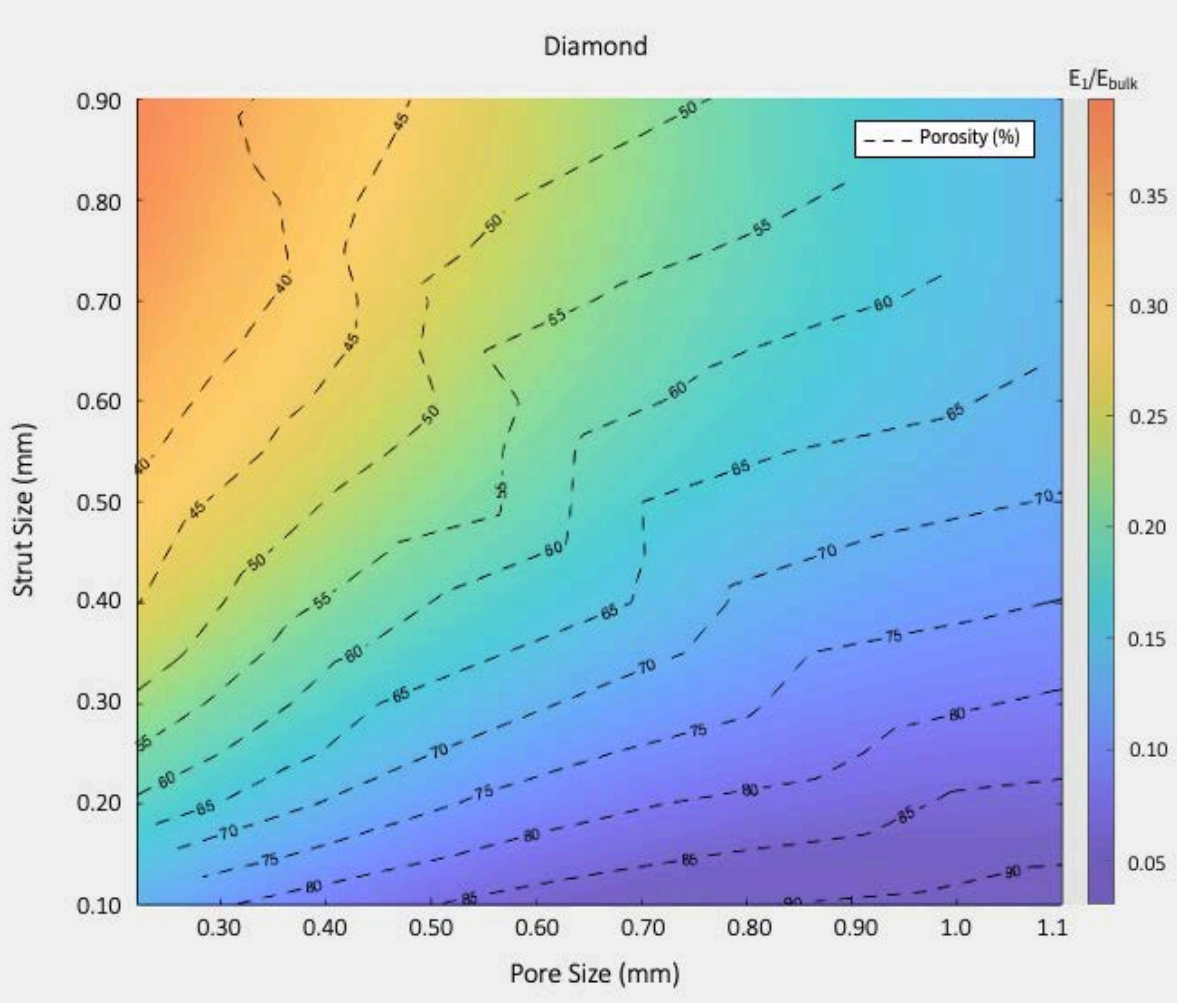

Figure 25. Structure-property models showing relationship between strut thickness, pore size, porosity, and normalized effective elastic modulus for the (top) gyroid and (bottom) diamond geometries. Note the difference in color bar values.

4.5 Discussion

For periodic materials used in medical applications, the basic repeating structure, and subsequently the mechanical response, can widely vary. As 3D printing continues to expand the possibilities for manufacturing complex geometries, understanding how the periodic material structure affects its mechanical properties is essential. In this study, a custom coding scheme was created to generate and assess TPMS-based structures, and maps of the interplay between TPMS type, approximation equation scaling factor, strut thickness, pore size, and porosity were provided. Families of unit cells were then modeled and used in a homogenization scheme to predict the elastic behavior of the structures, and relationships between the effective stiffness and structural properties were established. Ultimately, the resulting models help elucidate the interplay between architecture and function for 3D printed TPMS structures and can be useful for future design of porous materials for various applications including orthopaedic bone ingrowth.

Some limitations to the study should be noted. First, the investigation includes just two TPMS geometries, the gyroid and diamond, though many more are known. While alternative geometries, combinations of unit cell types, and functionally graded designs can provide a variety of desirable material properties [26, 47, 48], the gyroid and diamond represent two basic geometries that are both highly relevant to bone ingrowth and able to be reliably manufactured via FFF. Additionally, the general scheme presented in this study can be applied to a number

of different TPMS unit cell types for which the surface-approximating implicit functions are known. Second, this work focuses on sheet-based TPMS solids and does not examine the strut-based alternative, though their behaviors would most likely differ. However, existing studies have compared the two types of scaffolds at the same volume fraction and have demonstrated superior strength, greater elastic modulus, and better energy absorption capacity for sheet-based scaffolds [35, 47], therefore the sheet-based approach was chosen for the current work. Finally, elastic behavior characterization in this work is limited to determining Young's modulus and its relationship to structure porosity. While a variety of properties such as yield and fatigue strength are of course important for evaluating bone ingrowth materials, understanding how Young's modulus can be tuned is particularly useful in determining the suitability of porous PEEK for orthopaedic applications. Further, the homogenization technique described here provides an effective way to simplify future FE and more thorough mechanical behavior analyses for 3D printed devices incorporating TPMS structures.

In this study, the interplay between TPMS design parameters and resulting structural characteristics were explored for the gyroid and diamond geometries. The benefit of these models is to identify the values needed to achieve particular porous structure characteristics, which is a growing desire for researchers hoping to take advantage of TPMSs' unique properties. The ability to tune porous structure features is often highlighted as an important advantage for osseointegrative

biomaterials, with many studies investigating the optimal characteristics for achieving bone ingrowth [27, 33, 49]. While the current study does not include an exploration of optimal porous values, it provides a useful tool for such work. Similar tools have been developed for other non-TPMS structures, as exampled by a study from Arabnejad et al. in which design spaces for tetrahedral and octet truss unit cells are created [50]. In the study, the design spaces serve as a template for choosing and designing porous structures that are then created using SLM and tested mechanically and *in vivo*. Similarly, Xu et al. provides a recommended design space for optimized strut-based unit cells created via SLM [51]. For TPMSs, however, models are comparatively more limited and often consider only the outcome of porosity [49]. Vijayavenkataraman et al. posits that this is a result of studies focusing on controlling just one property of bone (e.g., density, permeability, strength) at a time and emphasizes the importance of considering multiple factors concurrently [49]. The study goes on to do just that using an optimization process, though a more generalized visualization of the design parameter interplay is not provided. Conversely, a more thorough exploration of how design parameters effect solid TPMS porous characteristics has been provided by Ambu and Morabito, though the study is specific to the Schwarz' Primitive geometry [16]. Notably, the authors reported that porosity has a greater dependence on thickness than scaling factor, similar to what was observed in the current study.

The structural properties of a porous material have a significant effect on the mechanical response, and the elastic behavior of the porous structures was therefore predicted. To this end, a homogenization approach was used to compute the effective elastic modulus for families of unit cells, like what has been performed for other periodic structures including natural bone [13, 26, 28, 30, 32, 33, 48, 52, 53]. One advantage of this process is the ability to readily predict the effective stiffness in each direction for the unit cell in order to assess anisotropy, with convenient visualization sometimes provided by 3D surface plots of Young's modulus [26, 52]. For native bone, this plot reflects a generally smooth distribution of Young's modulus without sharp protrusions or depressions, unlike what is typically found for many traditional strut-based structures [26, 33, 52, 54]. Importantly, this smooth distribution is similar to what has been reported in both the current research and other existing reports for TPMS structures [26, 33]. A study by Chen et al. explores both traditional lattice and TPMS-based geometries, noting more pronounced anisotropy for basic angular unit cells. The Young's modulus surfaces of the gyroid and diamond TPMSs appeared more rounded in shape with the gyroid surface appearing particularly sphere-like, similar to what was observed in the current study. The study by Chen et al. further explores how the unit cells can be manipulated and combined to change the degree of anisotropy, an important consideration for bone ingrowth materials [26, 53, 54]. Like other homogenization studies, the process in this study uses an isotropic base material so that resulting mechanical properties can be more easily attributed to the unit cell architecture and

not the base material properties. However, it should be noted that the degree of anisotropy and subsequent surface plots shapes can change accordingly with the base material properties (i.e., an orthotropic base material may result in varying amounts of protrusions between directions).

Following the characterization of TPMS design properties and the prediction of stiffness, the findings were combined into structure-property models for the gyroid and diamond geometries. Such models are found frequently in literature regarding porous biomaterials, often in the form of the Gibson-Ashby model [13, 27, 35, 43, 55]. To allow for comparison with these existing studies, the data was also fit to the scaling laws and the model coefficients, values that are not yet well-established for 3D printable porous structures [55], were reported. It was found that the predicted effective elastic modulus tended to decrease quadratically with increasing porosity, thus fitting well with the behavior proposed by Gibson and Ashby [43]. Modeling also showed similar elastic moduli between the gyroid and diamond geometries with the diamond achieving slightly greater stiffness, a finding that has been reflected elsewhere [26, 49, 53]. While the results generally agree well with previous findings, it is important to note that existing studies are somewhat limited in that they typically relate mechanical properties only to structure porosity [26, 35, 49, 53]. This focus on porosity is understandable as it is perhaps the most important architecture characteristic for determining porous structure behavior [13], a notion supported by the observation that predicted effective modulus remains relatively

consistent along each porosity line in **Figure 25.** However, successful bone ingrowth relies on multiple attributes. Pore size, for example, has been shown to have a significant impact on osseointegration throughout multiple stages of bone development, and different sizes are applicable for different functions [49, 50, 56]. Although it is useful to optimize a structural characteristic for a specific outcome, finding a balance between the multiple characteristics is essential. To this end, the models presented here provide a more comprehensive view of TPMS design property interplay and their relationship to stiffness. While the findings may be applicable to a range of materials, validation of the models will be carried out for FFF PEEK in the following chapter.

4.6 References

1. Lewallen, E.A., et al., Biological strategies for improved osseointegration and osteoinduction of porous metal orthopedic implants. Tissue Eng Part B Rev, 2015. **21**(2): p. 218-30.

2. Bobyn, J., et al., Characteristics of bone ingrowth and interface mechanics of a new porous tantalum biomaterial. The Journal of bone and joint surgery. British volume, 1999. **81**(5): p. 907-914.

3. Pałka, K. and R. Pokrowiecki, Porous Titanium implants: A review. Advanced Engineering Materials, 2018. **20**(5): p. 1700648.

4. Kienapfel, H., et al., Implant fixation by bone ingrowth. The Journal of arthroplasty, 1999. **14**(3): p. 355-368.

5. Bhattarai, S.R., et al., Novel production method and in-vitro cell compatibility of porous Ti-6Al-4V alloy disk for hard tissue engineering. J Biomed Mater Res A, 2008. **86**(2): p. 289-99.

6. Malahias, M.-A., et al., Highly porous titanium acetabular components in primary and revision total hip arthroplasty: a systematic review. The Journal of Arthroplasty, 2020. **35**(6): p. 1737-1749.

7. Trevisan, F., et al., Additive manufacturing of titanium alloys in the biomedical field: processes, properties and applications. Journal of applied biomaterials & functional materials, 2018. **16**(2): p. 57-67.

8. Castagnini, F., et al., Highly porous titanium cup in cementless total hip arthroplasty: registry results at eight years. International orthopaedics, 2019. **43**(8): p. 1815-1821.

9. Wong, K.C., 3D-printed patient-specific applications in orthopedics. Orthopedic research and reviews, 2016. **8**: p. 57.

10. Arce, K., et al., Developing a Point-of-Care Manufacturing Program for Craniomaxillofacial Surgery. Atlas of the Oral and Maxillofacial Surgery Clinics of North America, 2020. **28**(2): p. 165-179.

11. Teo, A.Q.A., et al., Point-of-Care 3D Printing: A Feasibility Study of Using 3D Printing for Orthopaedic Trauma. Injury, 2021.

12. Bhate, D., et al., Classification and selection of cellular materials in mechanical design: Engineering and biomimetic approaches. Designs, 2019. **3**(1): p. 19.

13. Nguyen, C.H.P., Y. Kim, and Y. Choi, Design for additive manufacturing of functionally graded lattice structures: a design method with process induced anisotropy consideration. International Journal of Precision Engineering and Manufacturing-Green Technology, 2019: p. 1-17.

14. Yuan, L., S. Ding, and C. Wen, Additive manufacturing technology for porous metal implant applications and triple minimal surface structures: A review. Bioactive Materials, 2019. **4**: p. 56-70.

15. Vijayavenkataraman, S., L.Y. Kuan, and W.F. Lu, 3D-printed ceramic triply periodic minimal surface structures for design of functionally graded bone implants. Materials & Design, 2020: p. 108602.

16. Ambu, R. and A.E. Morabito, Modeling, assessment, and design of porous cells based on schwartz primitive surface for bone scaffolds. The Scientific World Journal, 2019. **2019**.

17. Schoen, A.H., *Infinite periodic minimal surfaces without self-intersections*. 1970: National Aeronautics and Space Administration.

18. Guo, X., et al., *Mechanical behavior of TPMS-based scaffolds: a comparison between minimal surfaces and their lattice structures.* SN Applied Sciences, 2019. **1**(10): p. 1-11.

19. Li, L., et al., *Early osteointegration evaluation of porous Ti6Al4V scaffolds designed based on triply periodic minimal surface models.* J Orthop Translat, 2019. **19**: p. 94-105.

20. Ma, S., et al., *Manufacturability, mechanical properties, mass-transport properties and biocompatibility of triply periodic minimal surface (TPMS) porous scaffolds fabricated by selective laser melting.* Materials & Design, 2020. **195**: p. 109034.

21. Yavari, S.A., et al., *Layer by layer coating for bio-functionalization of additively manufactured meta-biomaterials.* Additive Manufacturing, 2020. **32**: p. 100991.

22. Liao, B., et al., *3D-Printed Ti6Al4V Scaffolds with Graded Triply Periodic Minimal Surface Structure for Bone Tissue Engineering.* Journal of Materials Engineering and Performance, 2021: p. 1-12.

23. Maskery, I., et al., *Effective design and simulation of surface-based lattice structures featuring volume fraction and cell type grading.* Materials & Design, 2018. **155**: p. 220-232.

24. Von Schnering, H. and R. Nesper, *Nodal surfaces of Fourier series: fundamental invariants of structured matter.* Zeitschrift für Physik B Condensed Matter, 1991. **83**(3): p. 407-412.

25. Herrera, A., et al., *Computational study and experimental validation of porous structures fabricated by electron beam melting: A challenge to avoid stress shielding*. Materials Science and Engineering: C, 2014. **45**: p. 89-93.

26. Chen, Z., et al., *On hybrid cellular materials based on triply periodic minimal surfaces with extreme mechanical properties.* Materials & Design, 2019. **183**: p. 108109.

27. Li, D., et al., *Design and optimization of graded cellular structures with triply periodic level surface-based topological shapes.* Journal of Mechanical Design, 2019. **141**(7).

28. Arabnejad, S. and D. Pasini, *Mechanical properties of lattice materials via asymptotic homogenization and comparison with alternative homogenization methods.* International Journal of Mechanical Sciences, 2013. **77**: p. 249-262.

29. Hollister, S.J. and N. Kikuchi, *A comparison of homogenization and standard mechanics analyses for periodic porous composites.* Computational mechanics, 1992. **10**(2): p. 73-95.

30. Hollister, S.J., J. Brennan, and N. Kikuchi, *A homogenization sampling procedure for calculating trabecular bone effective stiffness and tissue level stress.* Journal of biomechanics, 1994. **27**(4): p. 433-444.

31. Majumdar, S. and B.K. Bay, *Noninvasive assessment of trabecular bone architecture and the competence of bone*. Vol. 496. 2012: Springer Science & Business Media.

32. Fang, Z., et al., *Homogenization of heterogeneous tissue scaffold: A comparison of mechanics, asymptotic homogenization, and finite element approach.* Applied Bionics and Biomechanics, 2005. **2**(1): p. 17-29.

33. Li, D., et al., *Optimal design and modeling of gyroid-based functionally graded cellular structures for additive manufacturing.* Computer-Aided Design, 2018. **104**: p. 87-99.

34. Liu, F., et al., *Functionally graded porous scaffolds in multiple patterns: New design method, physical and mechanical properties.* Materials & Design, 2018. **160**: p. 849-860.

35. Al-Ketan, O., R.K.A. Al-Rub, and R. Rowshan, *Mechanical properties of a new type of architected interpenetrating phase composite materials.* Advanced Materials Technologies, 2017. **2**(2): p. 1600235.

36. Kapfer, S.C., et al., *Minimal surface scaffold designs for tissue engineering.* Biomaterials, 2011. **32**(29): p. 6875-82.

37. Kanit, T., et al., *Determination of the size of the representative volume element for random composites: statistical and numerical approach.* International Journal of solids and structures, 2003. **40**(13-14): p. 3647-3679.

38. Hassani, B. and E. Hinton, *A review of homogenization and topology optimization I—homogenization theory for media with periodic structure.* Computers & Structures, 1998. **69**(6): p. 707-717.

39. Abad, E.M.K., S.A. Khanoki, and D. Pasini, *Fatigue design of lattice materials via computational mechanics: Application to lattices with smooth transitions in cell geometry.* International journal of fatigue, 2013. **47**: p. 126-136.

40. Andreassen, E. and C.S. Andreasen, *How to determine composite material properties using numerical homogenization.* Computational Materials Science, 2014. **83**: p. 488-495.

41. Guedes, J. and N. Kikuchi, *Preprocessing and postprocessing for materials based on the homogenization method with adaptive finite element methods.* Computer methods in applied mechanics and engineering, 1990. **83**(2): p. 143-198.

42. Hollister, S.J., et al., *Application of homogenization theory to the study of trabecular bone mechanics.* Journal of biomechanics, 1991. **24**(9): p. 825-839.

43. Gibson, L.J. and M.F. Ashby, *Cellular solids: structure and properties*. 1999: Cambridge university press.

44. Spece, H., et al., *3D printed porous PEEK created via fused filament fabrication for osteoconductive orthopaedic surfaces.* Journal of the Mechanical Behavior of Biomedical Materials, 2020. **109**: p. 103850.

45. Parkinson, I.H. and N.L. Fazzalari, *Interrelationships between structural parameters of cancellous bone reveal accelerated structural change at low bone volume.* Journal of Bone and Mineral Research, 2003. **18**(12): p. 2200-2205.

46. Liu, X.S., et al., *Complete volumetric decomposition of individual trabecular plates and rods and its morphological correlations with anisotropic elastic moduli in human trabecular bone.* Journal of Bone and Mineral Research, 2008. **23**(2): p. 223-235.

47. Li, D., et al., *Comparison of mechanical properties and energy absorption of sheet-based and strut-based gyroid cellular structures with graded densities.* Materials, 2019. **12**(13): p. 2183.

48. Strömberg, N., *Optimal grading of TPMS-based lattice structures with transversely isotropic elastic bulk properties.* Engineering Optimization, 2020: p. 1-13.

49. Vijayavenkataraman, S., et al., *Triply periodic minimal surfaces sheet scaffolds for tissue engineering applications: An optimization approach toward biomimetic scaffold design.* ACS Applied Bio Materials, 2018. **1**(2): p. 259-269.

50. Arabnejad, S., et al., *High-strength porous biomaterials for bone replacement: A strategy to assess the interplay between cell morphology, mechanical properties, bone ingrowth and manufacturing constraints.* Acta biomaterialia, 2016. **30**: p. 345-356.

51. Xu, Y., et al., *Study on topology optimization design, manufacturability, and performance evaluation of Ti-6Al-4V porous structures fabricated by selective laser melting (SLM).* Materials, 2017. **10**(9): p. 1048.

52. Xu, S., et al., *Design of lattice structures with controlled anisotropy.* Materials & Design, 2016. **93**: p. 443-447.

53. Lu, Y., et al., *The anisotropic elastic behavior of the widely-used triply-periodic minimal surface based scaffolds.* Journal of the mechanical behavior of biomedical materials, 2019. **99**: p. 56-65.

54. Kang, J., et al., *Anisotropy characteristics of microstructures for bone substitutes and porous implants with application of additive manufacturing in orthopaedic.* Materials & Design, 2020. **191**: p. 108608.

55. Maskery, I., et al., *Insights into the mechanical properties of several triply periodic minimal surface lattice structures made by polymer additive manufacturing.* Polymer, 2018. **152**: p. 62-71.

56. Karageorgiou, V. and D. Kaplan, *Porosity of 3D biomaterial scaffolds and osteogenesis.* Biomaterials, 2005. **26**(27): p. 5474-5491.

Chapter 5: Validation of FFF Porous PEEK Architecture-Property Model

5.1 Abstract

Additively manufactured materials designed from triply periodic minimal surfaces (TPMSs) have been receiving attention for their usefulness in numerous applications including orthopaedic implant fixation. Predictive models can be used to better understand the elastic behavior of these materials, though experimental validation of such models is needed to determine their efficacy. Most existing validated models are specific to laser-based forms of printing and metallic materials and are therefore not applicable to the fused filament fabrication (FFF) process being adopted by many hospitals. Thus, this study investigates the mechanical behavior of TPMS-inspired porous PEEK created via FFF to experimentally validate the diamond architecture-property model created in **Chapter 4**. Porous structures representing six different points on the diamond architecture plot were additively manufactured in two orientations. The porosities were determined using micro-computed tomography and the mass method, and compression testing was performed to determine structure yield strength and Young's modulus. Good agreement was found between the as-designed and printed structure architectures, with an average absolute error of 4.1% for porosity. The z-direction Young's modulus ranged from 289.7 to 557.5 MPa and yield strength ranged from 10.12 to 20.3 MPa. For the xy-direction, Young's modulus ranged from 133.8 to 416.4 MPa and yield strength ranged from 3.8 to 12.2 MPa. For each orientation, the mechanical

properties were found to decrease with increasing porosity, and failure occurred due to both strut bending and interlayer debonding. The mechanical properties predicted by the modeling in **Chapter 4** agreed with the values found for z-direction samples (difference 2 – 11%) but less so for xy-direction samples (difference 27 – 62%) due to weak interlayer bonding and print path irregularities. Ultimately, the results demonstrate the ability to achieve a variety of FFF porous PEEK with ranging mechanical properties and show promise for a predictive architecture-property model for PEEK TPMS structures.

5.2 Introduction

The incorporation of highly porous materials is an effective strategy for achieving implant osseointegration, and advancements in 3D printing have expanded the possibilities of their design and creation. Consequently, the current work explores the potential of TPMS-inspired PEEK implant surfaces created via fused filament fabrication. The architectural and mechanical properties of such a material must be investigated to determine its suitability as an osseointegrative surface, and establishing an accurate model of properties will be useful for the future design and inclusion of porous PEEK in patient-specific and point of care manufactured implants.

Experimental validation is a vital step in determining the efficacy of any design or modeling process. This is especially true for TPMS structures, as the AM methods

primarily used to create them have been associated with varying degrees of dimensional accuracy and anisotropy [1-4]. So far, simulations of TPMS structures suitable for bone ingrowth have been validated mostly for the laser and light-based forms of printing [1, 5-10]. One such study from Zheng et al. investigated structures with four different TPMS geometries [6]. The study considers how structure density relates to other topological and mechanical properties one at a time and establishes a scaling law for each. The compressive mechanical properties models were validating for polymer gyroid structures and the authors report good agreement between the theoretical and measured values, though anisotropy resulting from the structure architecture or print process was not explored [6]. For TPMS structures more relevant to orthopaedic applications, a study from Soro et al. models and tests Ti6Al4V scaffolds created using selective laser melting (SLM) [10]. In this study, the Schwartz primitive geometry comprised the porous structure, and a range of porosities were included. The results showed that differences between the designed and actual porosity values tended to increase with increasing porosity, and that yield strength and Young's modulus tended to decrease with increasing porosity [10]. The latter finding agrees with what has been found for other porous structures [11], though compression testing was performed only in one direction. The study reported good agreement between experimental and FE modeled properties, and importantly, it was found that small discrepancies between designed and actual porosity did not appear to influence the mechanical behavior [10].

Compared to what is reported for laser and light-based printing methods, a relatively small number of studies present and validate models for the properties of TPMS-based structures created by FFF [12]. Kladovasilakis et al. investigated the gyroid, diamond, and primitive TPMS geometries printed in polylactic acid (PLA) and reported acceptable dimensional accuracy. The elastic behavior predictions from FE models agreed well with experimental results, though consideration was only given to loading perpendicular to layer deposition [12]. Notably, this was the only found instance of FE methods used for TPMS structures created via FFF. While a study from de Aquino et al. does not include simulation of mechanical properties, it does provide insight into the effect of print orientation on elastic behavior for FFF samples [4]. This study considers gyroid, diamond, and primitive structures built with acrylonitrile butadiene styrene (ABS) and performs compression at both 0° and 90° with respect to the printing orientation. Unsurprisingly, decreases in strength for the 90° group were attributed to debonding between the material layers, but differing degrees of anisotropy were also reported for each geometry, with the interaction effects between geometry type and loading direction being greatest for the primitive and least for the gyroid [4]. While these results are helpful for understanding how FFF may be used to control porous structure stiffness, strength, and degree of anisotropy, similar studies for PEEK other high temperature polymers do not exist to the author's knowledge. Additionally, no mechanical properties have been found for PEEK TPMS regardless of manufacturing method.

Although many researchers have shared useful models for relating TPMS structure and mechanical properties, not all have experimentally validated their findings, and fewer have conducted testing for more than one printing orientation. In this study, the aim is to validate the structure-property model created for 3D printed porous PEEK in Aim 3, specifically for the diamond TPMS. Porous structures within the design space for bone ingrowth will be selected from the model and manufactured using fused filament fabrication, and a series of compression tests will be performed to determine the elastic properties for each. The effects of structure porosity and print orientation on the resulting mechanical performance will be assessed.

5.3 Methods

Porous PEEK Sample Printing

The diamond TPMS type was chosen for experimental validation based on Aim 1 findings that it exhibited the highest yield strength, Young's modulus, and preosteoblast cell activity compared to the gyroid. Six testing points on the diamond TPMS architecture-property plot were selected to represent a range of porous properties. To explore differences between elastic behavior due to porosity, four points with nominal porosities of 45%, 50%, 60%, and 70% and a similar pore size of approximately 500 μm were selected. Two more points along the 70% porosity line were also chosen to determine mechanical property differences between structures with similar porosity but differing pore and strut size (**Figure 26**).

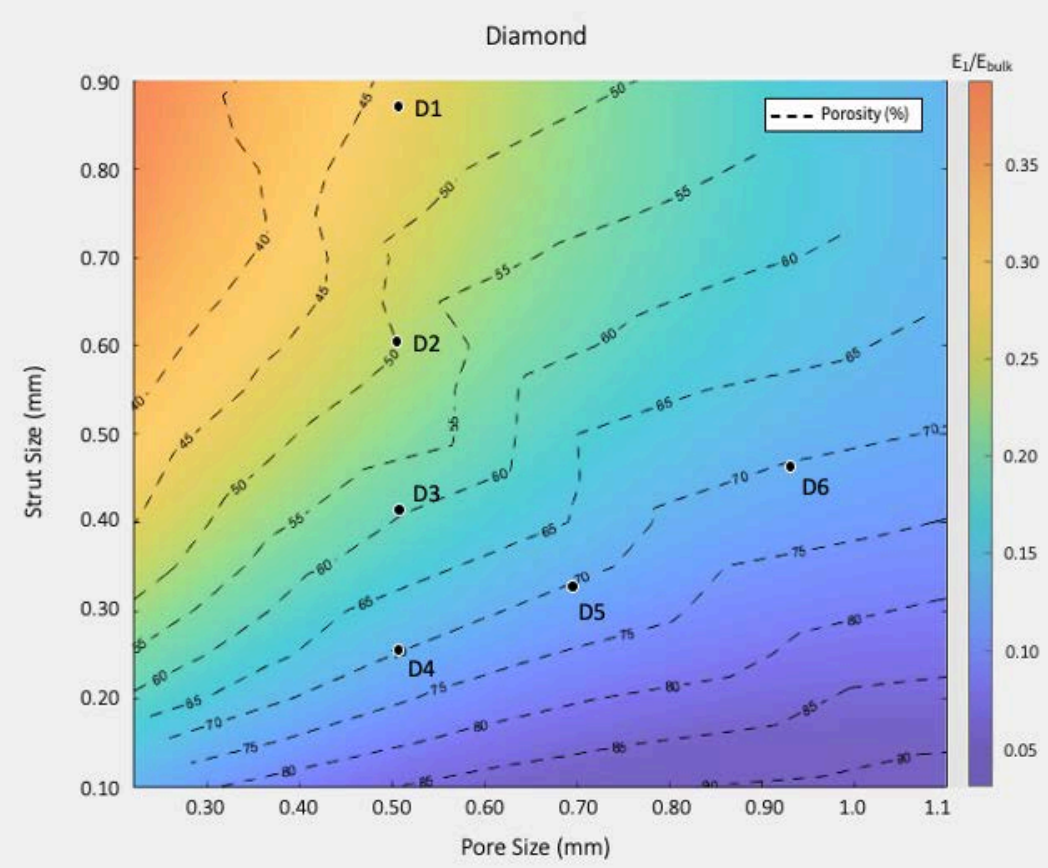

Figure 26. Points selected for validation testing from the diamond structure-function plot. Points were chosen to represent a range of different porosities, pore sizes, and strut sizes.

Porous structures corresponding to each testing point were designed as prisms with dimensions 12.7 x 12.7 x 25.4 mm, as recommended by ASTM D695 [13]. The TPMS models were created using MathMod-9.1 (open source, www.sourceforge.net) and 3ds Max (Autodesk, Inc., San Rafael, CA), and sliced for printing using Simplify3D software (Simplify3D, Cincinnati, OH). Four samples were printed for each point and in each orientation, with samples printed either laying sideways or standing

upright for determining the mechanical properties parallel and perpendicular to layer deposition direction, referred to as the xy and z-directions, respectively. Samples were additively manufactured from VESTAKEEP i4 PEEK filament (Evonik Industries AG, Essen, Germany) using a Kumovis HTRD 1.3 printer (Kumovis GmbH, Munich, Germany). Printing parameters remained consistent between the prints and matched the parameters used for the nonporous PEEK in Specific Aim 2 (**Table 3**).

Architecture Characterization

Following manufacturing, one samples of each testing point was imaged using micro-computed tomography (micro-CT) with a Scanco micro-CT 80 (Scanco Medical AG, Brüttisellen, Switzerland) at a maximum resolution of 0.0252 mm. A bone morphology module in AnalyzeDirect software (AnalyzeDirect, Stilwell, KS) was used to determine trabecular (i.e., strut) thickness, pore size, and porosity. Porosity was calculated as the ratio of void to total volume, and pore size was determined by measurement of spheres fitted into the porous structure. Porosity (P) was also determined for all samples using the mass method in which the sample mass (M) is measured by an electronic scale and the volume (V) measured by calipers [14]. Porosity can then be calculated using the equation

$$P = \left(1 - \frac{M}{V\rho}\right) * 100\ \%$$

where ρ is the density of the PEEK, taken as 1.35 g/cm^3.

Determination of Mechanical Properties

Compression testing was conducting according to ASTM D695 [13] and in accordance with ISO 17025 quality system requirements [15]. For each test, the prisms were oriented standing upright so that samples printed vertically were loaded perpendicular to the layer deposition direction and samples printed horizontally were loaded parallel to layer deposition. The testing was performed on a mechanical testing frame (MTS Criterion Model 43, MTS Systems, Eden Prairie, MN) with calibrated load and displacement sensors and lubricated platens at a displacement rate of 1.3 mm/min per ASTM D695 [16]. Stress-strain curves were generated from the data, and the modulus of elasticity and yield strength (taken as the 0.2% offset stress) were determined using the same custom script used in the preliminary mechanical testing portion of Aim 1 and the determination of solid PEEK properties in Aim 2.

Fracture Analysis

Following mechanical testing, the porous structures were imaged via scanning electron microscopy (SEM) using a Zeiss Supra 50VP SEM (Zeiss, Oberkochen, Germany) in order to help elucidate the fracture behavior. The samples were sputter coated with platinum-palladium alloy prior to imaging and micrographs were collected with a secondary electron detector.

Statistical Analysis

Sample size was determined via an a priori power analysis using a power of 0.80 and alpha value of 0.05. The effect size of 1.16 was determined using the data found in the mechanical testing portion of Aim 1. A sample size of n = 3 was determined, and an extra sample was added to each group to achieve n = 4. Differences in porosity determination method (micro-CT vs. mass method) were determined using paired t-tests with each tested sample representing a pair, and property differences between z and xy-directions were determined using paired t-tests with each architecture representing a pair. Correlation between the mechanical properties and porosity were evaluated using Pearson's correlation coefficient. For all analyses, SPSS Statistics 26 (IBM, Armonk, NY) was used, and significant was determined at an alpha value of 0.05.

5.4 Results

Porous Sample Printing and Architecture Characterization

Eight samples, four oriented vertically and four horizontally, were successfully printed for each of the representative architectures (**Figure 27**). A statistical difference in porosity values between the micro-CT and mass method of determination was observed ($p < 0.01$), though the average error between the two measurements was relatively small at 3.3 %. The results of both methods along with the strut and pore size micro-CT analysis are provided in **Table 5**. In general, good

agreement between the as-designed and measured values was found. With the exception of one measurement (D1_z strut thickness), the difference between the designed and actual strut thickness and pore size values were within 0.2 mm, the diameter of the nozzle used for 3D printing. The average absolute error between designed and actual strut thickness and pore size were 116 μm and 82 μm, respectively. For porosity, absolute error between the designed and actual mean values (determined by mass method) ranged from 0.1% to 8.5 %, with an average of 4.1 %.

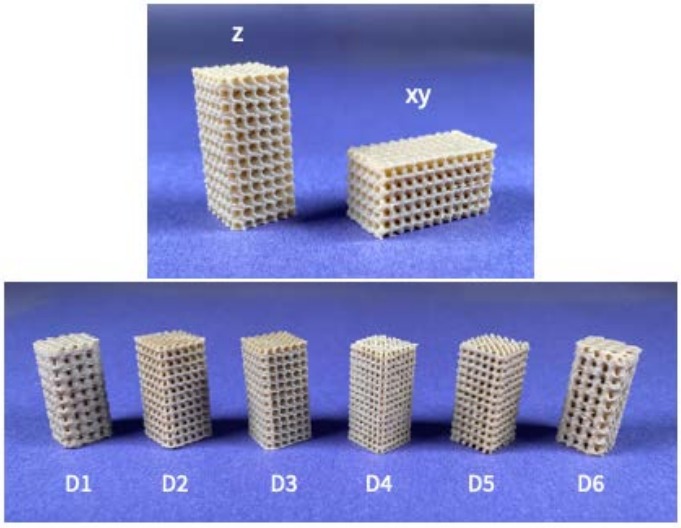

Figure 27. Porous diamond samples printed for compression testing. (Top) The same porous geometry printed vertically and horizontally to allow for compression testing parallel and perpendicular to print layer direction. (Bottom) Samples corresponding to the six points selected on the structure-function model.

Table 5. Architecture characteristics (i.e., strut size, pore size, and porosity) for structures D1-D6, printed both vertically and horizontally, as determined by microCT and mass method.

	Strut Thickness (mm)			**Pore Size (mm)**			**Porosity (%)**			
Architecture	As designed	µCT measured mean ± SD (n = 1)	Difference	As designed	µCT measured mean ± SD (n=1)	Difference	As designed	µCT measured (n = 1)	Mass method mean ± SD	Difference (designed to mass method)
D1_z	0.880	0.552 ± 0.305	-0.328	0.498	0.687 ± 0.497	0.189	45.8	42.3	48.7 ± 5.8	3.0
D1_xy		0.656 ± 0.212	-0.224		0.548 ± 0.424	0.050		45.8	50.2 ± 0.4	4.5
D2_z	0.600	0.532 ± 0.242	-0.069	0.485	0.540 ± 0.333	0.054	49.4	42.7	49.5 ± 3.2	0.1
D2_xy		0.534 ±0.213	-0.067		0.635 ± 0.373	0.150		50.1	57.8 ± 2.6	8.5
D3_z	0.425	0.557 ± 0.326	0.132	0.493	0.554 ± 0.359	0.062	58.6	54.7	54.7 ± 1.2	-3.9
D3_xy		0.435 ± 0.160	0.010		0.594 ± 0.329	0.102		62.3	63.2 ± 1.7	4.6
D4_z	0.260	0.436 ± 0.179	0.176	0.493	0.568 ± 0.365	0.075	69.1	61.6	60.7 ± 4.3	-8.4
D4_xy		0.331 ± 0.118	0.071		0.598 ± 0.312	0.105		66.7	65.2 ± 4.3	-4.0
D5_z	0.325	0.445 ± 0.190	0.120	0.680	0.657 ± 0.376	-0.022	70.6	62.5	64.9 ± 2.8	-5.7
D5_xy		0.463 ± 0.157	0.138		0.690 ± 0.349	0.010		60.0	65.3 ± 0.9	-5.3
D6_z	0.450	0.475 ± 0.141	0.025	0.939	0.974 ± 0.715	0.035	71.0	66.9	70.1 ± 0.9	-0.9
D6_xy		0.414 ± 0.126	-0.036		1.073 ± 0.707	0.135		71.9	71.2 ± 1.0	0.2

Despite good agreement between the measured characteristics, examination of the micro-CT renderings showed a considerable qualitative difference in the structures printed vertically vs. horizontally. This difference results from the printing process, in which the same geometry is formed differently depending on printing direction. Small voids between layer deposits further contribute to the irregularities seen. The resulting differences are explained further in **Figure 28**, which includes two toolpaths of the same geometry.

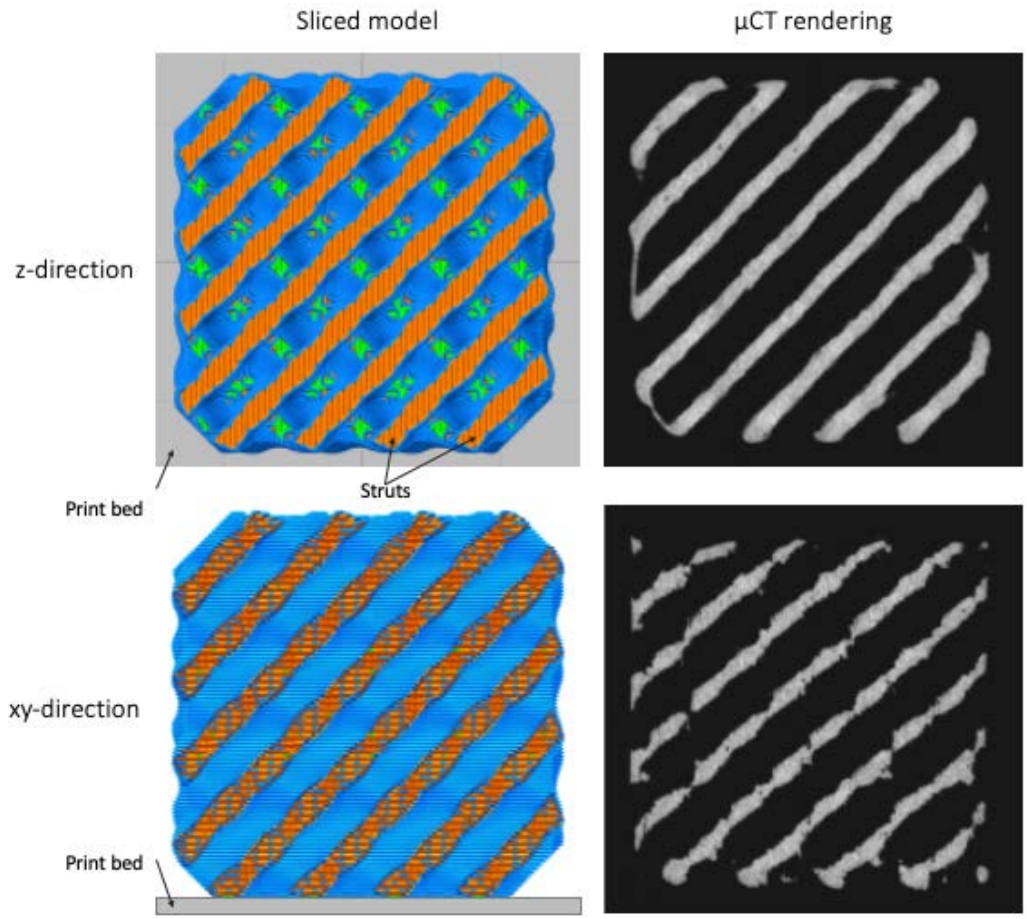

Figure 28. Loading surface of porous samples created either standing vertically or laying horizontally, with the print bed shown in gray. The geometry is the same prior to slicing, and the images on the left show the print path post-slicing. In the vertical orientation (top), the row of struts is created by continuous filament deposits, resulting in a smooth and accurate geometry. In the horizontal direction, the row of struts is instead built from successive layers, causing irregularities in the geometry.

Determination of Material Properties

The stress-strain plots resulting from compression testing are shown in **Figure 29**, with each plot containing both the xy and z loading orientations for a given architecture. Short toe regions prior to the linear elastic region were observed in some samples, but these regions were excluded from calculations for the Young's modulus. For the z-direction, the curves followed a similar behavior to those presented in **Chapter 2**, with a linear-elastic region followed by a plateau and increase in stress as the material is compressed post-yield. This behavior is typical of porous structures which exhibit bending-dominated behavior [17, 18]. For the xy-direction, the linear-elastic regions were generally followed by a decrease in as material layer splitting occurred under compression.

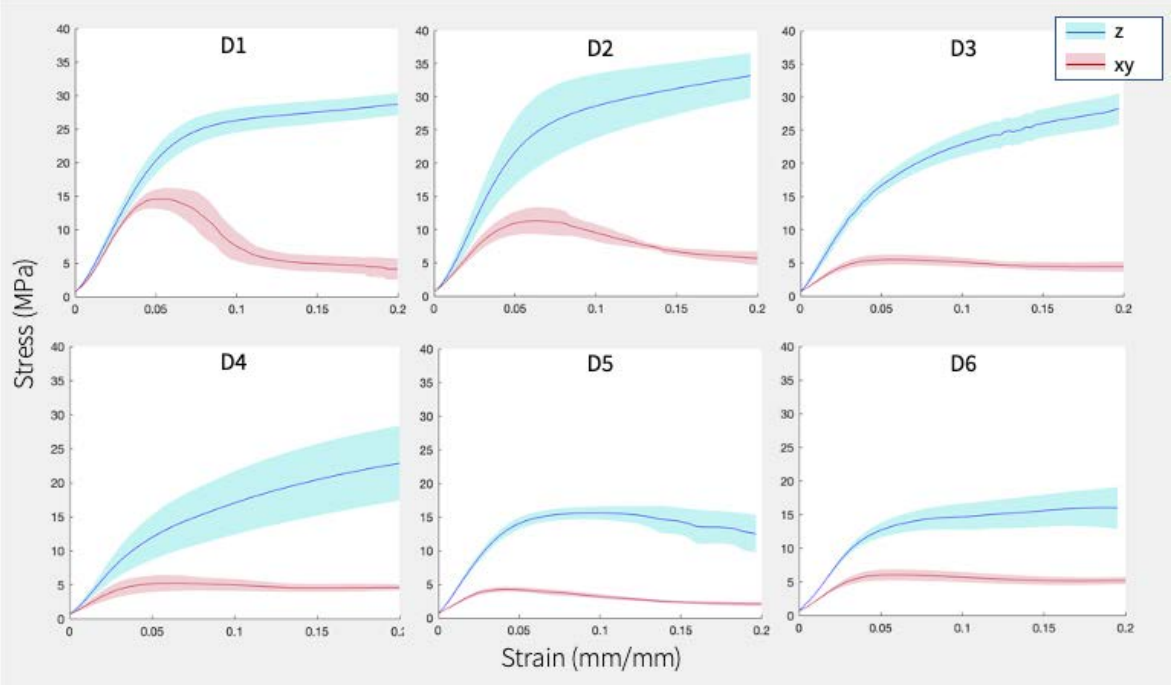

Figure 29. Stress-strain curves for the six architectures loaded in the 0° and 90° orientations with respect to print direction.

For each architecture, significantly greater properties (**Table 6**) were achieved for the z direction than the xy-direction (elastic moduli: $p < 0.001$; yield strength: $p < 0.001$). For z-direction samples, Young's modulus ranged from 289.7 to 557.5 MPa and yield strength ranged from 10.1 to 20.3 MPa. For the xy-direction, Young's modulus ranged from 133.8 to 416.4 MPa and yield strength ranged from 3.8 to 12.2 MPa. For each orientation, the mechanical properties were found to decrease with increasing porosity. For the xy-direction, strong negative correlations were found between porosity and elastic modulus ($r = -0.948$, $p < 0.001$) and porosity and yield

strength ($r = -0.943$, $p < 0.001$). Similar relationships were also observed for the z-direction porosity and modulus ($r = -0.775$, $p < 0.001$), as well as for porosity and yield strength ($r = -.681$, $p < 0.001$).

Normalized Young's modulus was calculated for each sample by dividing the measured modulus by the modulus of the constituent material (solid PEEK studied in Chapter 3). The z and xy-direction samples were normalized by the solid PEEK modulus determined via loading perpendicular and parallel to layer deposition, respectively. **Table 6** shows these values along with the normalized moduli predicted by homogenization in **Chapter 4**. The percent difference ranged from 2.0 to 11.0 % for the z-direction and 27.5 to 62.3 % for the xy-direction.

Table 6. Compressive properties of porous PEEK architectures and comparison with predicted values from Chapter 4 modeling.

Sample	Young's modulus (MPa)	Yield strength (MPa)	Normalized Young's modulus (experimental)	Normalized Young's modulus (model)	% difference
D1_z	557.5 ± 42.6	20.3 ± 2.1	0.238	0.261	8.91
D1_xy	416.5 ± 8.4	12.2 ± 1.3	0.189		27.47
D2_z	492.2 ± 85.4	20.3 ± 5.6	0.210	0.234	10.30
D2_xy	283.9 ± 46.6	9.1 ± 1.4	0.129		44.86
D3_z	423.7 ± 27.6	12.7 ± 0.3	0.181	0.203	10.98
D3_xy	168.6 ± 26.6	4.6 ± 0.6	0.077		62.26
D4_z	289.7 ± 73.5	10.1 ± 3.5	0.139	0.142	1.99
D4_xy	137.4 ± 42.2	4.3 ± 1.2	0.062		56.02
D5_z	329.2 ± 27.1	11.2 ± 0.7	0.140	0.146	3.83
D5_xy	160.4 ± 22.1	5.1 ± 0.7	0.073		50.07

D6_z	325.9 ±25.1	12.5 ± 1.4	0.139	0.130	6.92
D6_xy	133.8 ± 16.3	3.8 ± 0.4	0.061		53.22

Fracture Analysis

The main failure modes observed for the porous structures depended greatly on the loading orientation. Examples of loading in each direction up to 20% strain is provided in **Figure 30**.

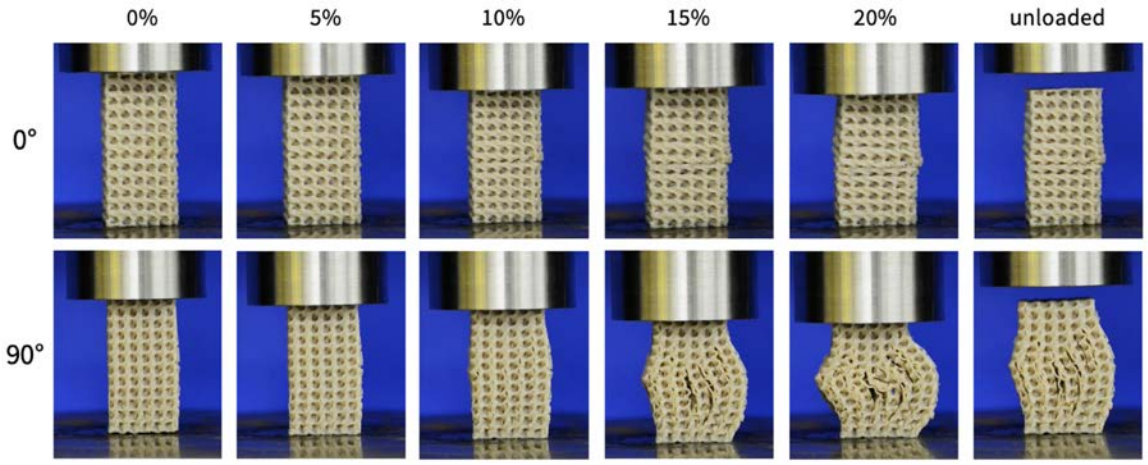

Figure 30. Stages of compression from 0 to 20% strain for z-direction samples (top) and xy-direction (bottom).

When loaded perpendicular to the layer deposition direction (z-direction), structures tended to fail by strut bending in roughly the thinnest section of the strut and layer-by-layer buckling was apparent (**Figure 31**). This behavior, along with the appearance of the stress-strain curves, points to bending-dominated deformation for these structures.

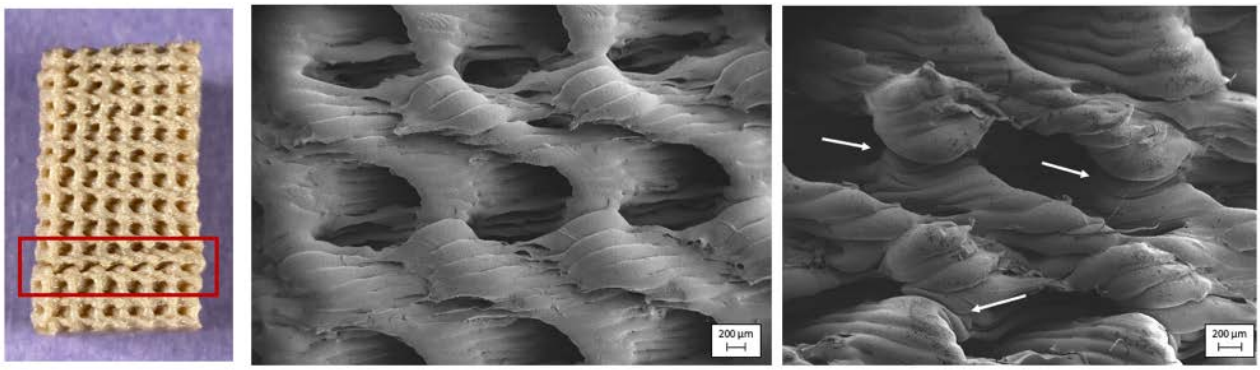

Figure 31. Strut bending resulting from compression of z-direction samples.

Samples loaded parallel to layer direction (xy-direction) underwent more catastrophic failure, and cracking resulting from layer debonding was the dominate failure mode. In many cases, small areas of layer debonding became apparent around 5 – 10% strain and occurred diagonally (**Figure 32**). Cracks propagated from the areas of debonding and increased under increasing deformation, often causing a bulging effect. In some cases, this bulging also led to the stretching and breaking of other filament deposits (**Figure 33**).

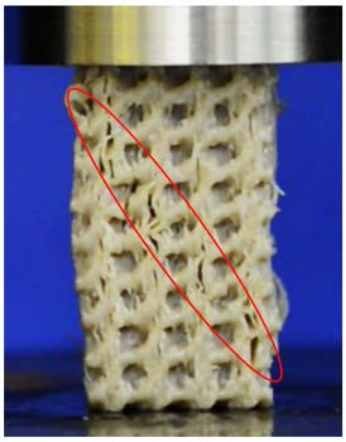

Figure 32. Layer splitting origins occurring at a 45° angle.

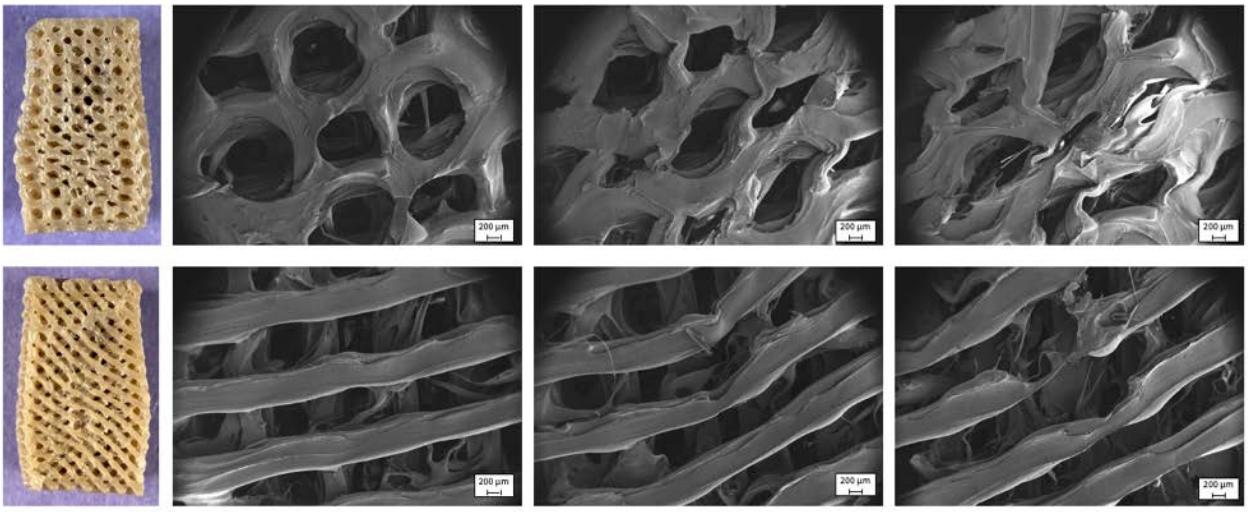

Figure 33. SEM image of xy-direction samples after being compressed to failure.

5.5 Discussion

AM materials designed from triply periodic minimal surfaces are gaining attention for their potential usefulness as orthopaedic osseointegrative materials. Predictive models can help in the design of these materials, though experimental validation of

such models is necessary to determine their efficacy. The purpose of this work was to validate the **Chapter 4** model relating TPMS architecture and mechanical response. A range of diamond TPMS-based porous PEEK structures were additively manufactured and tested in compression to characterize their elastic behavior. Large differences were found in elastic modulus and yield stress due to print orientation, and the z-direction failure appeared to be bending-dominated while xy-direction failure resulted from layer splitting. Good agreement was observed between the modeled and experimental values for the z-direction but not the xy-direction, due to irregularities resulting from the 3D printing process. Ultimately, the results reported here help elucidate the elastic behavior of FFF-printed TPMS PEEK and show promise for the related architecture-property model.

This study had some limitations. First, the architecture-property model created in **Chapter 4** was validated only for a single TPMS type and material, diamond and PEEK, respectively. Of course, a wide range of elastic behaviors could be achieved using alternative geometries and 3D printed materials, and future work will help determine which structures are optimal for a given application. Second, the mechanical testing was carried out on dry PEEK specimens at room temperature, and testing under more physiological conditions would better elucidate the performance of porous PEEK once implanted. Similarly, testing was conducted only in compression, while various stress states are involved in load-bearing orthopaedic applications. Nevertheless, establishing the properties under the current conditions

provides an initial characterization of the material unrelated to specific use cases and allows for comparison with existing porous materials, which are often tested in a similar manner. Finally, this study did not involve optimization of printing parameters to improve mechanical properties and layer bonding, and the ability to draw conclusions about the full range of achievable TPMS porous PEEK properties is therefore limited. Future work including parameter optimization may result in the achievement of greater yield stress and stronger interlayer bonding, the latter having significant impacts on structure anisotropy and model accuracy.

In this study, the architectural characteristics of the porous PEEK sample were assessed and compared to as-design values, and relatively small differences were observed. The current results were similar to some existing reports of dimensional accuracy for TPMS structures creating using laser based or FFF printing. For SLS and EBM, a number of studies have created TPMS structures using materials relevant to orthopaedics, including stainless steel and titanium alloy, and have reported generally good reproducibility [2, 7, 9, 10, 19-21]. However, differences between intended and actual porosity of up to 50% have been reported [10], and discrepancies are often attributed to adhesion of unsintered powder and to the "staircase effect" in which stacked layers form a stepwise structure at angled or rounded features [19, 20]. There are fewer findings related to dimensional accuracy for TPMS created by FFF but results are promising [18, 22, 23], with some studies reporting actual porosities within 10% of the designed value similar to what was

found in the current study [12, 24]. Defects in FFF prints may arise from sources like nozzle clogging and air bubbles within the material, and other discrepancies may result from toolpath errors, a large nozzle diameter relative to the feature size, gaps between extruded layers, or the staircase effect on certain features [18, 25]. The self-supporting nature of the porous structures may also contribute to error, especially in pore size, because extruded material can deform as it slowly solidifies in the heated chamber [18]. Although a combination of these factors may have led to the small dimensional discrepancies seen in this study, the porous properties were well within range for cancellous bone [26], and it was shown that the FFF process affords great control over porous PEEK for a range of architectural characteristics.

After assessing the morphology of the PEEK TPMS structures, compression testing was conducted to determine the mechanical properties. Though there are no existing studies of TPMS-inspired PEEK available for comparison, a few previous studies have examined porous PEEK created via FFF and found properties similar to those reported for the xy-direction samples in the current study [27-29]. One of the earliest reports comes from Vaezi and Yang, who tested FFF closed-cell porous samples with 38% rectilinear porosity and found a compressive yield strength (calculated as true stress) of 29 MPa [27]. Feng et al. similarly tested FFF rectilinear lattice samples and reported ultimate compressive strength and elastic modulus ranging from 31 to 60 MPa and 231 to 368 MPa, respectively, though yield strength was not reported [28]. Structure porosity in the study was roughly 60% with pore

sizes between 260 and 556 μm. Finally, Su et al. reported a compressive strength and modulus of rectilinear PEEK of 23 and 397 MPa, though samples which underwent post-printing annealing had increased values of 36 and 575 MPa [29]. Slightly lower values were observed for samples that underwent sulfonation after annealing to induce microporosity. For SLS, porous structures have demonstrated compressive strengths ranging from 10.1 to 51 MPa, though PEEK composite materials were used in these studies [30]. For non-additive methods, fully porous PEEK has shown generally lower mechanical properties with compressive yield strength below 10 MPa and elastic moduli below 200 MPa [31-33]. Such findings are similar to what was observed for the xy-direction samples in the current study, which are also comparable to what has been reported for trabecular bone [34].

It is well-accepted that the strength and elastic modulus of porous structures tend to decrease with increasing porosity [11], and the current findings show this relationship as expected for FFF porous PEEK. Similar findings have been reported for TPMS based structures composed of other AM materials [2, 17, 35-38]. Perhaps more importantly, the current results confirm that a range of porosities and pore sizes can be achieved for FFF porous PEEK, allowing for the tuning of mechanical properties. Manipulating structure stiffness through porosity and enhancing bone formation through pore size are popular strategies for osseointegrative biomaterials. This is because porosity allows for increase permeability and the reduction of biomechanical mismatch between the implant and surrounding bone,

a cause of stress shielding and stunted or irregular bone remodeling [39], while pore size can effect bone growth at multiple stages [40, 41]. Extensive efforts to identify the optimal porosity and pore size for osseointegrative materials have shown that recommended values vary depending on function. For example, smaller pores may lead to increased cell migration, differentiation, and structure strength, while larger pores allow for vascularization and tissue ingrowth [28, 40, 41]. Thus, many researchers are combining the positive attributes of multiple pore sizes though functional porosity grading, which can be easily achieved for the equation-based TPMS designs [42, 43]. Functional TPMS grading can provide improved control over structure characteristics like mechanical behavior, energy absorption, and scaffold degradability [5, 42-44], and though the structure porosities in the current study are not graded, the findings may be helpful for future creations of functionally graded FFF porous PEEK.

In addition to porosity, mechanical properties are also affected by loading direction due to anisotropy induced by geometrical features or manufacturing method. TPMS structures are generally considered anisotropic, but the gyroid and diamond show equivalent elastic moduli in each principal direction due cubic symmetry [45], a concept reflected in the **Chapter 4** findings. Additive manufacturing, on the other hand, tends to result in transversely isotropic properties [3, 22, 46, 47]. A study by de Aquino et al. considers the impact of both geometry and manufacturing process on TPMS structures created using low temperature FFF [4]. The study considers

compressive properties for 0º and 90º loading orientations (perpendicular and parallel to layers, respectively) and reports a decrease in stiffness and strength for 90º oriented gyroid and diamond samples due to layer debonding, with similar findings reported elsewhere [22]. Interestingly, the study also reports that the interaction effect of scaffold geometry and loading direction was least for the gyroid and greatest for the primitive type TPMS, with the expected process-induced anisotropy nearly eliminated, showing that anisotropy can be increased or decreased by modification of the scaffold geometry [4]. In the current study, results also showed a decrease in stiffness and strength for xy-direction samples due to layer debonding, though to a greater extent than what has been seen for low temperature materials [4, 22]. The degree of anisotropy was also much greater than what was observed for solid PEEK in **Chapter 3**. The large difference is suspected to be a result of the printing process toolpath, which, even for the same geometry, is different depending on structure orientation. This notion is supported by the micro-CT images which show significantly more print irregularities for a surface comprising many layers, as opposed to a single layer.

Loading direction also corresponded with differences in failure modes under compression. The z-direction exhibited struts failing in a manner suggesting bending-dominated deformation. This behavior is consistent with existing reports for diamond TPMS structures [17, 48] and is related to greater energy absorption capacity than stretch-dominated architectures [49]. The dominate failure mode for

the xy-direction was debonding of the print layers, as observed in previous FFF studies. Like what was observed for solid PEEK in Chapter 3, splitting tended to occur directly at the interface between two layers. While these findings point to weak layer bonding, it is important to note that the printing parameters in the current study were selected because they allow for the creation of fine features for an array of different architectures. Future studies may aim to improve interlayer bonding for a given architecture by optimizing parameters such as chamber temperature, printing speed, and local cooling conditions.

In this study, a comparison was made between the measured mechanical properties and those predicted by the homogenization method detailed in **Chapter 4,** and the difference was found to be between 2% and 12% for the z-direction and between 27% and 62% for the xy-direction. Existing models created to predict the mechanical properties of AM porous structures also show a range of agreement with experimental results [21, 50-53]. Similar to the current study, Castro et al. predicted the elastic properties of TPMS structures using asymptotic homogenization [50]. Validation was performed using MultiJet printed polymer samples, and the difference between the predicted and actual Young's modulus ranged from 2% to 8% for values measured by the testing machine arm and 2% to 19% for those measured by video extensometer. The authors identify potential sources of bias as unremoved support material within the pores and differences between design and actual porosity [50]. Other homogenization validations come from Cheng et al., who

report excellent agreement with predicted properties for laser sintered cubic scaffolds [52], and from Nasirov and Fidan who report values similar to their model (< 10% difference) for FFF tensile samples tested along the layer deposition direction but less agreement (up to 60% difference) for FFF samples tested against [51]. The orientation-based differences of the latter study are particularly similar to what was observed in the current study, and in agreement with the current findings, the differences are attributed to low interface strength between layers as well as irregularities and void spaces resulting from the printing toolpath [51]. In general, geometrical mismatch between the designed and actual structures and weak interlayer bonding are often cited as the primary sources of error in porous structure modeling [21, 51, 53]. Thus, others have taken steps to improve model accuracy for 3D printed samples, such as the inclusion of print irregularities in the 3D object model [54] and multi-scale homogenization for characterizing both the porous structure and its constitutive material [51, 55, 56]. While these strategies are not implemented in the current work, they may be employed in future work to improve the fidelity of the FFF TPMS architecture-property modeling.

Ultimately, the findings presented here provide better understanding of the range of properties achievable by 3D printed porous PEEK and show promising results for the validation of the architecture-property model presented in **Chapter 4**. As porous structures continue to be explored for osseointegrative uses, the findings of

the current study may support future research regarding the design and performance of FFF porous PEEK and other 3D printed porous materials.

5.6 References

1. Ataee, A., et al., Anisotropic Ti-6Al-4V gyroid scaffolds manufactured by electron beam melting (EBM) for bone implant applications. Materials & Design, 2018. **137**: p. 345-354.

2. Bobbert, F.S.L., et al., Additively manufactured metallic porous biomaterials based on minimal surfaces: A unique combination of topological, mechanical, and mass transport properties. Acta Biomater, 2017. **53**: p. 572-584.

3. Arif, M., et al., Performance of biocompatible PEEK processed by fused deposition additive manufacturing. Materials & Design, 2018. **146**: p. 249-259.

4. de Aquino, D., et al., Investigation of load direction on the compressive strength of additively manufactured triply periodic minimal surface scaffolds. The International Journal of Advanced Manufacturing Technology, 2020. **109**(3): p. 771-779.

5. Liu, F., et al., Functionally graded porous scaffolds in multiple patterns: New design method, physical and mechanical properties. Materials & Design, 2018. **160**: p. 849-860.

6. Zheng, X., et al., Minimal surface designs for porous materials: from microstructures to mechanical properties. Journal of materials science, 2018. **53**(14): p. 10194-10208.

7. Al-Ketan, O., et al., Functionally graded and multi-morphology sheet TPMS lattices: Design, manufacturing, and mechanical properties. Journal of the mechanical behavior of biomedical materials, 2020. **102**: p. 103520.

8. Ma, S., et al., Mechanical behaviours and mass transport properties of bone-mimicking scaffolds consisted of gyroid structures manufactured using selective laser melting. J Mech Behav Biomed Mater, 2019. **93**: p. 158-169.

9. Zhu, L.Y., et al., Mechanical characterization of 3D printed multi-morphology porous Ti6Al4V scaffolds based on triply periodic minimal surface architectures. Am J Transl Res, 2018. **10**(11): p. 3443-3454.

10. Soro, N., et al., Investigation of the structure and mechanical properties of additively manufactured Ti-6Al-4V biomedical scaffolds designed with a Schwartz primitive unit-cell. Materials Science and Engineering: A, 2019. **745**: p. 195-202.

11. Gibson, L.J. and M.F. Ashby, Cellular solids: structure and properties. 1999: Cambridge university press.

12. Kladovasilakis, N., K. Tsongas, and D. Tzetzis, Mechanical and FEA-Assisted Characterization of Fused Filament Fabricated Triply Periodic Minimal Surface Structures. Journal of Composites Science, 2021. **5**(2): p. 58.

13. International, A., D695-15 Standard Test Method for Compressive Properties of Rigid Plastics. ASTM International: West Conshohocken, PA.

14. Xu, Y., et al., Study on topology optimization design, manufacturability, and performance evaluation of Ti-6Al-4V porous structures fabricated by selective laser melting (SLM). Materials, 2017. **10**(9): p. 1048.

15. ISO/IEC 17025:2005. General requirements for the competence of testing and calibration laboratories International Organization for Standardization. 2017: Geneva, Switzerland.

16. Standard Test Method for Compressive Properties of Rigid Plastics.

17. Maskery, I., et al., Insights into the mechanical properties of several triply periodic minimal surface lattice structures made by polymer additive manufacturing. Polymer, 2018. **152**: p. 62-71.

18. Maconachie, T., et al., The compressive behaviour of ABS gyroid lattice structures manufactured by fused deposition modelling. The International Journal of Advanced Manufacturing Technology, 2020. **107**(11): p. 4449-4467.

19. Yang, L., et al., An investigation into the effect of gradients on the manufacturing fidelity of triply periodic minimal surface structures with graded density fabricated by selective laser melting. Journal of Materials Processing Technology, 2020. **275**: p. 116367.

20. Al-Ketan, O., R. Rowshan, and R.K.A. Al-Rub, Topology-mechanical property relationship of 3D printed strut, skeletal, and sheet based periodic metallic cellular materials. Additive Manufacturing, 2018. **19**: p. 167-183.

21. Ma, S., et al., Manufacturability, mechanical properties, mass-transport properties and biocompatibility of triply periodic minimal surface (TPMS) porous scaffolds fabricated by selective laser melting. Materials & Design, 2020. **195**: p. 109034.

22. Alizadeh-Osgouei, M., et al., High strength porous PLA gyroid scaffolds manufactured via fused deposition modeling for tissue-engineering applications. Smart Materials in Medicine, 2021. **2**: p. 15-25.

23. Shi, J., et al., A TPMS-based method for modeling porous scaffolds for bionic bone tissue engineering. Scientific reports, 2018. **8**(1): p. 1-10.

24. Cai, Z., et al., The effect of porosity on the mechanical properties of 3D-printed triply periodic minimal surface (TPMS) bioscaffold. Bio-Design and Manufacturing, 2019. **2**(4): p. 242-255.

25. Bochmann, L., et al., Understanding error generation in fused deposition modeling. Surface Topography: Metrology and Properties, 2015. **3**(1): p. 014002.

26. Syahrom, A., et al., Mechanical and microarchitectural analyses of cancellous bone through experiment and computer simulation. Med Biol Eng Comput, 2011. **49**(12): p. 1393-403.

27. Vaezi, M. and S. Yang, Extrusion-based additive manufacturing of PEEK for biomedical applications. Virtual and Physical Prototyping, 2015. **10**(3): p. 123-135.

28. Feng, X., et al., Osteointegration of 3D-Printed Fully Porous Polyetheretherketone Scaffolds with Different Pore Sizes. ACS omega, 2020. **5**(41): p. 26655-26666.

29. Su, Y., et al., Additively-manufactured poly-ether-ether-ketone (PEEK) lattice scaffolds with uniform microporous architectures for enhanced cellular response and soft tissue adhesion. Materials & Design, 2020. **191**: p. 108671.

30. Basgul, C., et al., Structure, properties, and bioactivity of 3D printed PAEKs for implant applications: A systematic review. Journal of Biomedical Materials Research Part B: Applied Biomaterials, 2021.

31. Landy, B.C., et al., Mechanical and in vitro investigation of a porous PEEK foam for medical device implants. J Appl Biomater Funct Mater, 2013. **11**(1): p. e35-44.

32. Senatov, F., et al., Comparative analysis of structure and mechanical properties of porous PEEK and UHMWPE biomimetic scaffolds. Materials Letters, 2019. **239**: p. 63-66.

33. Siddiq, A.R. and A.R. Kennedy, Porous poly-ether ether ketone (PEEK) manufactured by a novel powder route using near-spherical salt bead porogens: characterisation and mechanical properties. Mater Sci Eng C Mater Biol Appl, 2015. **47**: p. 180-8.

34. Wang, X., et al., Topological design and additive manufacturing of porous metals for bone scaffolds and orthopaedic implants: A review. Biomaterials, 2016. **83**: p. 127-141.

35. Yan, C., et al., Ti–6Al–4V triply periodic minimal surface structures for bone implants fabricated via selective laser melting. Journal of the mechanical behavior of biomedical materials, 2015. **51**: p. 61-73.

36. Vijayavenkataraman, S., L.Y. Kuan, and W.F. Lu, 3D-printed ceramic triply periodic minimal surface structures for design of functionally graded bone implants. Materials & Design, 2020: p. 108602.

37. Abueidda, D.W., et al., Mechanical properties of 3D printed polymeric cellular materials with triply periodic minimal surface architectures. Materials & Design, 2017. **122**: p. 255-267.

38. Zaharin, H.A., et al., Effect of unit cell type and pore size on porosity and mechanical behavior of additively manufactured Ti6Al4V scaffolds. Materials, 2018. **11**(12): p. 2402.

39. Murr, L.E., et al., Next-generation biomedical implants using additive manufacturing of complex, cellular and functional mesh arrays. Philosophical Transactions of the Royal Society A: Mathematical, Physical and Engineering Sciences, 2010. **368**(1917): p. 1999-2032.

40. Karageorgiou, V. and D. Kaplan, Porosity of 3D biomaterial scaffolds and osteogenesis. Biomaterials, 2005. **26**(27): p. 5474-5491.

41. Miao, X. and D. Sun, Graded/gradient porous biomaterials. Materials, 2010. **3**(1): p. 26-47.

42. Afshar, M., et al., Additive manufacturing and mechanical characterization of graded porosity scaffolds designed based on triply periodic minimal surface architectures. Journal of the mechanical behavior of biomedical materials, 2016. **62**: p. 481-494.

43. Li, D., et al., Comparison of mechanical properties and energy absorption of sheet-based and strut-based gyroid cellular structures with graded densities. Materials, 2019. **12**(13): p. 2183.

44. Yang, L., et al., Continuous graded Gyroid cellular structures fabricated by selective laser melting: Design, manufacturing and mechanical properties. Materials & Design, 2019. **162**: p. 394-404.

45. Lu, Y., et al., The anisotropic elastic behavior of the widely-used triply-periodic minimal surface based scaffolds. Journal of the mechanical behavior of biomedical materials, 2019. **99**: p. 56-65.

46. Casavola, C., et al., Orthotropic mechanical properties of fused deposition modelling parts described by classical laminate theory. Materials & design, 2016. **90**: p. 453-458.

47. Gao, X., et al., Fused filament fabrication of polymer materials: A review of interlayer bond. Additive Manufacturing, 2020: p. 101658.

48. Afshar, M., A.P. Anaraki, and H. Montazerian, Compressive characteristics of radially graded porosity scaffolds architectured with minimal surfaces. Materials Science and Engineering: C, 2018. **92**: p. 254-267.

49. Tripathi, Y., M. Shukla, and A.D. Bhatt, Implicit-function-based design and additive manufacturing of triply periodic minimal surfaces scaffolds for bone tissue engineering. Journal of Materials Engineering and Performance, 2019. **28**(12): p. 7445-7451.

50. Castro, A., et al., Numerical and experimental evaluation of TPMS Gyroid scaffolds for bone tissue engineering. Computer methods in biomechanics and biomedical engineering, 2019. **22**(6): p. 567-573.

51. Nasirov, A. and I. Fidan, Prediction of mechanical properties of fused filament fabricated structures via asymptotic homogenization. Mechanics of Materials, 2020. **145**: p. 103372.

52. Cheng, L., et al., Natural frequency optimization of variable-density additive manufactured lattice structure: theory and experimental validation. Journal of Manufacturing Science and Engineering, 2018. **140**(10).

53. Herrera, A., et al., Computational study and experimental validation of porous structures fabricated by electron beam melting: A challenge to avoid stress shielding. Materials Science and Engineering: C, 2014. **45**: p. 89-93.

54. Campoli, G., et al., Mechanical properties of open-cell metallic biomaterials manufactured using additive manufacturing. Materials & Design, 2013. **49**: p. 957-965.

55. Somireddy, M., A. Czekanski, and C.V. Singh, Development of constitutive material model of 3D printed structure via FDM. Materials Today Communications, 2018. **15**: p. 143-152.

56. Nguyen, C.H.P., Y. Kim, and Y. Choi, Design for additive manufacturing of functionally graded lattice structures: a design method with process induced anisotropy consideration. International Journal of Precision Engineering and Manufacturing-Green Technology, 2019: p. 1-17.

Chapter 6: Conclusions and Future Work

6.1 Summary

Additive manufacturing is being adopted at an increasing rate for orthopaedic applications, with PEEK representing one of the most promising materials. The overall goal of this work was to establish how porous PEEK may be additively manufactured to serve as an osseointegrative implant material and to explore the impact of using triply periodic minimal surface design. The findings reported in **Aim 1** demonstrated the feasibility of creating porous PEEK using the fused filament fabrication method and established its potential for use in orthopaedic implant applications. TPMS structures based on the gyroid and diamond geometries were successfully created in PEEK using the FFF process and showed good agreement with the as-designed architecture. Superior mechanical properties were reported for the TPMS structures compared to traditional rectilinear lattice, with the average yield strength and Young's modulus calculated as 14.8 MPa and 210 MPa for the gyroid and 17.2 MPa and 268 MPa for the diamond. For *in vitro* testing with preosteoblast cells, increased ALP activity was demonstrated for the porous structures compared to flat PEEK, supporting the hypothesis that the bioinert nature of PEEK could be overcome by additively manufactured porosity. The promising results of **Aim 1** led to a deeper exploration of the TPMS-inspired porous PEEK mechanical properties in the following aims. As the properties and anisotropy imparted on PEEK by the FFF process is not fully understood, the

purpose of **Aim 2** was to characterize the behavior of this material both parallel and normal to the layer deposition direction. It was found that the solid PEEK in compression was less anisotropic than what has been previously reported for tension, though samples loaded perpendicular to layer direction were generally more ductile than those loaded parallel. The results from this aim also provided the constitutive material elastic constants for subsequent porous PEEK modeling. In **Aim 3**, models were created to relate the design parameters, architectural characteristics, and predicted elastic modulus (determined via homogenization) for the gyroid and diamond TPMS structures, and the work in **Aim 4** provided a validation of the diamond architecture-property model for FFF PEEK. In this aim, structures representing six different points within the model additively manufactured, and the structural characteristics and mechanical behavior in compression were assessed. Bending-dominated deformation and layer splitting were the most common failure modes, and printing orientation greatly affected the mechanical properties. The experimental data agreed well with the predicted values for the z-direction samples but less so for the xy-direction samples due to print irregularities. Future work in optimizing the print parameters for each porous architecture or including irregularities in the 3D object model may show improved results.

The potential impact of this research is varied and includes work that may be translated into a clinical setting. First, the research includes, to the author's

knowledge, the first report of TPMS-inspired structures additively manufacturing using PEEK. The promising biologic and mechanical testing results further support this new material as a potential tool for implant fixation that avoids the negative impacts metal and bone cement. Moreover, the FFF process used to create the structures can be utilized for creating patient-specific implants and is being increasingly adopted in clinical settings. Because interest in FFF PEEK is growing in general, a second significant contribution of the current work is the characterization of both porous and solid 3D printed PEEK, which may be utilized in future studies exploring the potential applications of the material. Finally, the modeling performed in this thesis provides a novel tool for researchers aiming to design tunable porous scaffolds based on triply periodic minimal surfaces. Because the architecture models were created to be independent of base material, they may be useful for a wide range of applications, an important benefit considering the increasing use of TPMS structures across multiple industries. Ultimately, while the goal of this research was to advance orthopaedic additive manufacturing and point of care implant creation specifically, the findings presented in this work may be generalized to serve a wider range of research interests.

6.2 Future Work

Fused filament fabrication of PEEK is a budding technology, and there is still much to learn about the process, the material itself, and the possible applications. The results presented in this thesis opens the door to many new research directions for

porous PEEK and the adoption of 3D printing for orthopaedic uses in general. Some potential areas of work directly related to this thesis include validating the predictive model for gyroids, expanding the family of TPMS architecture maps for more geometries, exploring graded porosity, and investigating more porous PEEK mechanical properties including fatigue behavior. More opportunities for future research are detailed below.

An evident and particularly important next step in the research of FFF porous PEEK is investigating the biologic response *in vivo*, because while cell testing is a highly valuable tool in biomaterial assessment, *in vitro* methods cannot fully elucidate the characteristics of material performance and bone ingrowth. Testing with preclinical animal models, on the other hand, is useful for determining factors like local and systemic biocompatibility, bone-implant interface strength, and potential capsule fiber growth [1]. Simply put, it is a necessary measure towards adopting FFF porous PEEK for human orthopaedics. *In vivo* testing will also allow for bone ingrowth optimization of porous structures and provide means to compare this new biomaterial with clinically relevant benchmarks. Importantly, the plan to test *in vivo* will also spur work regarding sterilization of these structures, an already budding area of research for 3D printed medical devices [2-5].

Another large area of future research relates to the biomaterials able to be used in FFF for creating porous structures. Within the PAEK family alone, several materials and related composites have been introduced since PEEK filament for FFF became

widely available in the last few years [6]. Two materials gaining particular interest include polyetherketoneketone (PEKK) and carbon-fiber reinforced PEEK, which may enhance the bioactivity and mechanical properties of FFF PAEK, respectively [7, 8]. Like any new biomaterial, each material will need to undergo a series of biological and mechanical experiments to determine its suitability for bone ingrowth or other point of care 3D printing applications. Even for plain PEEK, additional testing of material from different manufacturers may be useful, as qualitative differences in print results using PEEK from different sources is often observed. As the ongoing introduction of new printable PAEKs generates a plethora of questions to explore in the near future, so too will the ability to dual extrude materials, a technique that is expected to be adapted from low temperature printers. Dual extrusion will be particularly transformative for PEEK TPMS printing if dissolvable/easy-to-remove high temperature support materials are developed, as the manufacturing of certain geometries like the Schwarz Primitive surface will benefit from supports [9]. In general, the ability to co-print materials alongside thermopolymers like PEEK will increase the complexity of printable structures and open the door for even more innovative AM solutions.

While the current work focuses just on the creation and basic characterization of FFF porous PEEK, future work will be needed to understand how the material may fit into the grander scheme of orthopaedic applications. For example, many implants involve a combination of materials, such as an implant with

osseointegrative porous metal on one side and smooth articulating polyethylene on the other. It will be necessary to not only determine how porous PEEK may be combined with another biomaterial during or after the printing process but also to characterize important factors like the interface strength between the materials. Additionally, orthopaedic biomaterials are often tasked with performing more than one function *in vivo*, such as antibiotic-doped bone cement, and it may be important for porous PEEK to do the same. While it remains to be explored, the architecture of the porous presented in this work may facilitate a number of functions including infection resistance through drug delivery or increased osteoconductivity through coatings like hydroxyapatite, similar to what has been seen for other porous biomaterials [10]. Ultimately, there are a variety of potential opportunities for future investigations into porous PEEK and other AM orthopaedic biomaterials, and gaining a better understanding of these materials will add to the exciting work regarding patient-specific implants and 3D printing at the point of care.

6.3 References

1. Spece, H., et al., *A systematic review of preclinical in vivo testing of 3D printed porous Ti6Al4V for orthopedic applications, part I: Animal models and bone ingrowth outcome measures.* Journal of Biomedical Materials Research Part B: Applied Biomaterials, 2021.
2. Manea, A., et al., *Sterilization protocol for porous dental implants made by Selective Laser Melting.* Clujul Medical, 2018. **91**(4): p. 452.
3. Ferràs-Tarragó, J., et al., *Security of 3D-printed polylactide acid piece sterilization in the operating room: a sterility test.* European Journal of Trauma and Emergency Surgery, 2021: p. 1-6.

4. Aguado-Maestro, I., et al., *Are the common sterilization methods completely effective for our in-house 3D printed biomodels and surgical guides?* Injury, 2020.

5. Majumdar, T., et al., *Additive manufacturing of titanium alloys for orthopedic applications: a materials science viewpoint.* Advanced Engineering Materials, 2018. **20**(9): p. 1800172.

6. Basgul, C., et al., *Structure, properties, and bioactivity of 3D printed PAEKs for implant applications: A systematic review.* Journal of Biomedical Materials Research Part B: Applied Biomaterials, 2021.

7. Liao, C., Y. Li, and S.C. Tjong, *Polyetheretherketone and Its Composites for Bone Replacement and Regeneration.* Polymers, 2020. **12**(12): p. 2858.

8. Cheng, B.C., et al., *A comparative study of three biomaterials in an ovine bone defect model.* The Spine Journal, 2020. **20**(3): p. 457-464.

9. Soro, N., et al., *Investigation of the structure and mechanical properties of additively manufactured Ti-6Al-4V biomedical scaffolds designed with a Schwartz primitive unit-cell.* Materials Science and Engineering: A, 2019. **745**: p. 195-202.

10. Zadpoor, A.A., *Additively manufactured porous metallic biomaterials.* Journal of Materials Chemistry B, 2019. **7**(26): p. 4088-4117.

Appendix A: TPMS Design and Topology Parameter Values for Gyroid and Diamond Geometries

Table A.1. TPMS structure design values and resulting architecture characteristics.

Gyroid				Diamond			
Scaling factor	**Strut Thickness (mm)**	**Pore Size (mm)**	**Porosity (%)**	**Scaling factor**	**Strut Thickness (mm)**	**Pore Size (mm)**	**Porosity (%)**
0.30	0.100	0.306	83.62	0.30	0.100	0.309	80.36
0.30	0.110	0.296	81.99	0.30	0.110	0.303	78.42
0.30	0.120	0.284	80.37	0.30	0.120	0.298	76.49
0.30	0.130	0.277	78.75	0.30	0.130	0.283	74.56
0.30	0.140	0.265	77.14	0.30	0.140	0.278	72.64
0.30	0.150	0.256	75.53	0.30	0.150	0.261	70.73
0.30	0.160	0.245	73.93	0.30	0.160	0.258	68.83
0.30	0.170	0.237	72.33	0.30	0.170	0.245	66.95
0.30	0.180	0.226	70.74	0.30	0.180	0.234	65.07
0.30	0.190	0.216	69.16	0.30	0.190	0.223	63.20
0.30	0.200	0.204	67.58	0.30	0.200	0.217	61.35
0.30	0.210	0.194	66.01	0.30	0.210	0.207	59.51
0.30	0.220	0.185	64.45	0.30	0.220	0.199	57.69
0.30	0.230	0.175	62.89	0.30	0.230	0.183	55.88
0.30	0.240	0.168	61.34	0.30	0.240	0.173	54.08
0.30	0.250	0.152	59.80	0.30	0.250	0.165	52.30
0.30	0.260	0.145	58.27	0.30	0.260	0.159	50.54
0.30	0.270	0.132	56.75	0.30	0.270	0.149	48.80
0.30	0.280	0.127	55.24	0.30	0.280	0.135	47.07
0.30	0.290	0.115	53.74	0.30	0.290	0.125	45.36
0.30	0.300	0.123	52.25	0.30	0.300	0.114	43.68
0.30	0.310	0.094	50.77	0.30	0.310	0.106	42.01
0.30	0.320	0.090	49.31	0.30	0.320	0.100	40.37
0.30	0.330	0.076	47.85	0.30	0.330	0.088	38.74
0.35	0.100	0.401	85.90	0.35	0.100	0.403	83.20
0.35	0.113	0.388	84.15	0.35	0.113	0.393	81.13
0.35	0.125	0.377	82.40	0.35	0.125	0.380	79.06

0.35	0.138	0.360	80.66	0.35	0.138	0.368	77.00
0.35	0.150	0.351	78.92	0.35	0.150	0.354	74.94
0.35	0.163	0.338	77.19	0.35	0.163	0.341	72.90
0.35	0.175	0.325	75.46	0.35	0.175	0.330	70.87
0.35	0.188	0.312	73.74	0.35	0.188	0.320	68.85
0.35	0.200	0.299	72.02	0.35	0.200	0.300	66.85
0.35	0.213	0.287	70.32	0.35	0.213	0.290	64.86
0.35	0.225	0.274	68.62	0.35	0.225	0.284	62.88
0.35	0.238	0.264	66.93	0.35	0.238	0.265	60.92
0.35	0.250	0.251	65.24	0.35	0.250	0.258	58.97
0.35	0.263	0.235	63.57	0.35	0.263	0.240	57.04
0.35	0.275	0.223	61.91	0.35	0.275	0.232	55.13
0.35	0.288	0.212	60.25	0.35	0.288	0.221	53.24
0.35	0.300	0.198	58.61	0.35	0.300	0.201	51.37
0.35	0.313	0.188	56.97	0.35	0.313	0.197	49.52
0.35	0.325	0.172	55.35	0.35	0.325	0.182	47.69
0.35	0.338	0.160	53.74	0.35	0.338	0.170	45.89
0.35	0.350	0.148	52.14	0.35	0.350	0.157	44.10
0.35	0.363	0.137	50.56	0.35	0.363	0.138	42.34
0.35	0.375	0.125	48.99	0.35	0.375	0.134	40.61
0.35	0.388	0.112	47.43	0.35	0.388	0.123	38.90
0.40	0.100	0.460	87.89	0.40	0.100	0.495	84.99
0.40	0.115	0.445	86.08	0.40	0.115	0.477	82.76
0.40	0.130	0.430	84.27	0.40	0.130	0.447	80.53
0.40	0.145	0.416	82.47	0.40	0.145	0.447	78.31
0.40	0.160	0.402	80.67	0.40	0.160	0.434	76.10
0.40	0.175	0.385	78.88	0.40	0.175	0.420	73.91
0.40	0.190	0.369	77.10	0.40	0.190	0.405	71.72
0.40	0.205	0.354	75.31	0.40	0.205	0.382	69.55
0.40	0.220	0.340	73.54	0.40	0.220	0.378	67.39
0.40	0.235	0.325	71.77	0.40	0.235	0.363	65.25
0.40	0.250	0.310	70.02	0.40	0.250	0.348	63.12
0.40	0.265	0.294	68.26	0.40	0.265	0.317	61.01
0.40	0.280	0.278	66.52	0.40	0.280	0.316	58.92
0.40	0.295	0.264	64.79	0.40	0.295	0.307	56.85
0.40	0.310	0.251	63.07	0.40	0.310	0.273	54.80
0.40	0.325	0.232	61.35	0.40	0.325	0.278	52.77
0.40	0.340	0.218	59.65	0.40	0.340	0.247	50.76

0.40	0.355	0.201	57.96	0.40	0.355	0.249	48.77
0.40	0.370	0.187	56.28	0.40	0.370	0.218	46.81
0.40	0.385	0.175	54.62	0.40	0.385	0.204	44.88
0.40	0.400	0.159	52.96	0.40	0.400	0.189	42.97
0.40	0.415	0.145	51.32	0.40	0.415	0.189	41.09
0.40	0.430	0.128	49.70	0.40	0.430	0.158	39.24
0.40	0.445	0.113	48.08	0.40	0.445	0.158	37.41
0.45	0.100	0.558	89.15	0.45	0.100	0.573	86.71
0.45	0.118	0.543	87.26	0.45	0.118	0.531	84.40
0.45	0.135	0.522	85.40	0.45	0.135	0.543	82.09
0.45	0.153	0.505	83.51	0.45	0.153	0.501	79.80
0.45	0.170	0.487	81.65	0.45	0.170	0.506	77.51
0.45	0.188	0.473	79.76	0.45	0.188	0.489	75.23
0.45	0.205	0.453	77.90	0.45	0.205	0.474	72.97
0.45	0.223	0.434	76.05	0.45	0.223	0.447	70.72
0.45	0.240	0.417	74.19	0.45	0.240	0.438	68.48
0.45	0.258	0.400	72.38	0.45	0.258	0.417	66.26
0.45	0.275	0.384	70.52	0.45	0.275	0.400	64.05
0.45	0.293	0.365	68.71	0.45	0.293	0.378	61.86
0.45	0.310	0.345	66.90	0.45	0.310	0.366	59.69
0.45	0.328	0.329	65.08	0.45	0.328	0.346	57.54
0.45	0.345	0.313	63.31	0.45	0.345	0.328	55.42
0.45	0.363	0.293	61.49	0.45	0.363	0.314	53.31
0.45	0.380	0.274	59.72	0.45	0.380	0.298	51.23
0.45	0.398	0.261	57.98	0.45	0.398	0.273	49.17
0.45	0.415	0.240	56.21	0.45	0.415	0.260	47.14
0.45	0.433	0.224	54.48	0.45	0.433	0.213	45.14
0.45	0.450	0.202	52.74	0.45	0.450	0.227	43.16
0.45	0.468	0.188	51.05	0.45	0.468	0.184	41.22
0.45	0.485	0.169	49.35	0.45	0.485	0.199	39.30
0.45	0.503	0.133	47.66	0.45	0.503	0.153	37.42
0.50	0.100	0.636	90.31	0.50	0.100	0.646	87.98
0.50	0.120	0.619	88.37	0.50	0.120	0.627	85.59
0.50	0.140	0.596	86.44	0.50	0.140	0.610	83.20
0.50	0.160	0.579	84.52	0.50	0.160	0.594	80.83
0.50	0.180	0.558	82.60	0.50	0.180	0.570	78.46
0.50	0.200	0.537	80.68	0.50	0.200	0.546	76.11
0.50	0.220	0.519	78.78	0.50	0.220	0.531	73.77

0.50	0.240	0.500	76.87	0.50	0.240	0.515	71.44
0.50	0.260	0.479	74.98	0.50	0.260	0.493	69.13
0.50	0.280	0.460	73.09	0.50	0.280	0.475	66.84
0.50	0.300	0.439	71.22	0.50	0.300	0.446	64.56
0.50	0.320	0.417	69.35	0.50	0.320	0.435	62.30
0.50	0.340	0.399	67.49	0.50	0.340	0.414	60.07
0.50	0.360	0.381	65.64	0.50	0.360	0.394	57.85
0.50	0.380	0.358	63.80	0.50	0.380	0.374	55.66
0.50	0.400	0.341	61.98	0.50	0.400	0.345	53.49
0.50	0.420	0.316	60.17	0.50	0.420	0.338	51.35
0.50	0.440	0.297	58.37	0.50	0.440	0.316	49.23
0.50	0.460	0.276	56.58	0.50	0.460	0.293	47.14
0.50	0.480	0.264	54.81	0.50	0.480	0.271	45.08
0.50	0.500	0.234	53.05	0.50	0.500	0.245	43.05
0.50	0.520	0.218	51.31	0.50	0.520	0.239	41.06
0.50	0.540	0.196	49.59	0.50	0.540	0.210	39.09
0.50	0.560	0.176	47.88	0.50	0.560	0.191	37.16
0.55	0.100	0.717	90.86	0.55	0.100	0.701	89.43
0.55	0.123	0.696	88.81	0.55	0.123	0.678	87.06
0.55	0.145	0.671	86.76	0.55	0.145	0.659	84.70
0.55	0.168	0.648	84.72	0.55	0.168	0.641	82.34
0.55	0.190	0.627	82.68	0.55	0.190	0.620	79.99
0.55	0.213	0.603	80.65	0.55	0.213	0.593	77.66
0.55	0.235	0.583	78.62	0.55	0.235	0.569	75.33
0.55	0.258	0.558	76.60	0.55	0.258	0.547	73.02
0.55	0.280	0.537	74.59	0.55	0.280	0.524	70.71
0.55	0.303	0.514	72.59	0.55	0.303	0.500	68.43
0.55	0.325	0.493	70.59	0.55	0.325	0.479	66.16
0.55	0.348	0.470	68.61	0.55	0.348	0.462	63.91
0.55	0.370	0.446	66.63	0.55	0.370	0.439	61.67
0.55	0.393	0.423	64.67	0.55	0.393	0.410	59.46
0.55	0.415	0.401	62.72	0.55	0.415	0.385	57.27
0.55	0.438	0.378	60.78	0.55	0.438	0.368	55.10
0.55	0.460	0.358	58.86	0.55	0.460	0.348	52.95
0.55	0.483	0.333	56.95	0.55	0.483	0.322	50.83
0.55	0.505	0.310	55.05	0.55	0.505	0.299	48.73
0.55	0.528	0.288	53.17	0.55	0.528	0.278	46.66
0.55	0.550	0.264	51.31	0.55	0.550	0.249	44.62

0.55	0.573	0.240	49.46	0.55	0.573	0.228	42.62
0.55	0.595	0.217	47.63	0.55	0.595	0.216	40.64
0.55	0.618	0.194	45.82	0.55	0.618	0.187	38.69
0.60	0.100	0.798	92.12	0.60	0.100	0.819	89.93
0.60	0.125	0.775	90.15	0.60	0.125	0.795	87.42
0.60	0.150	0.751	88.19	0.60	0.150	0.773	84.92
0.60	0.175	0.724	86.23	0.60	0.175	0.743	82.43
0.60	0.200	0.699	84.27	0.60	0.200	0.723	79.94
0.60	0.225	0.676	82.32	0.60	0.225	0.696	77.47
0.60	0.250	0.649	80.38	0.60	0.250	0.669	75.00
0.60	0.275	0.624	78.44	0.60	0.275	0.647	72.56
0.60	0.300	0.600	76.50	0.60	0.300	0.623	70.12
0.60	0.325	0.573	74.58	0.60	0.325	0.594	67.71
0.60	0.350	0.547	72.66	0.60	0.350	0.573	65.31
0.60	0.375	0.522	70.76	0.60	0.375	0.549	62.93
0.60	0.400	0.500	68.86	0.60	0.400	0.521	60.57
0.60	0.425	0.473	66.97	0.60	0.425	0.493	58.24
0.60	0.450	0.449	65.09	0.60	0.450	0.476	55.93
0.60	0.475	0.423	63.23	0.60	0.475	0.447	53.64
0.60	0.500	0.397	61.38	0.60	0.500	0.425	51.38
0.60	0.525	0.371	59.54	0.60	0.525	0.390	49.15
0.60	0.550	0.349	57.71	0.60	0.550	0.376	46.95
0.60	0.575	0.323	55.90	0.60	0.575	0.345	44.78
0.60	0.600	0.297	54.10	0.60	0.600	0.326	42.65
0.60	0.625	0.270	52.32	0.60	0.625	0.288	40.55
0.60	0.650	0.244	50.55	0.60	0.650	0.270	38.48
0.60	0.675	0.223	48.80	0.60	0.675	0.246	36.45
0.65	0.100	0.882	92.62	0.65	0.100	0.894	90.86
0.65	0.128	0.855	90.59	0.65	0.128	0.868	88.35
0.65	0.155	0.829	88.57	0.65	0.155	0.847	85.85
0.65	0.183	0.801	86.55	0.65	0.183	0.817	83.36
0.65	0.210	0.775	84.53	0.65	0.210	0.795	80.88
0.65	0.238	0.746	82.52	0.65	0.238	0.767	78.41
0.65	0.265	0.720	80.52	0.65	0.265	0.735	75.95
0.65	0.293	0.695	78.52	0.65	0.293	0.717	73.50
0.65	0.320	0.667	76.53	0.65	0.320	0.689	71.07
0.65	0.348	0.639	74.55	0.65	0.348	0.654	68.65
0.65	0.375	0.611	72.58	0.65	0.375	0.637	66.26

0.65	0.403	0.582	70.61	0.65	0.403	0.606	63.88
0.65	0.430	0.557	68.66	0.65	0.430	0.575	61.52
0.65	0.458	0.529	66.72	0.65	0.458	0.553	59.19
0.65	0.485	0.502	64.79	0.65	0.485	0.522	56.88
0.65	0.513	0.473	62.87	0.65	0.513	0.497	54.60
0.65	0.540	0.444	60.97	0.65	0.540	0.469	52.34
0.65	0.568	0.415	59.08	0.65	0.568	0.441	50.11
0.65	0.595	0.389	57.20	0.65	0.595	0.417	47.91
0.65	0.623	0.361	55.34	0.65	0.623	0.376	45.74
0.65	0.650	0.333	53.49	0.65	0.650	0.361	43.60
0.65	0.678	0.301	51.67	0.65	0.678	0.331	41.50
0.65	0.705	0.274	49.86	0.65	0.705	0.296	39.43
0.65	0.733	0.246	48.06	0.65	0.733	0.267	37.40
0.70	0.100	0.961	92.89	0.70	0.100	0.977	91.22
0.70	0.130	0.930	90.77	0.70	0.130	0.952	88.59
0.70	0.160	0.902	88.64	0.70	0.160	0.922	85.97
0.70	0.190	0.872	86.52	0.70	0.190	0.900	83.36
0.70	0.220	0.843	84.40	0.70	0.220	0.861	80.76
0.70	0.250	0.815	82.29	0.70	0.250	0.839	78.17
0.70	0.280	0.783	80.19	0.70	0.280	0.810	75.59
0.70	0.310	0.754	78.09	0.70	0.310	0.780	73.03
0.70	0.340	0.723	76.00	0.70	0.340	0.747	70.48
0.70	0.370	0.692	73.92	0.70	0.370	0.725	67.96
0.70	0.400	0.665	71.85	0.70	0.400	0.686	65.45
0.70	0.430	0.635	69.79	0.70	0.430	0.664	62.96
0.70	0.460	0.603	67.74	0.70	0.460	0.631	60.50
0.70	0.490	0.573	65.70	0.70	0.490	0.602	58.06
0.70	0.520	0.543	63.67	0.70	0.520	0.568	55.64
0.70	0.550	0.513	61.66	0.70	0.550	0.545	53.26
0.70	0.580	0.482	59.66	0.70	0.580	0.507	50.90
0.70	0.610	0.453	57.68	0.70	0.610	0.483	48.58
0.70	0.640	0.421	55.72	0.70	0.640	0.447	46.29
0.70	0.670	0.388	53.77	0.70	0.670	0.420	44.03
0.70	0.700	0.362	51.84	0.70	0.700	0.393	41.81
0.70	0.730	0.330	49.92	0.70	0.730	0.357	39.63
0.70	0.760	0.299	48.03	0.70	0.760	0.329	37.48
0.70	0.790	0.265	46.15	0.70	0.790	0.288	35.38
0.75	0.100	1.036	93.18	0.75	0.100	1.026	92.40

0.75	0.133	1.002	90.96	0.75	0.133	0.994	89.94
0.75	0.165	0.969	88.75	0.75	0.165	0.963	87.48
0.75	0.198	0.937	86.54	0.75	0.198	0.930	85.02
0.75	0.230	0.905	84.34	0.75	0.230	0.901	82.58
0.75	0.263	0.873	82.14	0.75	0.263	0.868	80.15
0.75	0.295	0.841	79.95	0.75	0.295	0.836	77.72
0.75	0.328	0.808	77.77	0.75	0.328	0.799	75.31
0.75	0.360	0.775	75.59	0.75	0.360	0.766	72.91
0.75	0.393	0.741	73.43	0.75	0.393	0.739	70.53
0.75	0.425	0.709	71.27	0.75	0.425	0.705	68.17
0.75	0.458	0.675	69.13	0.75	0.458	0.675	65.82
0.75	0.490	0.647	66.99	0.75	0.490	0.639	63.50
0.75	0.523	0.610	64.87	0.75	0.523	0.603	61.19
0.75	0.555	0.578	62.76	0.75	0.555	0.574	58.91
0.75	0.588	0.547	60.67	0.75	0.588	0.542	56.65
0.75	0.620	0.512	58.59	0.75	0.620	0.511	54.42
0.75	0.653	0.479	56.53	0.75	0.653	0.472	52.21
0.75	0.685	0.443	54.48	0.75	0.685	0.441	50.04
0.75	0.718	0.412	52.46	0.75	0.718	0.406	47.89
0.75	0.750	0.380	50.45	0.75	0.750	0.382	45.77
0.75	0.783	0.348	48.46	0.75	0.783	0.342	43.69
0.75	0.815	0.316	46.49	0.75	0.815	0.305	41.64
0.75	0.848	0.279	44.54	0.75	0.848	0.282	39.63
0.80	0.100	1.077	93.84	0.80	0.100	1.128	92.77
0.80	0.135	1.041	91.69	0.80	0.135	1.071	90.25
0.80	0.170	1.006	89.53	0.80	0.170	1.037	87.73
0.80	0.205	0.970	87.39	0.80	0.205	1.000	85.22
0.80	0.240	0.934	85.24	0.80	0.240	0.967	82.71
0.80	0.275	0.899	83.11	0.80	0.275	0.958	80.22
0.80	0.310	0.864	80.97	0.80	0.310	0.897	77.74
0.80	0.345	0.829	78.85	0.80	0.345	0.860	75.27
0.80	0.380	0.792	76.73	0.80	0.380	0.829	72.82
0.80	0.415	0.757	74.62	0.80	0.415	0.792	70.39
0.80	0.450	0.720	72.52	0.80	0.450	0.753	67.97
0.80	0.485	0.686	70.43	0.80	0.485	0.722	65.58
0.80	0.520	0.651	68.35	0.80	0.520	0.682	63.20
0.80	0.555	0.615	66.28	0.80	0.555	0.676	60.85
0.80	0.590	0.579	64.23	0.80	0.590	0.615	58.52

0.80	0.625	0.544	62.19	0.80	0.625	0.576	56.22
0.80	0.660	0.509	60.16	0.80	0.660	0.543	53.95
0.80	0.695	0.472	58.14	0.80	0.695	0.511	51.71
0.80	0.730	0.436	56.14	0.80	0.730	0.472	49.50
0.80	0.765	0.401	54.16	0.80	0.765	0.440	47.32
0.80	0.800	0.366	52.20	0.80	0.800	0.426	45.18
0.80	0.835	0.330	50.25	0.80	0.835	0.370	43.07
0.80	0.870	0.294	48.32	0.80	0.870	0.334	41.00
0.80	0.905	0.259	46.42	0.80	0.905	0.303	38.97
0.85	0.100	1.192	94.31	0.85	0.100	1.182	92.95
0.85	0.138	1.157	92.22	0.85	0.138	1.142	90.31
0.85	0.175	1.118	90.08	0.85	0.175	1.106	87.68
0.85	0.213	1.082	87.98	0.85	0.213	1.070	85.05
0.85	0.250	1.046	85.89	0.85	0.250	1.031	82.44
0.85	0.288	1.007	83.75	0.85	0.288	0.994	79.83
0.85	0.325	0.970	81.65	0.85	0.325	0.954	77.24
0.85	0.363	0.930	79.56	0.85	0.363	0.917	74.66
0.85	0.400	0.897	77.50	0.85	0.400	0.882	72.10
0.85	0.438	0.856	75.40	0.85	0.438	0.845	69.55
0.85	0.475	0.818	73.35	0.85	0.475	0.807	67.03
0.85	0.513	0.780	71.29	0.85	0.513	0.770	64.52
0.85	0.550	0.744	69.23	0.85	0.550	0.733	62.04
0.85	0.588	0.704	67.18	0.85	0.588	0.692	59.59
0.85	0.625	0.667	65.16	0.85	0.625	0.658	57.16
0.85	0.663	0.630	63.15	0.85	0.663	0.616	54.76
0.85	0.700	0.592	61.13	0.85	0.700	0.579	52.39
0.85	0.738	0.552	59.15	0.85	0.738	0.544	50.05
0.85	0.775	0.513	57.18	0.85	0.775	0.497	47.75
0.85	0.813	0.475	55.20	0.85	0.813	0.465	45.48
0.85	0.850	0.441	53.27	0.85	0.850	0.425	43.25
0.85	0.888	0.399	51.33	0.85	0.888	0.391	41.06
0.85	0.925	0.361	49.44	0.85	0.925	0.353	38.91
0.85	0.963	0.323	47.54	0.85	0.963	0.317	36.80
0.90	0.100	1.274	94.68	0.90	0.100	1.272	93.52
0.90	0.140	1.235	92.54	0.90	0.140	1.236	90.94
0.90	0.180	1.196	90.44	0.90	0.180	1.196	88.36
0.90	0.220	1.159	88.31	0.90	0.220	1.158	85.79
0.90	0.260	1.119	86.21	0.90	0.260	1.120	83.22

0.90	0.300	1.081	84.07	0.90	0.300	1.107	80.67
0.90	0.340	1.040	81.98	0.90	0.340	1.044	78.12
0.90	0.380	1.002	79.88	0.90	0.380	1.032	75.59
0.90	0.420	0.963	77.78	0.90	0.420	0.965	73.08
0.90	0.460	0.921	75.73	0.90	0.460	0.926	70.58
0.90	0.500	0.881	73.63	0.90	0.500	0.887	68.10
0.90	0.540	0.841	71.57	0.90	0.540	0.847	65.64
0.90	0.580	0.801	69.52	0.90	0.580	0.806	63.20
0.90	0.620	0.762	67.50	0.90	0.620	0.765	60.79
0.90	0.660	0.721	65.44	0.90	0.660	0.754	58.39
0.90	0.700	0.679	63.43	0.90	0.700	0.686	56.03
0.90	0.740	0.640	61.41	0.90	0.740	0.650	53.69
0.90	0.780	0.599	59.44	0.90	0.780	0.610	51.39
0.90	0.820	0.559	57.46	0.90	0.820	0.590	49.11
0.90	0.860	0.516	55.52	0.90	0.860	0.522	46.87
0.90	0.900	0.474	53.55	0.90	0.900	0.480	44.66
0.90	0.940	0.437	51.65	0.90	0.940	0.445	42.48
0.90	0.980	0.394	49.72	0.90	0.980	0.396	40.35
0.90	1.020	0.355	47.82	0.90	1.020	0.354	38.25
0.95	0.100	1.352	94.92	0.95	0.100	1.346	93.81
0.95	0.143	1.311	92.74	0.95	0.143	1.310	91.18
0.95	0.185	1.274	90.60	0.95	0.185	1.272	88.56
0.95	0.228	1.231	88.43	0.95	0.228	1.232	85.95
0.95	0.270	1.191	86.29	0.95	0.270	1.192	83.34
0.95	0.313	1.152	84.19	0.95	0.313	1.152	80.74
0.95	0.355	1.108	82.02	0.95	0.355	1.115	78.16
0.95	0.398	1.069	79.88	0.95	0.398	1.077	75.58
0.95	0.440	1.027	77.78	0.95	0.440	1.036	73.03
0.95	0.483	0.984	75.65	0.95	0.483	0.994	70.48
0.95	0.525	0.942	73.55	0.95	0.525	0.951	67.96
0.95	0.568	0.900	71.45	0.95	0.568	0.910	65.46
0.95	0.610	0.860	69.40	0.95	0.610	0.871	62.98
0.95	0.653	0.813	67.30	0.95	0.653	0.833	60.52
0.95	0.695	0.770	65.24	0.95	0.695	0.794	58.08
0.95	0.738	0.728	63.19	0.95	0.738	0.749	55.67
0.95	0.780	0.685	61.17	0.95	0.780	0.702	53.29
0.95	0.823	0.641	59.15	0.95	0.823	0.655	50.94
0.95	0.865	0.598	57.14	0.95	0.865	0.610	48.62

0.95	0.908	0.554	55.16	0.95	0.908	0.569	46.34
0.95	0.950	0.508	53.23	0.95	0.950	0.524	44.09
0.95	0.993	0.466	51.25	0.95	0.993	0.474	41.87
0.95	1.035	0.422	49.31	0.95	1.035	0.423	39.69
0.95	1.078	0.374	47.42	0.95	1.078	0.386	37.56
1.00	0.100	1.435	95.08	1.00	0.100	1.434	93.97
1.00	0.145	1.392	92.86	1.00	0.145	1.389	91.27
1.00	0.190	1.351	90.65	1.00	0.190	1.350	88.56
1.00	0.235	1.310	88.43	1.00	0.235	1.312	85.87
1.00	0.280	1.265	86.25	1.00	0.280	1.274	83.18
1.00	0.325	1.220	84.03	1.00	0.325	1.231	80.51
1.00	0.370	1.179	81.85	1.00	0.370	1.192	77.84
1.00	0.415	1.134	79.68	1.00	0.415	1.148	75.19
1.00	0.460	1.091	77.50	1.00	0.460	1.103	72.56
1.00	0.505	1.046	75.32	1.00	0.505	1.060	69.95
1.00	0.550	1.001	73.19	1.00	0.550	1.018	67.35
1.00	0.595	0.956	71.05	1.00	0.595	0.977	64.78
1.00	0.640	0.914	68.91	1.00	0.640	0.931	62.23
1.00	0.685	0.870	66.77	1.00	0.685	0.882	59.70
1.00	0.730	0.820	64.68	1.00	0.730	0.835	57.20
1.00	0.775	0.777	62.58	1.00	0.775	0.792	54.73
1.00	0.820	0.729	60.48	1.00	0.820	0.749	52.29
1.00	0.865	0.684	58.43	1.00	0.865	0.706	49.89
1.00	0.910	0.641	56.37	1.00	0.910	0.663	47.52
1.00	0.955	0.591	54.35	1.00	0.955	0.609	45.18
1.00	1.000	0.545	53.01	1.00	1.000	0.563	42.88
1.00	1.045	0.497	51.05	1.00	1.045	0.516	40.63
1.00	1.090	0.455	49.11	1.00	1.090	0.464	38.41
1.00	1.135	0.400	47.19	1.00	1.135	0.414	36.24
1.05	0.100	1.511	95.26	1.05	0.100	1.509	94.11
1.05	0.148	1.467	93.01	1.05	0.148	1.473	91.32
1.05	0.195	1.422	90.76	1.05	0.195	1.425	88.53
1.05	0.243	1.377	88.52	1.05	0.243	1.384	85.76
1.05	0.290	1.332	86.28	1.05	0.290	1.336	82.99
1.05	0.338	1.288	84.04	1.05	0.338	1.298	80.23
1.05	0.385	1.241	81.82	1.05	0.385	1.256	77.48
1.05	0.433	1.195	79.60	1.05	0.433	1.206	74.75
1.05	0.480	1.148	77.38	1.05	0.480	1.163	72.04

1.05	0.528	1.103	75.18	1.05	0.528	1.117	69.35
1.05	0.575	1.054	72.99	1.05	0.575	1.069	66.67
1.05	0.623	1.007	70.81	1.05	0.623	1.027	64.03
1.05	0.670	0.959	68.64	1.05	0.670	0.980	61.40
1.05	0.718	0.913	66.48	1.05	0.718	0.931	58.81
1.05	0.765	0.863	64.34	1.05	0.765	0.887	56.24
1.05	0.813	0.817	62.21	1.05	0.813	0.839	53.70
1.05	0.860	0.766	60.10	1.05	0.860	0.792	51.20
1.05	0.908	0.720	58.01	1.05	0.908	0.738	48.73
1.05	0.955	0.669	55.93	1.05	0.955	0.687	46.30
1.05	1.003	0.619	53.87	1.05	1.003	0.638	43.91
1.05	1.050	0.571	51.83	1.05	1.050	0.590	41.56
1.05	1.098	0.523	49.81	1.05	1.098	0.540	39.25
1.05	1.145	0.471	47.82	1.05	1.145	0.489	36.99
1.05	1.193	0.419	45.85	1.05	1.193	0.440	34.77
1.10	0.100	1.586	95.35	1.10	0.100	1.579	94.35
1.10	0.150	1.538	93.03	1.10	0.150	1.535	91.52
1.10	0.200	1.491	90.71	1.10	0.200	1.487	88.71
1.10	0.250	1.444	88.40	1.10	0.250	1.441	85.90
1.10	0.300	1.397	86.09	1.10	0.300	1.397	83.09
1.10	0.350	1.349	83.78	1.10	0.350	1.349	80.30
1.10	0.400	1.300	81.48	1.10	0.400	1.303	77.53
1.10	0.450	1.250	79.19	1.10	0.450	1.257	74.76
1.10	0.500	1.201	76.91	1.10	0.500	1.207	72.02
1.10	0.550	1.150	74.64	1.10	0.550	1.153	69.30
1.10	0.600	1.105	72.38	1.10	0.600	1.107	66.59
1.10	0.650	1.052	70.13	1.10	0.650	1.061	63.91
1.10	0.700	1.002	67.89	1.10	0.700	1.007	61.26
1.10	0.750	0.952	65.66	1.10	0.750	0.957	58.63
1.10	0.800	0.900	63.46	1.10	0.800	0.913	56.03
1.10	0.850	0.849	61.26	1.10	0.850	0.860	53.46
1.10	0.900	0.797	59.08	1.10	0.900	0.809	50.93
1.10	0.950	0.748	56.92	1.10	0.950	0.755	48.43
1.10	1.000	0.698	54.78	1.10	1.000	0.699	45.98
1.10	1.050	0.646	52.66	1.10	1.050	0.652	43.56
1.10	1.100	0.592	50.56	1.10	1.100	0.601	41.18
1.10	1.150	0.540	48.48	1.10	1.150	0.549	38.84
1.10	1.200	0.487	46.42	1.10	1.200	0.493	36.55
1.10	1.250	0.437	44.39	1.10	1.250	0.432	34.31

Vita

Hannah Spece

922 Ellsworth St. Floor 2, Philadelphia, PA 19147

hgs29@drexel.edu

Education

Drexel University — Philadelphia, PA

Ph.D. in Biomedical Engineering — In progress

M.S. in Biomedical Engineering — May 2018

The Pennsylvania State University, Schreyer Honors College — State College, PA

B.S. in Mechanical Engineering with Honors in Mechanical Engineering — May 2014

Professional & Research Experience

Drexel University — Philadelphia, PA

Ph.D. Candidate, Drexel Implant Research Center — Aug. 2016 - present

Currently studying the mechanical and osteoconductive properties of 3D printed porous PEEK for orthopaedic applications. Other research focuses include the examination of implant retrievals to determine the *in vivo* damage mechanisms for total joint arthroplasty components.

Additional roles at Drexel have included **Remote Course Facilitator** for assisting professors in the remote class format, **AJ Flex Face Shield project member** for 3D printing face shields to address Covid-19 PPE shortages, **Senior Design co-advisor**, and **Co-organizer** of the International PEEK and UHMWPE Meetings.

Instructor, Technological and Societal Impacts of 3D Printing

Designed a 3D printing-based curriculum for Honors First Year Seminar (HNRS 200), introduced students to core concepts of 3D printing, and facilitated discussions about related world impacts.

U.S. Food and Drug Administration (FDA), Center for Devices and Radiological Health — Silver Spring, MD

Oak Ridge Institute for Science and Education (ORISE) Research Fellow — July 2017- July 2018

Examined histopathological and retrieval analyses to investigate the relationships between implant characteristics and adverse local tissue reactions (ALTR).

Accenture — Philadelphia, PA

Technology Global Delivery Senior Analyst — Aug. 2014 – June 2016

Led a team of offshore developers and testers, translated client's business requirements into functional designs for Salesforce.com platform, and acted as a liaison between US and India teams.

Publications & Presentations

Peer-Reviewed Publications

2021 **Spece, H.**, Ouellette, E. S., Jones, O. L., MacDonald, D. W., Piuzzi, N. S., Lee, G. C., ... & Kurtz, S. M. Fretting Corrosion, Third-Body Polyethylene Damage, and Cup Positioning in Primary vs Revision Dual Mobility Total Hip Arthroplasty. The Journal of Arthroplasty.

Basgul, C., **Spece, H.**, Sharma, N., Thieringer, F. M., & Kurtz, S. M. Structure, properties, and bioactivity of 3D printed PAEKs for implant applications: A systematic review. Journal of Biomedical Materials Research Part B: Applied Biomaterials.

Spece, H., Basgul, C., Andrews, C. E., MacDonald, D. W., Taheri, M. L., & Kurtz, S. M. A systematic review of preclinical in vivo testing of 3D printed porous Ti6Al4V for orthopedic applications, part I: Animal models and bone ingrowth outcome measures. Journal of Biomedical Materials Research Part B: Applied Biomaterials.

2020 **Spece, H.**, Yu, T., Law, A. W., Marcolongo, M., & Kurtz, S. M. (2020). 3D printed porous PEEK created via fused filament fabrication for osteoconductive orthopaedic surfaces. Journal of the mechanical behavior of biomedical materials.

Torosyan, Y., **Spece, H.**, Goodacre, N., Azarbaijani, Y., Marinac-Dabic, D., & Kurtz, S. M. (2020). In silico approaches for enhancing retrieval analysis as a source for discovery of implant reactivity-related mechanisms and biomarkers. Journal of Biomedical Materials Research Part B: Applied Biomaterials, 108(1), 263-271.

2019 **Spece, H.**, Schachtner, J. T., MacDonald, D. W., Klein, G. R., Mont, M. A., Lee, G. C., & Kurtz, S. M. (2019). Reasons for revision, oxidation, and damage mechanisms of retrieved vitamin E-stabilized highly crosslinked polyethylene in total knee arthroplasty. The Journal of arthroplasty.

Spece, H., Underwood, R. J., Baykal, D., Eiselstein, L. E., Torelli, D. A., Klein, G. R., ... & Kurtz, S. M. (2019). Is There Material Loss at the Conical Junctions of Modular Components for Total Knee Arthroplasty?. The Journal of arthroplasty.

2018 **Spece, H.**, MacDonald, D., Mont, M., Lee, G. C., & Kurtz, S. (2018). Fretting Corrosion and Polyethylene Damage Mechanisms in Modular Dual Mobility Total Hip Arthroplasty. In Beyond the Implant: Retrieval Analysis Methods for Implant Surveillance. ASTM International.

Select Conference Presentations

2021 **Spece H**, MacDonald DW, Jones OL, Piuzzi NS, Lee G-C, Mont MA, Klein GR, Kurtz SM. Polyethylene Damage And Fretting Corrosion In Primary Vs. Revision Dual Mobility Total Hip Arthroplasty. Podium Presentation 0290. Orthopaedic Research Society 2021 Annual Meeting, Virtual, February 12-16, 2021.

Criscione J, **Spece H**, Oral E, Kurtz SM. Vancomycin Elution From Porous PEEK. Poster 0380. Orthopaedic Research Society 2021 Annual Meeting, Virtual, February 12-16, 2021.

2020 **Spece H**, Yu T, Law AW, Leung JK, Marcolongo M, Kurtz SM. Customizable 3D Printing of PEEK Implants With Porosity Based on Triply Periodic Minimal Surfaces. International Society for Technology in Arthroplasty, New Early-Career Webinar Series, Virtual, November 20-21, 2020.

Spece H, Yu T, Law AW, Leung JK, Marcolongo M, Kurtz SM. 3D Printed Porous PEEK Created via Fused Filament Fabrication for Osteoconductive Orthopaedic Surfaces. ASME International Mechanical Engineering Congress and Exposition, Virtual, November 16-19, 2020.

2017 **Spece H**, MacDonald DW, Mont MA, Lee GC, Kurtz SM. Fretting Corrosion and Polyethylene Damage Mechanisms in Modular Dual Mobility Total Hip Arthroplasty. Podium Presentation, Paper No. 27, 27th Annual Meeting of the American Association of Hip and Knee Surgeons. Dallas, TX, November 2-5, 2017.

Honors & Awards

2021 Drexel University Graduate College Research Excellent Award Finalist

2020 Best Presentation Award, ISTA New Early-Career Webinar Series

Drexel University Graduate College Outstanding Mentorship Award Finalist

2019 Philadelphia Society of Tribologists and Lubrication Engineers Scholarship Recipient